

**A Thesis Submitted for the Degree of PhD at the University of Warwick**

**Permanent WRAP URL:**

<http://wrap.warwick.ac.uk/163648>

**Copyright and reuse:**

This thesis is made available online and is protected by original copyright.

Please scroll down to view the document itself.

Please refer to the repository record for this item for information to help you to cite it.

Our policy information is available from the repository home page.

For more information, please contact the WRAP Team at: [wrap@warwick.ac.uk](mailto:wrap@warwick.ac.uk)



# **Inertial Confinement Fusion: Energy Transport and Shock Ignition**

by

**Duncan Barlow**

**Thesis**

Submitted to the University of Warwick

for the degree of

**Doctor of Philosophy**

**Department of Physics**

2021

# Contents

<b>List of Tables</b>	<b>iv</b>
<b>List of Figures</b>	<b>v</b>
<b>Acknowledgments</b>	<b>xviii</b>
<b>Declarations</b>	<b>xx</b>
<b>Abstract</b>	<b>xxi</b>
<b>Acronyms</b>	<b>xxii</b>
<b>Chapter 1 Introduction</b>	<b>1</b>
1.1 Purpose of Fusion Energy . . . . .	1
1.2 Inertial Confinement Fusion Energy . . . . .	3
1.2.1 Alpha Particles and Areal Density . . . . .	4
1.2.2 Implosion Velocity . . . . .	8
1.2.3 Adiabatic and Shocks . . . . .	9
1.2.4 Laser Driver . . . . .	11
1.2.5 Energy Transport . . . . .	16
1.2.6 Summary of Issues . . . . .	18
1.3 Shock Ignition . . . . .	21
1.4 Summary of Odin's Conservation Equations . . . . .	23
<b>Chapter 2 Theory: Thermal Conduction</b>	<b>27</b>
2.1 Simplified Derivation from Plasma Kinetic Equation . . . . .	27
2.2 Isotropic . . . . .	29
2.2.1 Beyond Spitzer-Härm . . . . .	30
2.3 Conduction by Ions . . . . .	31

<b>Chapter 3</b>	<b>Application and Tests: Thermal Conduction</b>	<b>32</b>
3.1	Design Brief . . . . .	33
3.2	Finite Difference Method Selection . . . . .	34
3.3	Sheng et al 2008: Applied Method . . . . .	38
3.3.1	Modifications . . . . .	41
3.4	Pert 1981: Comparison Method . . . . .	42
3.5	Time Stepping Options . . . . .	43
3.5.1	Explicit Super-stepping: Comparison Method . . . . .	44
3.5.2	Implicit: Applied Method . . . . .	45
3.6	Future Work . . . . .	50
3.7	Tests . . . . .	50
3.7.1	Kershaw's Z grid . . . . .	51
3.7.2	Convergence . . . . .	53
3.7.3	Heat-front into Cold Medium . . . . .	55
3.8	Inertial Confinement Implosion . . . . .	57
3.8.1	Simplified Laser Model . . . . .	58
3.8.2	Cold Start (Quiet Start) . . . . .	59
<b>Chapter 4</b>	<b>Theory: Hot Electrons</b>	<b>61</b>
4.1	Plasma Waves . . . . .	62
4.2	Laser Plasma Instabilities . . . . .	64
4.3	Hot Electron Characteristics . . . . .	68
4.3.1	Parameter Scan Setup and Comparison Simulations . . . . .	70
4.3.2	Base Hot Electron Simulation for Parameter Scan . . . . .	71
4.3.3	Target Preheat . . . . .	71
4.3.4	Preheat Variation in Parameter Scan . . . . .	72
4.3.5	Parameter Scan Implosion Analysis . . . . .	72
<b>Chapter 5</b>	<b>Application and Tests: Hot Electrons</b>	<b>76</b>
5.1	Application . . . . .	76
5.1.1	Path Tracking . . . . .	78
5.1.2	Sampling . . . . .	79
5.1.3	Energy Deposition (Stopping Power) . . . . .	81
5.1.4	Scattering . . . . .	84
5.1.5	Reflux . . . . .	86
5.1.6	Future Work . . . . .	87
5.2	Tests . . . . .	88
5.2.1	Deposition Test . . . . .	88



5.2.2	MCNP Code Comparison: Scattering Test . . . . .	89
<b>Chapter 6</b>	<b>NIF Solid Target Experiment</b>	<b>91</b>
6.1	Background . . . . .	92
6.2	Simulation to Match NIF SSS Experiment . . . . .	94
6.3	Analysis of NIF SSS simulation . . . . .	95
6.4	Shock Ignition Implosion Setup . . . . .	97
6.5	Applying Hot Electron Characterisation to Shock Ignition . . . . .	99
<b>Chapter 7</b>	<b>Omega Conical Target Experiment</b>	<b>101</b>
7.1	Conical Target Experiment . . . . .	102
7.2	Shock Ignition Simulations . . . . .	105
7.3	Hot Electron Characterisation Disparity . . . . .	107
<b>Chapter 8</b>	<b>Conclusion</b>	<b>110</b>

# List of Tables

3.1 A brief literature review of which finite difference methods exhibit  
which ideal properties. Citations recorded at time of writing. X  
means that the method has the property. . . . . 36

# List of Figures

1.1	Schematic showing the 4 main stages of laser direct drive, central hotspot ignition. Figure reproduced from Craxton et al. [2015]. . . .	3
1.2	Nuclear reactivity (or reaction cross-section $\langle\sigma v\rangle$ ) for the three lowest temperature fusion reactions. The peak of the blue curve (DT) is at a temperature $\sim 10^8\text{K} \sim 10\text{keV}$ . Figure reproduced from Wikipedia Dstrozzi [2020]. . . . .	5
1.3	Capsule energy transfer over the course of an implosion. It shows $\approx 100\text{kJ}$ peak kinetic energy converted with $\theta < 0.5$ efficiency to the hotspot. Improved efficiency can be achieved with a larger radius, thinner shell, however this also leads to hydrodynamic instabilities. Figure reproduced from Craxton et al. [2015]. . . . .	8
1.4	Image in the rest frame of a shock. The density and pressure of the fluid increase as it passes through the shock, but velocity decreases, from $u_1$ to $u_2$ , to conserve mass at the shock front. In the lab rest frame the shock would be travelling at a velocity $u_s$ left to right into stationary fluid defined by subscript 1 and accelerating it to a velocity $u_2 - u_1$ . . . . .	9
1.5	Schematic of the phenomena that might occur as the electromagnetic wave created by the laser travels up the density gradient toward the critical surface. The shorthand “em” denotes electromagnetic wave with the arrow showing the result of laser plasma interaction giving either, em as backscattered light, “l” meaning Langmuir (electron plasma) waves or “ia” ion acoustic wave (More detail on plasma waves can be found in Chapter 4). Image reproduced from Pfalzner [2006].	12
1.6	Schematic of electron’s closest approach $b$ as it collides with an ion in the plasma. This is a classical reduction of a quantum physics interaction. If the electron also absorbs a photon as it accelerates around the ion then this is an inverse bremsstrahlung event. . . . .	13

1.7	Three fluid system used to simulate HEDP, made up of free electrons, ions and a radiation fluid. The (dominant) interactions between the fluids are shown with arrows, including the looping arrows which represent relaxation time to establish thermodynamic equilibrium and set the particle distribution to a Maxwellian. . . . .	17
1.8	Target and laser pulse shape predicted to give energy gain of 48 times larger than incident laser energy of 1.5MJ. (Top, Left) Capsule layout with DT central gas region, DT shell and CH plastic ablator all cooled to cryogenic temperatures. (Axes) A laser pulse shape assumed to be emitted with spherical uniformity. The power is from all incident beams. The drive phase which generates the majority of the kinetic energy is between 6.0 – 10.5ns. All features before 6ns are to set the adiabat of the implosion and create compressional shocks. There are 3 “picket pulses” at $\approx 0.5\text{ns}$ , $\approx 1.9\text{ns}$ and $\approx 3.7\text{ns}$ (Goncharov et al. [2003]). There is a “foot” between 4.8 – 6.0ns (Dittrich et al. [2014], terminology more common to indirect drive ICF). Peak velocity of the shell occurs at $\approx 10.0\text{ns}$ and stagnation occurs at $\approx 11.5\text{ns}$ . Ignition occurs at $\approx 11.3\text{ns}$ and the burn fraction is predicted to be 20% of the DT fuel. Figure reproduced from Craxton et al. [2015]. . . . .	19
1.9	Predictive capabilities of 1D (blue) and 2D (green) simulations compared to experiment for different implosion velocities. Dashed lines represent the loss in yield compared to experiment. They also correspond approximately to increased implosion velocities. The high velocity implosions that show large yields in 1D, but the growth of hydrodynamic instabilities mean that both experiment and 2D simulation see no net benefit from increasing implosion velocity to the speeds required for ignition. Figure reproduced from Presentation by Richard Town, NIF, 2017 . . . . .	20

1.10	Shock ignition (SI) target and pulse shape to contrast with conventional target and pulse in Figure 1.8. (a) Target cross-section, CH foam “wetted” with DT ice, pure DT ice and a central DT gas region. The radius of the SI target is much less than that of the target in Figure 1.8. (b) As shown in Figure 1.8 the laser power against time but with a second axis indicating the approximate intensity of the laser in units of $10^{15}\text{W}/\text{cm}^2$ . The solid line corresponds to SI with a gain of $\times 55$ the input laser energy of $\approx 300\text{kJ}$ and the dashed line corresponds to a conventional laser pulse that does not ignite. Figure reproduced from Betti et al. [2007]. . . . .	22
3.1	Schematic detailing 5 and 9 point stencil. Blue dashed lines represent cell boundaries, black dots are the cell centred values and the solid lines represent inter-cell flux. . . . .	37
3.2	Diffusion notation. Left: image showing the grid with cell centres $K, K_A, K_B, L, L_A$ and $L_B$ , vertices $A$ and $B$ , and the edge $\sigma$ . Right: Centred and reoriented is the line joining the vertices $A$ and $B$ . The key vectors for the flux calculation from $K$ are the edge normal $\vec{n}_{K,\sigma}$ and the non-orthogonal basis $\vec{\tau}_{BA}$ and $\vec{\tau}_{KI}$ (one parallel to the edge and the other parallel to an extension of a line joining cell centre to edge centre) with cell $L$ also having a face normal $\vec{n}_{L,\sigma}$ and non-orthogonal basis $\vec{\tau}_{LI}$ and $\vec{\tau}_{AB}$ . Reproduced from Sheng and Yuan [2008]. . . . .	38
3.3	Energy conservation test (no hydrodynamics). Left: initial temperature state with a hot quadrilateral $T_h = 10^5\text{K}$ and a cold background $T_c = 2 \times 10^4\text{K}$ . Right: final diffused state. Images of explicit simulation. The final state breaks monotonicity with minima lower than $T_c$ visible in the right image at top left and bottom right of the diffused heat. Both arithmetic averaging for implicit and explicit conduction were susceptible to violate the lower extremum depending on time step size. In the test arithmetic and harmonic averaging for implicit conduction achieved a relative energy conservation $10^{-10}$ while explicit conduction achieved $10^{-16}$ . . . . .	41

3.4	Left: Explicit stencil for 1D. 3 point spatial stencil and 1 output at $t = n + 1$ . Right: Implicit stencil for a 1D code. Spatial 3 point stencil this time at $t = n + 1$ which have to be solved as a series of simultaneous equations with the boundary condition and the 1 input point at $t = n$ providing closure. Crossing the orange dotted line implies a change in time step. A semi-implicit method would use all 6 points from the two schematics (i.e. 3 spatial point stencil from $t = n$ and 3 points from $t = n + 1$ ). The weighting of the $t = n$ vs $t = n + 1$ is what determines how implicit a method is. . . . .	44
3.5	Left: Numerical asymmetries present in a late stage capsule implosion without filtering (left half) and with a median filter (right half) the noise is reduced several orders of magnitude. The image includes the coronal region, which is very susceptible to tangling due to the high velocity flows and low densities. Right: Two simulations using the median filter focusing on the high density capsule during peak compression, a uniform implosion (left half) compared to a simulation that was driven asymmetrically with laser perturbations (right half). This demonstrates median filtering capabilities with non-uniform simulations. . . . .	48
3.6	The figures show for simulation of a target implosion the differences between an unfiltered (solid blue line) and a filtered (dashed orange line) simulation. Left: shell density, slight differences are visible at the ablation front (630 microns). Right: electron temperature throughout the target and ablation plasma, there is a difference in temperature in the coronal plasma (800microns). . . . .	49
3.7	Left: Implicit conduction using a 5 point method. Right: Implicit conduction using Sheng and Yuan [2008] full 9 point method. Both images are a snapshot of a heatwave propagating from right to left. Simulation using the 5 point method leads to the grid affecting the diffusion front despite the uniform material properties and boundaries in the y-direction. The nine point method shows improved uniformity.	51
3.8	Implicit method comparison between harmonic averaging (blue dots) and arithmetic averaging (red dots) for edge centred coefficients compared to an analytic solution at infinite time (black line). The simulations are at an equilibrium state for the Z-grid diffusion problem. All cell centres (dots) should converge to the black line. . . . .	52

3.9	Convergence test for the implicit and explicit models. Gradients (Order of convergence) is given below each plot except (d) which shows the test problem at the point the test was taken, this is a snapshot of a heat wave travelling across the domain. The initial temperature of the domain is, $T_c = 10^8\text{K}$ and the right boundary is held at $T_h = 10^9\text{K}$ .	54
3.10	Simulation of a heat-front moving into a cold medium. Reproduction of a test shown in Basko et al. [2009] to highlight the benefit of an arithmetic average over the harmonic average derived from the flux matching condition. Using a harmonic average heat cannot flow into a cold medium $T_c = 0$ .	56
3.11	Full scale ICF simulation, a cross-section of a 2D simulation. Density is plot in black and temperature in red, the blue dashed lines correspond to, the ablation front at the edge of the shell (left) and the critical density beyond which laser light cannot propagate (right). The blue arrow indicates the region where thermal conduction plays its most critical role in direct drive ICF (transporting energy to ablate the target).	57
3.12	Laser rays (red, where darker corresponds to more energy deposited, normalized per ray) travelling on radial trajectories across 2D Odin mesh (purple). The target shell is visible at $ Z  \sim 300\mu\text{m}$ and the hotspot $ Z  < 250\mu\text{m}$ .	58
4.1	The 3-wave dispersion relation of a Maxwellian plasma interacting with light. The three waves are the electromagnetic wave (EM, blue), the electron plasma wave (EPW, green), and the ion-acoustic wave (IAW, red). The dispersion relation depends on the plasma parameters, $n_e = 0.15n_c$ , $T_e = 3.5\text{keV}$ , $T_i = 1.7\text{keV}$ and $Z = 1$ which is typical for LPI in ICF, except $Z = 3.5$ for the CH plastic material ablated from the targets. The frequency and wave number have been normalised with the laser wave frequency in a vacuum (for $\lambda_L = 351\text{nm}$ ), $\omega_0 = ck_0 = \omega_L$ . This image is reproduced from Seaton [2019]	63

- 4.2 (a) A cross-section of the target used in implosion simulations. The capsule shell features a plastic outer layer (CH)  $\rho = 1.05\text{g/cm}^{-3}$ , a DT inner layer  $\rho = 0.25\text{g/cm}^{-3}$ , and a DT gas filled core  $\rho = 0.06\text{g/cm}^{-3}$ . (b) black, solid line shows the laser power deposited due to IB and (“dump-all”) resonant absorption of radial rays at critical density. This is equivalent to laser power emitted after losses due to CBET, target convergence and SRS backscatter are considered and the red, dashed line shows the time integrated power deposited (energy) equivalent to  $\approx 350\text{kJ}$ . As in Atzeni et al. [2019] the predicted laser power at the source to achieve the implosion is between,  $500 - 700\text{kJ}$  which corresponds to laser-target coupling of  $\sim 50 - 75\%$  typical of ICF and SI. The peak power of  $220\text{TW}$  corresponds to a laser intensity at  $n_{crit}/4$  ( $\approx 1100\mu\text{m}$ ) of  $I \approx 10^{16}\text{W/cm}^2$ . . . . . 66
- 4.3 Simulations investigating the effect of hot electrons on SI. Blue solid lines are from a SI simulation without hot electrons. Orange dashed lines are from a simulation without a SI spike. All simulations are run without alpha heating. Green dash-dot lines are from a simulation which will be the base of a parameter scan of hot electron characteristics. The base hot electron characteristics are beam size corresponding to a uniform solid angle of  $2\pi(2 - \sqrt{2})/2\text{sr}$  equivalent to a half cone angle of  $45^\circ$ , laser to hot electron conversion percentage  $10\%$  and temperature of  $40\text{keV}$ . (a) shows the density at peak compression, a simple measure of implosion success, (b) shows the background electron temperature near peak velocity in the cold fuel demonstrating hot electron preheat, and (c) shows the fluid pressure near peak velocity. Also visible is the hot electrons’ effect on the SI shock ( $\approx 175\mu\text{m}$ , green, dash-dot), spreading it over a larger length to appear more like a pressure wave (as seen in the orange, dashed line). . . . . 67



4.4	The same simulations as Figure 4.3 but looking at the ignition parameters, (a) areal density and (b) ion temperature from Equation 1.5 during peak compression. The maximum areal density decreases $\approx 15\%$ when hot electrons are simulated and again by $\approx 15\%$ when the SI spike is removed, however there is very little change in hotspot ion temperature. The areal density and ion temperature of the SI simulation without hot electrons (blue line) is comparable to direct drive, central hotspot ignition simulation seen in Craxton et al. [2015], (fig.3–5) which achieves a gain of $\sim 50$ . . . . .	68
4.5	Hot electron characteristics parameter scan examining preheat at 12.0ns (time-integrated preheat). Centralized is the blue dashed vertical line which indicates the separation between hotspot and shell. The solid blue line is the base hot electron characteristics shown in Figure 4.3, a uniform beam over a cone with half angle of $45^\circ$ , laser to hot electron conversion percentage 10% and temperature of 40keV. Preheat is most deleterious in the cold fuel between $50 - 75\mu\text{m}$ . . . .	69
4.6	Parameter scan of hot electron energy fraction at quarter critical ( $\eta_{qc}$ ), where modification is made from the “base” hot electron characteristics simulation shown in Figure 4.3. From peak compression density (a) it is visible that a $\eta_{qc} = 0.4$ (pink, dash-dot line) is worse than the simulation without a SI spike (orange, dashed line) despite having a stronger shock in (c). Also visible is the increase in shell width at peak compression as $\eta$ increases. The background electron temperature in (b) shows $\eta_{qc} < 0.1$ does not significantly pre-heat ahead of the shock at $\approx 150\mu\text{m}$ . The igniter shock pressure (c) demonstrates that hot electrons can modify shock timing $\eta_{qc} = 0.4$ (pink, dash-dot line). . . . .	73

- 4.7 Parameter scan of hot electron beam size where angles quoted correspond to a half cone angle ( $\theta$ ). Emission is uniform over the cone/beam. Modification is made from the “base” hot electron characteristics simulation shown in Figure 4.3. The target (defined by material within the ablation surface), when viewed from quarter critical, occupies a solid angle of  $\approx 0.84\text{sr}$  (cone half angle  $30^\circ$ ) meaning that the green dash-dot line corresponds to the most deleterious angle. If the angle were further reduced, the change in deposition would be small (although path length and incident angle to the target would be reduced) since the dominant effect of modifying beam size appears to be the fraction of hot electrons that are incident on the target. An isotropic distribution of hot electrons would result in preheat four times smaller than the purple solid line, which occupies a solid angle of  $\approx \pi\text{sr}$ . More drive energy would be wasted, so even an isotropic distribution would not improve peak compression density much compared to that of the purple line. . . . . 73
- 4.8 Parameter scan of hot electron temperature ( $T_h$ ), where modification is made from the “base” hot electron characteristics simulation shown in Figure 4.3. It is expected that a low hot electron temperature would improve shock formation, but the green dash-dot line in (c) shows even a cold population is deleterious to shock formation. This is not due to preheat as very little is visible in (b) but is better explained by wasted laser drive energy from hot electrons not incident on the target or not making up the density ramp to the ablation front. The peak compression density shown in (a) is almost unaffected by the low temperature hot electrons  $T_h = 20\text{keV}$ . High temperature hot electrons  $T_h = 80\text{keV}$ , purple solid line appear to leave the shock front in (c) unaffected compared to the base characteristics (red dotted line) and cause near uniform preheat throughout the target. The high temperature population would be easy to model (with a straight line model or preheat multiplier over the entire grid) due to its near uniform energy deposition and would likely not prevent SI if  $\eta_{qc} < 0.05$  or  $\theta > 60^\circ$  taking it below the  $1\text{kJ/mg}$  limit on Figure 4.5 . . . 74

5.1	Top: Schematic demonstrating how hot electrons are generated from laser rays at the quarter critical surface. Bottom: Odin diagnostic showing the density of a solid plastic target (colour bar not shown) with electrons paths emitted from a single ray overlaid (for more details on the target, see Chapter 6). The colour axis refers to the hot electron path energy. . . . .	77
5.2	(Left) Linear and (Right) logarithmic particle distributions. The histogram represents a 40 keV thermal hot electron emission distribution using Odin's direct sampler with 10,000 paths, each path is mono-energetic. Direct/Monte-Carlo sampling gives each path an equal number of electrons and uses the cumulative distribution function to weight initial electron energy. . . . .	79
5.3	(Left) Linear and (Right) logarithmic particle distributions. The histogram represents a 40 keV thermal hot electron emission distribution using Odin's uniform sampler between 0 and 300 keV with 10,000 paths, each path is mono-energetic. Uniform sampling spread the paths uniformly in energy space (initial electron energy) and use particle number weighting from the probability distribution function. . .	80
5.4	40 keV thermal hot electron energy distribution for 45° (top) and 27.5° (bottom) half cone angle. The distribution was taken at the edge of the simulated domain which was $\approx 10\text{mm}$ for this snapshot. Uniform sampling between 0 and 300 keV with 10,000 paths, each path is mono-energetic. . . . .	86
5.5	Direct comparison between Odin hot electron deposition (black line) to Fox [2014] (green dots) of 1D hot electron energy deposition for a Maxwellian beam at 30keV. The hot electron beam travels from a low density region, $0.1\text{g/cm}^3$ on the left to a high density, $10.0\text{g/cm}^3$ region on the right with the material boundary at $50\mu\text{m}$ . The total energy deposition error compared to prior work was $\mathbf{L_1} < 0.4\%$ . . . .	88

5.6	Code comparison to Werner et al. [2018]. (Left) Problem setup, a collimated electron beam with a thermal distribution of electrons at 40keV enters dense uniform material (ionized ideal gas hydrogen, at $1\text{g}/\text{cm}^3$ and 7eV) centred on the point $Z = 0, R = 0$ and a beam width of 200 microns (simulation grid was 200x200 cells). (Right) Amount of energy deposited per source particle averaged radially, the black line is MCNP's energy deposition (rescaled 30% so that deposition at $1000\mu\text{m}$ is the same), the orange dashed line is Odin's hot electron energy deposition with scattering, and the blue line is Odin's hot electron deposition without scattering. There is a significant difference in the amount of hot electron dispersion that occurs, which is partially due to MCNP's improved trajectory updating with sub-cell resolution. . . . .	89
6.1	(a) GXD data showing the shock propagation. (b) FFLEX data showing x-ray bremsstrahlung temperature used to infer hot electron temperature ( $T_h = 56\text{keV}$ ) and total kinetic energy (35kJ) overlaid. National Ignition Facility (NIF) direct drive solid target strong shock (SSS) experiment N190204-002. Measurement of X-ray emission using the filter-fluorescer diagnostic system (FFLEX, McDonald et al. [2004], in the range 20 – 500keV). The peak intensity of the laser at quarter critical is $I \sim 10^{16}\text{W}/\text{cm}^2$ . . . . .	93
6.2	(a) Inverse pressure length scale ( $d(\ln P)/dr$ ) showing the shock propagation in the simulation and the red circles representing the shock timing extracted from Figure 6.1 with corresponding error bars. (b) Power emitted: dashed black is the experimental measure, solid black is the simulation after CBET and SRS backscatter and red solid is the hot electrons, equivalent to 35kJ. . . . .	95
6.3	(a) Shows the density profile of the target in black and the hot electron deposition in red. The critical surface is at $\approx 1050\mu\text{m}$ , the ablation front is at $\approx 900\mu\text{m}$ but between $850 - 900\mu\text{m}$ there is a hot electron pressure front. (b) Comparison of the density profile (black) and pressure profile (red) for simulations with (solid) and without (dashed) hot electrons. The change in shock timing is approximately equivalent to 0.1ns at this point, but will be 0.3ns by the time the two shock coalesce. After coalescence, the shock will travel at the same velocity (with the same pressure) as the simulation with hot electrons.	96

6.4	Hotspot thermodynamic path using the same hotspot definition as Ref. Colaitis et al. [2016] (hotspot edge $T_{edge} = T_i/10$ where $T_i$ is the core temperature). The isobaric ignition criteria is displayed as a dashed black line. The simulation without hot electrons and without a SI spike lie at the extremum, with two simulations including hot electrons between. The difference is the timing of the shock ignition spike. We find the least degraded implosion requires a delay of 0.2ns on the shock ignition spike when compared to the optimal design without hot electrons. . . . .	98
6.5	(a) The areal density (black) and cumulative hot electron energy deposition (red) of two simulations with hot electrons. The solid lines correspond to a simulation with a laser pulse shape optimized without hot electrons and the dashed line is the reduced preheat found by delaying the ignition pulse by 0.2ns. Both snapshots are taken 0.1ns into the shock pulse and are therefore 0.2ns offset. (b) Density (black) and pressure (red) achieving optimal shock timing for a simulation with (dashed) and without (solid) hot electrons. The shock timing offset is 0.1ns due to the volumetric heating of the hot electrons as seen in the NIF SSS experiment. . . . .	99
7.1	(a) Target setup with beam alignments. The target is a 3.6mm diameter cone with a full cone angle of $152^\circ$ . The layered cone was $40\mu\text{m}$ CH plastic on which the laser was incident, with a $5\mu\text{m}$ copper layer and a $30\mu\text{m}$ CH back. (b) Simulation of experiment done on H2D gives density scale length (red, solid), electron temperature (blue, dashed), ion temperature (black, solid) and intensity (green, solid, read from the right axis). This is the first published experiment to achieve SI plasma parameters seen in (b) at $\approx 1.2\text{ns}$ . Reproduced from Scott et al. [2021]. . . . .	102

- 7.2 (a) Observed hot electron temperature (red, left axis) and laser to hot electron conversion efficiencies (green, right axis) for different intensity shots (bottom axis). Hot electron temperature shows little sensitivity to intensity and is consistently  $\approx 40\text{keV}$ . Hot electron fraction shows some sensitivity to intensity, however the trend is not clear and all are within 2 standard deviations of 1.5%. The use of imprint mitigating “smoothing by spectral dispersion” phase plates (SSD, Regan et al. [2000]) have no effect on hot electron characteristics. (b) The SRS reflectivity (backscatter) observed is affected by the use of SSD. The experiments done without the SSD (red, diamonds) show more backscatter,  $\sim 5\%$ , than those with the SSD,  $\sim 1\%$  (blue, dots). The mitigation of LPI with more spatially uniform lasers is one of the desired effects of SSD, so it is an expected result. The graph also shows a trend of increasing SRS backscatter with increasing intensity. Reproduced from Scott et al. [2021]. . . . . 103
- 7.3 A spherically bent quartz crystal imager (SCI, Stoeckl et al. [2012]) was used to give spatially resolved images of high energy ( $\sim 8\text{keV}$ ) hot electrons. (a) the low intensity beams show the most intense emission near the quarter critical surface where the beams are focused. (b) with the high intensity beams, the diagnostic shows intense patches with small structure. It is believed that hot electron emission cones from the non-uniform high intensity beams may cause the structures. Reproduced from Scott et al. [2021]. . . . . 103
- 7.4 Shock ignition coronal plasma parameters. The quarter critical surface (blue, dashed) has density scale length  $\approx 500\mu\text{m}$  (black, left axis), electron temperature  $\approx 4\text{keV}$  (red, right axis) and peak laser intensity  $\approx 2 \times 10^{15}\text{W}/\text{cm}^2$  at quarter critical. This can be compared to the experimental measured parameters shown in Figure 7.1 (b). . 105

7.5	Shock ignition implosion simulated without (black, solid) and with (red, dashed) a hot electron population being generated from the quarter critical surface during the shock ignition spike in laser power. The hot electron population is simulated with a temperature of 40keV, an energy fraction at quarter critical of 2.5%, and a full cone angle of 90°. Simulations are run without alpha particle heating, and the target and pulse shape are based on Atzeni et al. [2019]. (a) Pressure in the shock immediately after the laser pulse has ended, approximately at peak velocity. (b) Density at peak compression. Both (a) and (b) show that the hot electron population are having a negligible effect during the key phases of a shock ignition implosion. Reproduced from Scott et al. [2021]. . . . .	106
-----	--	-----

# Acknowledgments

I acknowledge financial support from ESPRC, AWE and CCPP. I would like to acknowledge the work of many experimentalists at the National Ignition Facility and the Laboratory for Laser Energetics, particularly Ken Anderson and Wolfgang Theobald who made the observations in Chapter 6 and; Robbie Scott and others (Scott et al. [2021]) who made the observations in Chapter 7.

I would like to acknowledge the support and advice of my supervisor Tony Arber, whose patience, calm and extensive knowledge was critical to the success of the project. I would also like to acknowledge the work of Tom Goffrey whose creation and continuing development of Odin made this project possible. His kindness and understanding was invaluable to my work. Keith Bennett's meticulous attention to detail and deep affinity with programming which contributed to the success of this project. A very enjoyable summer internship with Robbie Scott has ignited my passion for fusion energy, and I am very grateful for his continuing support. Technical discussions with SJ Spencer, Alun Rees, Phil Bradford and Matt Khan stand out among the many useful and insightful conversations with brilliant people I have been lucky enough to enjoy. From these incredible friends and many others I have learnt much.

I would like to acknowledge my immense privilege in life, but also to thank my family who have worked hard (and been lucky themselves) to put me in a position to dedicate this effort to academic ends. The sense of belonging I have gained through family and friends has given me the confidence to strive for excellence, even if at times I fall short. Thank you all.

I would like to acknowledge the greatest threat to diversity, inclusion, and



enjoyment of physics: intellectual insecurity. We were all born curious and unsure, it is the loss of these human attributes that corrupts the most fundamental and beautiful science.

The final year of my PhD was in the confines of our self-inflicted isolation. Although not perfect, it is actions such as this which give me the confidence in humanity to perform this work in the trust that it will be used for the long-term benefit of all. We are in more than one crisis and I hope each small effort carries us to a better future. Cynicism is easy, hope is hard, but balance is critical.

# Declarations

This thesis is submitted to the University of Warwick in my application for a Doctor of Philosophy degree. The work has been written by the author and not been submitted for any previous applications.

Original work is featured in Chapters 3, 4, 5, 6 and 7. Sources have been accredited with citations where material has been reproduced. Part of the works featured in Chapter 6 and 7 have been submitted for publication.

Chapters 6 and 7 focus on experiments that were not carried out by the author. Ignition scale simulation and analysis was provided as original work for this thesis. Further demarcation is made in each chapter.

# Abstract

From hydrodynamics alone, shock ignition (SI) achieves the largest fusion energy output per energy input, using current inertial confinement fusion (ICF) facilities (Betti et al. [2007]). This gain margin is critical if ICF is to be used for energy generation. The National Ignition Facility (NIF, Miller et al. [2004]) is the world's largest laser facility, with a 1.8MJ laser energy. It has not yet achieved ignition and although not designed to work in the same direct drive configuration as SI there are simulations showing an alignment called polar direct drive (PDD) could be used to ignite an implosion (Anderson et al. [2013]). Strong shock experiments intended to investigate the fundamental principles of SI have shown that hot electrons generated from laser plasma instabilities (LPI) can degrade shock creation (Theobald et al. [2012]; Nora et al. [2015]), but LPI are a phenomenon that do not scale (Rosenberg et al. [2018]) and so further investigation is required at SI relevant plasma conditions.

SI simulations require accurate hydrodynamics, a laser driver, energy transport and a kinetic model of hot electrons. Odin uses arbitrary Lagrangian-Eulerian (ALE) methods to accurately capture the hydrodynamics. This thesis introduces a diffusion operator to model energy transport, as well as, a simplified laser driver and a full 3D Monte-Carlo scattering model of hot electrons.

This thesis presents Odin's use in support of two of the first experiments that characterize the hot electron populations at SI intensities and plasma conditions. The NIF strong shock solid target (SSS) experiment uses PDD to observe a hot electron population with a temperature 56keV and a cumulative energy of 35kJ (an instantaneous energy fraction at  $n_{crit}/4$  of 0.2) for a SI laser pulse. The Omega laser (Laboratory for Laser Energetics, Boehly et al. [1997]), with total energy  $< 40$ kJ, was used in a novel geometry to achieve SI plasma conditions and laser intensities which resulted in a hot electron population with an observed 40keV temperature and energy fraction 0.025 at  $n_{crit}/4$ . The disparity in observed conversion fractions is an open problem for SI requiring more experimental investigation. Simulation for this thesis demonstrates that the NIF SSS population would lead to preheat near the maximum tolerable limit and require mitigation strategies (Rosenberg et al. [2018]) while the Omega conical target would cause only a minor deleterious effect.

# Acronyms

**ALE** Arbitrary Lagrangian-Eularian.

**CBET** Cross-Beam Energy Transfer.

**CDF** Cumulative Distribution Function.

**DT** Deuterium-Tritium.

**EOS** Equation of State.

**HEDP** High Energy Density Physics.

**IB** Inverse Bremsstrahlung.

**ICF** Inertial Confinement Fusion.

**IFE** Inertial Fusion Energy.

**MPFA** multi-point flux-approximation control-volume methods.

**NIF** National Ignition Facility.

**PDF** Probability Distribution Function.

**RT** Rayleigh-Taylor Instability.

**SBS** Stimulated Brillouin Scattering.

**SI** Shock Ignition.

**SPD** Symmetric Positive Definite.

**SRS** Stimulated Raman Scattering.

**TPD** Two Plasmon Decay.

**VFP** Vlasov Fockker-Plank.

# Chapter 1

## Introduction

### 1.1 Purpose of Fusion Energy

Energy surplus has catalysed every major change in society since the discovery of fire. The energy surplus of food created by agriculture allowed cities and specialization of professions, modern society is possible due to the extraction of energy from the easily accessible coal and oil. The first glimpse of the energy available within the atom was one of the darkest moments in human history, however it brought into view the next step for humanities' energy consumption, nuclear energy. Nuclear fission has provided a great opportunity for reduction in harmful atmospheric emissions, however nuclear fusion offers these benefits in addition to not producing the radioactive ground pollutants whose storage is an engineering challenge. It will not come soon enough to solve the current climate emergency and unlike many developments made in the 20th century, the completion of a productive fusion reactor may require international collaboration.

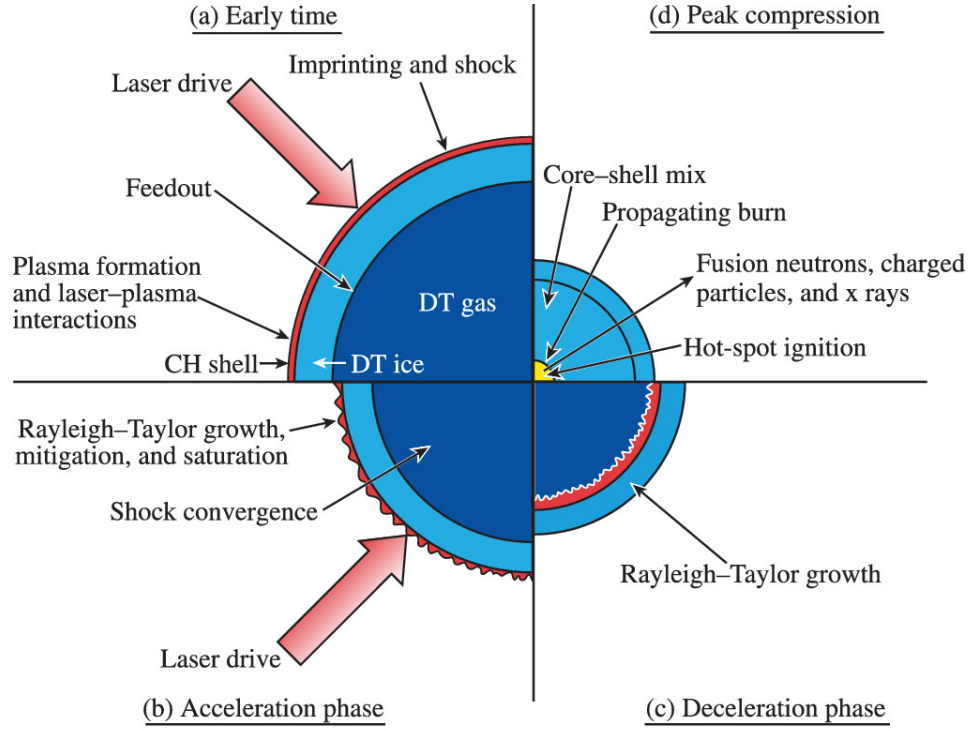
Climate change is the greatest existential threat facing humanity in the 21st century. The crisis which faces us requires the balance of energy usage of 1.2 billion people living above the poverty line (15% of people live on more than \$30 a day, see Roser and Ortiz-Ospina [2013]) with the finite resources that the world can provide. Within the next 100 years, humanity should aim to have  $\sim 10$  billion people living above the poverty line, sustainably. Despite the great benefits of solar and wind, these will not provide a long term global solution due to their material requirements, short life-span and energy storage requirements. Hydro and geothermal plants present a near perfect solution, however almost all safe sources have been utilized. Nuclear fission has the required energy density and reactor longevity to be a transitional solution to climate change, however even if all the

uranium within mining depth and the sea is utilized it will only provide humanity with its energy needs for  $\approx 100$  years (longer with breeder reactors). There are several possible solutions, including reducing the energy consumption per capita or controlling global population, but the only solution that does not involve invasive social intervention is an order of magnitude increase in clean energy production.

It is expensive to research nuclear fusion and countries involved must be trusted with hazardous material, however we cannot resolve a global energy crisis without a global approach. An individual nation's emissions can be large enough to undo global progress, so international cooperation is required. Since any solution requires cooperation, we must work toward the one that is most achievable. Nuclear fusion does not present an easy target; it requires temperatures several times larger than the centre of the Sun however it does offer a benefit over any comparable source, a plentiful, distributed supply of fuel. In theory, the fuel extracted from a glass of seawater can provide as much energy as a barrel of oil. The fuel is deuterium a naturally occurring isotope of hydrogen, along with tritium (which can be made in the reactor from lithium).

In order to effectively extract energy from a fuel, a chain reaction must occur. A chain reaction requires confinement of the fuel so that the reactants aren't blown apart by the initial energy release. For fusion the confinement methods are, gravitational, magnetic, and inertial. Gravitationally confined fusion occurs in stars, like the Sun, and directly or indirectly supplies humanity with almost all of our energy. Direct energy extraction is done with solar cells, efficiency can be improved with location, such as a desert or putting them in space. Better still, proximity to the Sun increases irradiance further increasing efficiency, however the enormous distance presents challenges for power transmission. Magnetic and inertial fusion allow us to create a star of our own and extract energy where it is needed. Magnetic confinement uses the charged material (plasma) to create a current and applies an external field to confine the current from the reactor wall by the Lorentz force. Magnetic fusion aims to keep the material heated over the seconds or minutes required to extract energy. Inertial confinement fusion for energy will be covered in this Thesis, in addition to original work presented in order to achieve it.

Inertial confinement fusion (ICF) occurs in nanoseconds, a timescale so small that when one has passed, light has not yet covered the distance of a metre. The creation and diagnosis of a high energy density plasma on this timescale constitutes a scientific and engineering frontier. The near perfect balance of complex phenomena required to initiate the chain reaction and ignite the plasma is still beyond our capabilities. Significant improvements are still being made in both creation and



E9886J1

Figure 1.1: Schematic showing the 4 main stages of laser direct drive, central hotspot ignition. Figure reproduced from Craxton et al. [2015].

diagnosis of the plasma and once ignition is achieved it is expected that break-even (energy production) will follow. The road toward creating a full size reactor is unknown and will test humanities ingenuity, however even the act of igniting a plasma will tell us about the powerhouses of the galaxy, the stars and the outflow of technology will improve our lives.

## 1.2 Inertial Confinement Fusion Energy

There are two main types of inertial fusion, direct and indirect drive. Direct drive imparts laser light onto the target to heat the outer edges and accelerate material away. Indirect drive puts the target within a gold can, by illuminating the inner surface of the can the laser light can be transferred from UV/infrared to x-ray frequency, and it is the x-ray light that drives the implosion. X-rays are thought to be a more efficient driver and less prone to create fluid instabilities due to their deeper target penetration, however the conversion of UV/infrared to x-ray light is inefficient so both direct and indirect drive are currently being pursued as viable options. The focus of this Thesis is on energy transport for direct drive fusion.

Laser direct drive fusion, as seen in the schematic Figure 1.1, uses direct laser illumination of a hollow sphere (shell/capsule/target) to heat and ablate the outer edge. The expanding, coronal plasma pushes the hollow shell inward via the rocket effect. As the laser light interacts with the coronal plasma, it deposits its energy only as far as the critical surface, beyond which it cannot propagate. The energy is deposited mostly into free electrons, and transport mechanisms spread the energy, accelerating and ionizing more of the target up to the ablation front. The pressure applied at the ablation front creates a wave that exceeds the sound speed, becoming a shock wave. The shock drives the target inward but also compresses, increasing the density of the capsule wall. As the shell is pushed inward, the velocity  $\sim 300\text{km/s} = 300\mu\text{m/ns}$ , leads to a kinetic energy  $\sim 100\text{kJ}$ . The hollow shell is filled with Deuterium-Tritium (DT) gas and stored at cryogenic temperatures ( $\sim 18\text{K}$ ) until the laser hits. As seen in Figure 1.1 the gas now pushes back on the imploding shell, further increasing density and the pressure exerted, until the back pressure is enough to stop the inflowing shell. Stagnation occurs, and the kinetic energy of the shell is transferred into internal energy of the central hotspot. The conditions in the hotspot are primed for nuclear fusion, and the dense DT shell is ready to absorb the fusion energy, starting a chain reaction and creating a burn wave. This is the basic theory of central hotspot ignition explored in this chapter, but also in more depth in Atzeni and Meyer-ter Vehn [2004]; Pfalzner [2006]; and Craxton et al. [2015].

In the first section (1.2.1), the conditions required to ignite the fuel are explained through the key concept of areal density. In the next section (1.2.2), the use of velocity to focus energy in the hotspot will be explored. In Section 1.2.3, the physics of shocks and adiabatic compression will be described. Section 1.2.4 covers laser energy deposition. In Section 1.2.5, energy transport will be discussed, although more depth will be given in Chapter 2. The issues for central hotspot ignition will be summarized in Section 1.3 and lastly a brief overview of the high energy density physics (HEDP) code Odin will be given in Section 1.4.

### 1.2.1 Alpha Particles and Areal Density

In order to fuse nuclei, first an atom must be stripped of its electrons (which occurs at temperatures  $\sim$  tens of eV), and then the charge repulsion of the nuclei must be overcome (temperatures of several keV). The likelihood that two nuclei will fuse is determined by their reaction cross-section,  $\langle\sigma v\rangle$  displayed in Figure 1.2 which can be seen in more detail in Atzeni and Meyer-ter Vehn [2004]. DT has the largest reaction cross-section at the temperatures currently achievable  $T < 10^8\text{K}$ . The products of DT fusion are a helium nucleus (referred to as an alpha particle), a neutron, and



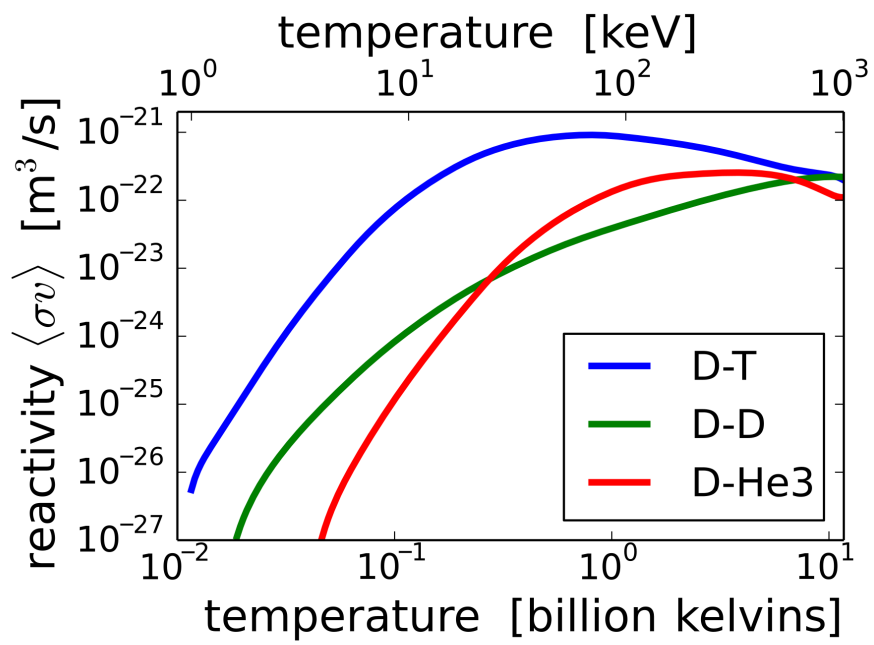


Figure 1.2: Nuclear reactivity (or reaction cross-section  $\langle \sigma v \rangle$ ) for the three lowest temperature fusion reactions. The peak of the blue curve (DT) is at a temperature  $\sim 10^8 \text{K} \sim 10 \text{keV}$ . Figure reproduced from Wikipedia Dstrozzi [2020].

$\sim 18\text{MeV}$  of energy. Of the energy,  $\sim 14\text{MeV}$  is carried away by the neutron and  $E_\alpha \approx 3.5\text{MeV} \approx 5.6 \times 10^{-13}\text{J}$  is carried by the alpha particle.

The rate nuclear fusion releases energy at  $T \sim 10^8\text{K}$  is approximately  $\propto n^2 T^2$ , where  $n$  is the number density of fuel ions (assuming equal parts deuterium and tritium) and  $T$  is the temperature. The fusion energy released can be expressed  $P_\alpha = \beta n^2 T^2$ , where  $\beta = \frac{1}{4} E_\alpha \langle \sigma v \rangle = 1.1 \times 10^{-51} [\text{J m}^3 \text{s}^{-1}]$ . In addition, energy loss from the area,  $P_L = W/\tau_E = 3nk_B T/\tau_E$ , where  $W = 3nk_B T$  is the energy stored in the 2 species at the reaction site (electrons and ions) and  $\tau_E$  is the characteristic loss timescale (energy confinement time). By balancing these ( $P_\alpha \geq P_L$ ), the conditions for a self-sustaining fusion reaction can be derived,

$$\begin{aligned} nT\tau_E &\geq \frac{3k_B}{\beta} \\ &\geq 3.5 \times 10^{28} [\text{K s m}^{-3}], \end{aligned} \tag{1.1}$$

an ICF implosion aims to fulfil this criterion with  $n \sim 10^{31}\text{m}^{-3} \sim 500n_0$ ;  $T \sim 10^8\text{K} \sim 7\text{keV}$  and  $\tau_E \sim 10^{-10}\text{s} \sim 0.1\text{ns}$  where  $n_0$  is solid density and  $1[\text{eV}] = e/k_B[\text{Kelvin}]$ . From Equation 1.1, a dimensionless ignition parameter can also be defined  $\chi = 3 \times 10^{28}/(nT\tau_E)$ .

To limit the parameter space further, the mass of the fuel is defined by the maximum energy that can be contained within a reactor. 1mg of DT can release about  $\approx 0.1\%$  of its mass as energy  $E = mc^2 \approx 100\text{MJ} \approx 25 \text{ kg of TNT}$ . Converting energy to electrical power has inefficiencies, meaning that a reactor needs approximately a gain of  $\times 100$  the energy input. Putting these two figures together, we can see that the driver of the  $\sim 1\text{mg}$  of fuel must be less than  $\sim 1\text{MJ}$ .

Equation 1.1 defines when a fusion reaction site (hotspot for ICF) is self-sustaining, but it can be rephrased in terms of parameters relevant for an implosion. A chain reaction (burn) occurs when more energy is captured in the hotspot than lost. The high energy neutron is uncharged, and the majority will leave the capsule. In order to create a chain reaction, the alpha particle needs to deposit energy before leaving the capsule. The term areal density is devised to represent the amount of material a particle will interact with along its trajectory out of the capsule. Rather than devising a trajectory specific areal density, we consider the mean free path of an alpha particle created at the centre of the target and define areal density radially,  $\rho R = \int \rho dr$ , where  $\rho$  is density and  $R$  is radius. To restate Equation 1.1 in terms of  $\rho R$ , the hotspot disassembly time ( $\tau_E$ ) can be estimated by the speed of sound in

the hotspot ( $C_s \sim v_{th} = (k_B T/m_i)^{1/2}$ ), assuming spherical symmetry,

$$\tau_E = \frac{R}{4v_{th}} \quad (1.2)$$

where  $R$  is the radius of the target and the factor of 4 arises due to the spherical geometry of the target (Fraley et al. [1974]).  $\tau_E$  is the time taken for a pressure wave to travel from the inner surface, of the shell to the centre of the hotspot immediately after stagnation. Using Equation 1.1, 1.2, and  $n = \rho/m_i = \rho/(2.5m_p)$ ,

$$\begin{aligned} \rho R &> 3.5 \times 10^{28} \sqrt{\frac{2.5m_p T}{k_B}} \times 4 \\ &> 3.0[\text{kg/m}^{-2}] = 0.3[\text{g/cm}^{-2}] \end{aligned} \quad (1.3)$$

a similar derivation can be found in Fraley et al. [1974]. To achieve this areal density using uncompressed DT at solid density,  $\rho_{DT} \approx 0.2\text{g/cm}^3$  you would require a sphere with radius  $\approx 1.5\text{cm}$  which would weigh  $\approx 3\text{g}$  equivalent to  $\approx 300\text{GJ} \approx 30$  tons of TNT. For a reactor, we instead use a hotspot  $M_{hs} \approx 0.01\text{mg}$  compressed to  $\approx 500$  times solid density, which gives a hotspot radius of  $\approx 10^{-4}\text{m} = 100\mu\text{m}$ . The mass of the hotspot  $M_{hs} \ll M_{fuel}$  to achieve efficient drive and energy confinement.

An areal density of  $\approx 0.2\text{g/cm}^{-2}$  is required to ignite the hotspot. The total burn fraction of the fuel ( $\Phi$ ) is determined by the total areal density ( $\rho R_{tot}$ , hotspot and cold fuel),

$$\Phi \approx \frac{\rho R_{tot}}{7[\text{g/cm}^2] + \rho R_{tot}} \quad (1.4)$$

requiring  $\rho R_{tot} \approx 3\text{g/cm}^2$  for  $\approx 30\%$  burn efficiency (Fraley et al. [1974]; Atzeni and Meyer-ter Vehn [2004]) which appears to be a much more limiting criterion. The cold, dense fuel in the outer shell is required to achieve efficient burn, however the shell does not reach the temperature required for self-ignition using Equation 1.3. It is the combination of ignition in the central hotspot (at high temperatures and low density) and the areal density of the shell (low temperatures and high densities) which aims to fulfil the criteria in Equation 1.3 and 1.4 giving nuclear burn fractions  $> 10\%$ .

Zhou and Betti [2008] use 1D simulation to put an ignition criterion in terms of total areal density  $\rho R_{tot}$  and hotspot temperature  $T_{hs}$ ,

$$\chi \approx \left( \frac{\rho R_{tot}}{0.5[\text{g/cm}^2]} \right) \left( \frac{T_{hs}}{6[\text{keV}]} \right)^{2.6} \quad (1.5)$$

where  $\rho R_{tot}$  is the areal density of the hotspot and cold fuel. The aim of which is

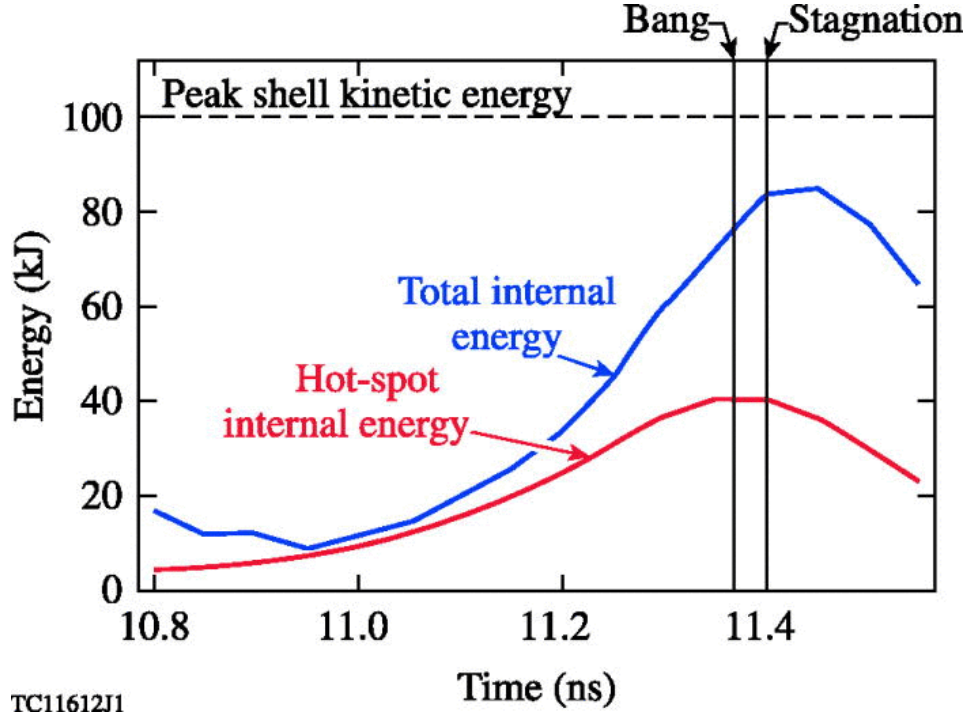


Figure 1.3: Capsule energy transfer over the course of an implosion. It shows  $\approx 100\text{kJ}$  peak kinetic energy converted with  $\theta < 0.5$  efficiency to the hotspot. Improved efficiency can be achieved with a larger radius, thinner shell, however this also leads to hydrodynamic instabilities. Figure reproduced from Craxton et al. [2015].

to give a measurable ignition parameter using neutron diagnostics.

### 1.2.2 Implosion Velocity

The focusing of energy and density is achieved through spherical convergence of the imploding shell. The pressure in the hotspot builds until it stops the inertia of the imploding shell. At stagnation, the energy exchange in the hotspot can be rearranged to determine the implosion velocity of the shell needed to create fusion conditions,

$$\begin{aligned} \frac{4\pi}{3} R_{hs}^3 n k_B T_{hs} &= \frac{\theta}{2} M_{sh} V_{imp}^2 \\ V_{imp} &= \sqrt{\frac{8\pi R_{hs}^3 n k_B T_{hs}}{3\theta M_{sh}}} \end{aligned} \quad (1.6)$$

where  $T_{hs} \approx 10^8\text{K}$  is the hotspot temperature,  $M_{sh} \approx 1\text{mg}$  is the mass of the imploding shell,  $n \approx 10^{31}\text{m}^{-3}$  is the number density in the hotspot,  $R_{hs} \approx 10^{-4}\text{m}$  is the hotspot radius,  $\theta \approx 0.5$  is the fraction of shell kinetic energy converted to hotspot

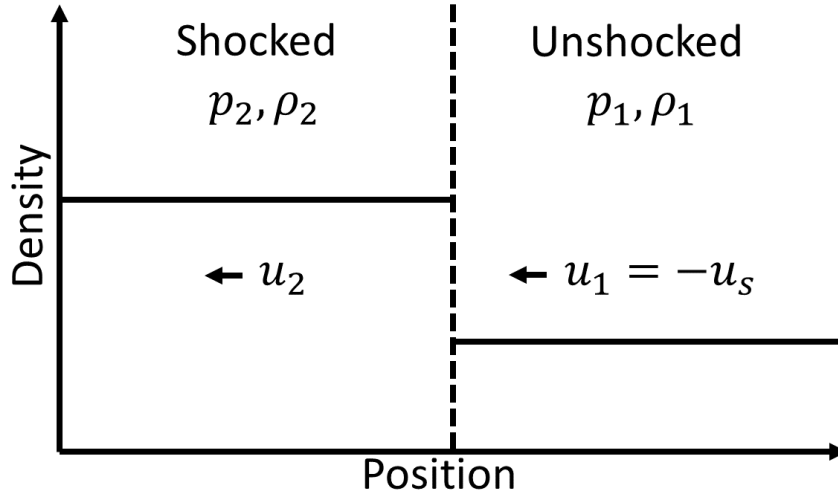


Figure 1.4: Image in the rest frame of a shock. The density and pressure of the fluid increase as it passes through the shock, but velocity decreases, from  $u_1$  to  $u_2$ , to conserve mass at the shock front. In the lab rest frame the shock would be travelling at a velocity  $u_s$  left to right into stationary fluid defined by subscript 1 and accelerating it to a velocity  $u_2 - u_1$ .

internal energy, and  $V_{imp}$  is the velocity the shell travels at. Using these numbers, the hotspot internal energy is  $\approx 50\text{kJ}$  and implosion velocity  $V_{imp} \approx 480\text{km/s}$ . The energy exchange for an ICF simulation is similar and can be seen in Figure 1.3.

### 1.2.3 Adiat and Shocks

Before the implosion, the cold DT fuel is nearly electron Fermi-degenerate which can be maintained throughout the implosion using isentropic compression (maintaining entropy). Isentropic compression is possible with an infinite number of small shocks which is experimentally infeasible. Instead, near adiabatic compression (without heat transfer) is achieved with several strong shocks. To measure the success of the compression compared to the low entropy initial state, an adiabat is defined (Craxton et al. [2015]; Atzeni and Meyer-ter Vehn [2004]),

$$\alpha_{\text{DT}} = \frac{P}{2.17 \times 10^{17} \rho^{5/3}}, \quad (1.7)$$

where  $P$  is pressure and  $\rho$  is density. An adiabat  $\alpha = 1$  implies the equimolar DT is electron Fermi-degenerate. The mass averaged adiabat in the cold fuel is commonly quoted for an implosion and will be used from now on in this work. It is possible to carry out an ICF implosion with,  $\alpha < 1.5$  however it has been shown to lead to

more hydrodynamic instabilities (Goncharov et al. [2003]).

In an ideal gas ( $\gamma = 5/3$ ), a strong planar shock can achieve a density increase of  $4 \approx \rho_{\text{shocked}}/\rho_{\text{unshocked}}$ , although with real equations of state (EoS) this is not exact. Shock physics is critical for the compression required by ICF. The phenomena of shock creation and propagation will be derived. A more thorough treatment can be found in Zel'Dovich and Raizer [2002] or Drake [2006]. Starting from single-fluid hydrodynamics equations,

$$\begin{aligned}\frac{\partial \rho}{\partial t} &= -\nabla \cdot (\rho \mathbf{u}) \\ \frac{\partial}{\partial t}(\rho \mathbf{u}) &= -\nabla \cdot (\rho \mathbf{u} \mathbf{u}) - \nabla P, \text{ and} \\ \frac{\partial}{\partial t} \left( \frac{\rho u^2}{2} + \rho e \right) &= -\nabla \cdot \left[ \rho \mathbf{u} \left( e + \frac{u^2}{2} \right) + P \mathbf{u} \right].\end{aligned}\tag{1.8}$$

where  $e$  is the specific internal energy and  $\mathbf{u}$  is the velocity. To close the equations an ideal EoS is used, however more accuracy over a larger range can be achieved with a semi-empirical, tabulated EoS. The ideal EoS is,

$$\rho e = \frac{P}{\gamma - 1}\tag{1.9}$$

where  $\gamma$  is the adiabatic index. A shock is a pressure wave that moves faster than the sound speed. Rather than spreading out, the tail of the pressure wave travels faster than the front since the sound speed is higher in material that has been compressed. The wave becomes spatially small until it is almost a discontinuous change in fluid properties, as shown in Figure 1.4. Pressure waves (sound waves) become shocks if they exceed a limit in amplitude, approximately twice the pressure of the ambient fluid.

To resolve the issue of a discontinuous change in a continuous fluid, Equation 1.8 must be matched either side of the shock (dashed line in Figure 1.4),

$$\begin{aligned}\rho_1 u_1 &= \rho_2 u_2, \\ \rho_1 u_1^2 + P_1 &= \rho_2 u_2^2 + P_2, \\ \left[ \rho_1 u_1 \left( e_1 + \frac{u_1^2}{2} \right) + P_1 u_1 \right] &= \left[ \rho_2 u_2 \left( e_2 + \frac{u_2^2}{2} \right) + P_2 u_2 \right],\end{aligned}\tag{1.10}$$

where we are considering the 1D motion in Figure 1.4 and the material parameters before and after the shock are described by subscript 1 and 2 respectively. Rearranging (assuming constant  $\gamma$ ) for pressure and density ratios respectively we get,

$$\frac{P_2}{P_1} = \frac{\rho_2(\gamma + 1) - \rho_1(\gamma - 1)}{\rho_1(\gamma + 1) - \rho_2(\gamma - 1)} \quad (1.11)$$

and,

$$\frac{\rho_2}{\rho_1} = \frac{u_1}{u_2} = \frac{P_2(\gamma + 1) + P_1(\gamma - 1)}{P_1(\gamma + 1) + P_2(\gamma - 1)} \quad (1.12)$$

which in the limit of  $P_2 \gg P_1$  the density ratio becomes,

$$\frac{\rho_2}{\rho_1} = \frac{(\gamma + 1)}{(\gamma - 1)} \quad (1.13)$$

which, with  $\gamma = 5/3$  gives the value  $\rho_2/\rho_1 = 4$  for planar shocks. When a shock converges spherically, the maximum compression ratio for  $\gamma = 5/3$  is  $\rho_2/\rho_1 = 32$  derived in Guderley [1942] and generalized in English in Meyer-ter Vehn and Schalk [1982].

The specific entropy change in the system shown in Figure 1.4 can be written,

$$s_2 - s_1 = c_V \ln \left( \frac{P_2 \rho_1^\gamma}{P_1 \rho_2^\gamma} \right) \quad (1.14)$$

in the limit of  $(P_2 \rho_1^\gamma)/(P_1 \rho_2^\gamma) \rightarrow 1$  the shock is isentropic otherwise kinetic energy is converted to thermal energy as it travels, and the process is irreversible.

#### 1.2.4 Laser Driver

High energy lasers turn materials into plasmas by ionizing the atoms, they also increase the pressure, ablating the surface. The first instant ( $< 100\text{ps}$ ) of the expansion/absorption is atypical and will be neglected in this description (see Pfalzner [2006] for a more thorough investigation). After the initial stage, the ablated plasma follows approximately an exponential decrease in density away from the target. Once a plasma has been formed, the material can be split into four regimes where different phenomena dominate as denoted by the dashed lines in Figure 1.5. The lines demarcate the quarter critical surface ( $n_c/4$ ), the critical surface ( $n_c$ ), and the ablation front respectively. The critical surface can be defined,

$$n_c = \frac{\epsilon_0 m_e \omega_L^2}{4\pi e^2} \quad (1.15)$$

where  $\omega_L$  is the laser angular frequency (more explanation of  $n_c$  in Chapter 4). At this density, light incident normal to the density gradient would undergo resonant absorption (electromagnetic waves resonate with oscillations in the electron fluid). Laser plasma interactions can occur in the under-dense plasma up to  $n_c$  however

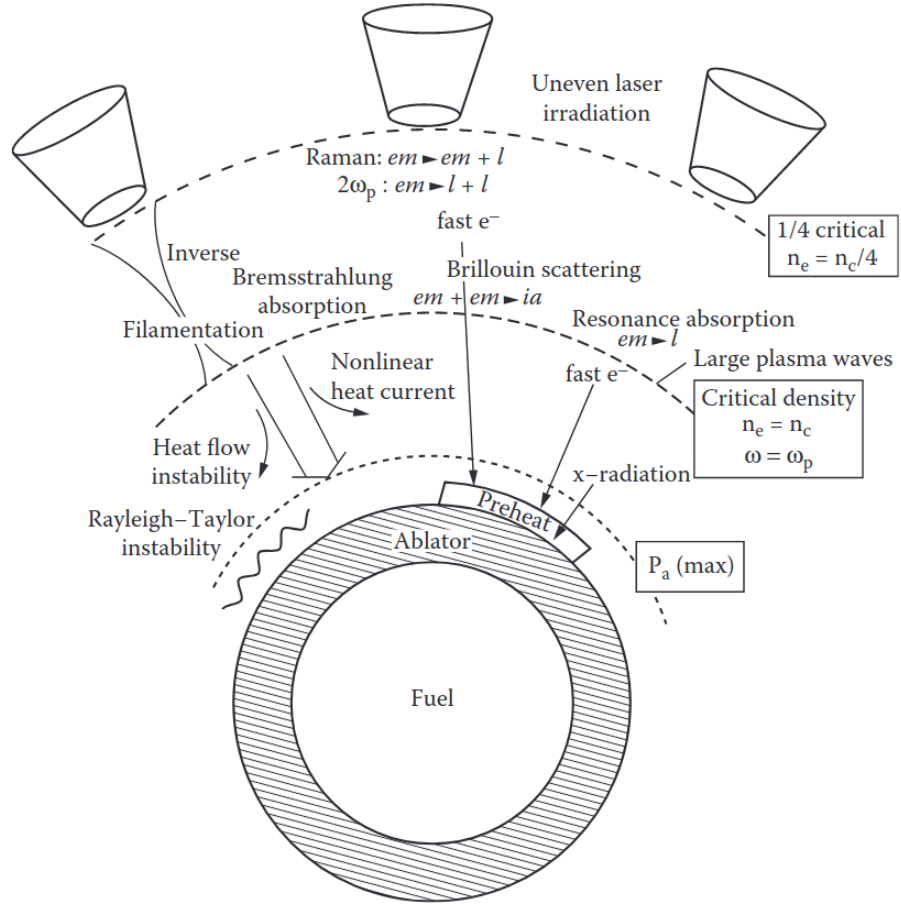


Figure 1.5: Schematic of the phenomena that might occur as the electromagnetic wave created by the laser travels up the density gradient toward the critical surface. The shorthand “em” denotes electromagnetic wave with the arrow showing the result of laser plasma interaction giving either, em as backscattered light, “l” meaning Langmuir (electron plasma) waves or “ia” ion acoustic wave (More detail on plasma waves can be found in Chapter 4). Image reproduced from Pfalzner [2006].



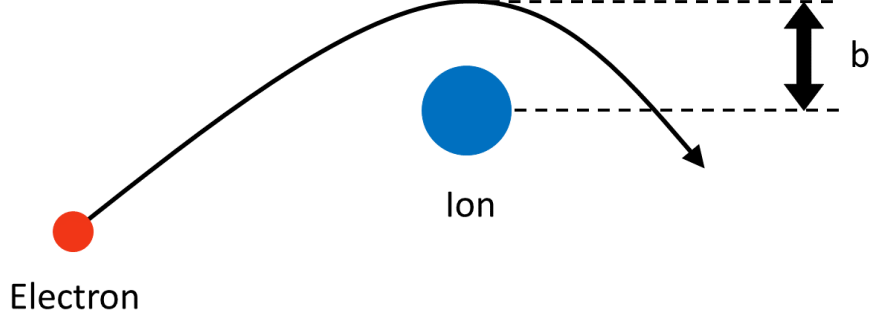


Figure 1.6: Schematic of electron’s closest approach  $b$  as it collides with an ion in the plasma. This is a classical reduction of a quantum physics interaction. If the electron also absorbs a photon as it accelerates around the ion then this is an inverse bremsstrahlung event.

the type of LPI that occur changes at  $\approx n_c/4$  described in Kruer [2019], after  $n_c/4$  is where the majority of the laser energy is deposited for standard ICF conditions, beyond the critical density is an over-dense plasma through which the laser light can not propagate, and this region is dominated by energy transport up to the ablation front (sometimes called the stand-off distance). The ablation front is where density gradients that slow energy transport balance with temperature gradients, which increase energy transport. Beyond the ablation front is the shock compressed ablator (often made of plastic) and the cold fuel.

Most laser photons are not incident normal to the critical surface and undergo refraction or reflection before reaching the critical density. Inverse bremsstrahlung (IB) is the dominant absorption process for low intensity lasers ( $< 10^{15} \text{ W/cm}^2$ , also laser frequency dependant, Pfalzner [2006]). In Section 3.8.1 this Thesis presents original work in developing a laser ray trace model with IB deposition, so a classical physics derivation will be performed, stating the modification due to quantum effects. IB occurs when a free electron is accelerated around an ion by a photon. The schematic in Figure 1.6 shows an electron-ion collision, the mean time  $\tau_{90}$  for an electron to scatter  $90^\circ$  from its initial path is required to determine IB energy deposition. Following the derivation seen in Kruer [2019] the maximum electrostatic

force on the electron is,

$$F_{max} = \frac{-Ze^2}{4\pi\epsilon_0 b^2} \approx m_e \frac{\Delta v}{2b/v} \quad (1.16a)$$

$$\Delta v = \frac{-Ze^2}{2\pi\epsilon_0 m_e b} \quad (1.16b)$$

where,  $Z$  is the ion's charge state,  $b$  is the electron's nearest distance to the ion, the electron's velocity change  $\Delta v$  occurs over an interaction time of  $\Delta t \approx 2b/v$ . The ion's mass is large compared to the electron, and it is assumed to be unaffected in the interaction. For many random interactions, the mean electron velocity change  $\langle \Delta v \rangle = 0$ , since the plasma is isotropic. The mean-squared value for  $\langle \Delta v^2 \rangle$  does change, which reflects the dynamic equilibrium of energy between particles. Summing for all collisions over path length  $v\Delta t$ ,

$$\begin{aligned} \langle \Delta v^2 \rangle &= 2\pi n_i \int_{b_{min}}^{b_{max}} b \Delta v^2 db v \Delta t \\ &= 2\pi n_i v \frac{\Delta v^2}{b^2} \int_{b_{min}}^{b_{max}} \frac{1}{b} db \Delta t \\ &= \frac{Z^2 n_i e^4}{2\pi \epsilon_0^2 m_e^2 v} \ln \left( \frac{b_{max}}{b_{min}} \right) \Delta t \end{aligned} \quad (1.17)$$

the Coulomb logarithm features  $b_{max}$  and  $b_{min}$  which need to be determined since the function  $[\log b]_0^\infty$  is not defined. The derivation so far has relied on a simplified approach, but the correct derivation of the limits relies on full particle kinetics, which is seen in Bornath et al. [2001] for dense plasmas of interest to ICF. The Coulomb logarithm is a key concept for electron interactions and will be seen again in Equation 1.27 for electron thermal conduction and Equation 5.11b for hot electron energy deposition. It can be approximated by,

$$b_{max} \approx \lambda_D = \sqrt{\frac{\epsilon_0 k_B T_e}{e^2 n_e}} \quad (1.18a)$$

$$b_{min} \approx \frac{Ze^2}{4\pi\epsilon m_e v^2} \quad (1.18b)$$

$$\ln \Lambda \equiv \ln \left( \frac{b_{max}}{b_{min}} \right) \approx \ln \left( \frac{12\pi(\epsilon k_B T_e)^{3/2}}{Ze^3 n_e^{1/2}} \right). \quad (1.18c)$$

where the Debye length  $\lambda_D$  is described in Chapter 4 and  $b_{min}$  is the point at which

the coulomb potential energy equals the electron's kinetic energy. From Equation 1.17 we can get  $\tau_{90}$  the  $90^\circ$  collision time by equating the root-mean-squared (RMS) change in velocity to the electron's velocity,  $\langle \Delta v^2 \rangle \approx v^2$  and  $\Delta t = \tau_{90}$  resulting in the  $90^\circ$  turning time for a single particle,

$$\tau_{90} = \frac{4\pi\epsilon_0^2 m_e^2 v^3}{Z^2 e^4 n_i \ln \Lambda} \quad (1.19)$$

where it is useful to define the electron thermal speed  $v_T = \sqrt{2k_B T_e / m_e}$  and average over a Maxwellian distribution resulting in a factor  $3\sqrt{\pi}/4$  to get the  $90^\circ$  turning time for a thermal distribution,

$$\tau_{ei} = \frac{3\epsilon_0^2 \sqrt{m_e} (2\pi k_B T_e)^{3/2}}{Z^2 e^4 n_i \ln \Lambda} \quad (1.20)$$

which is the expression needed to calculate the laser energy deposition by inverse bremsstrahlung absorption, however it is a fundamental part of plasma physics since it also determines electron-ion equilibration time.

Inverse bremsstrahlung, is the absorption of laser light into a thermal population of electrons. The thermal collision time between electrons and ions ( $\tau_{ei}$ ) has been defined, but to determine deposition, the interaction between the electromagnetic (EM) field and the plasma must also be quantified. The acceleration of an electron due to a laser created electric field  $|\mathbf{E}| = E_0 \sin \omega_L t$  is,

$$\begin{aligned} \ddot{x} &= -\frac{e|\mathbf{E}|}{m_e} = -\frac{eE_0}{m_e} \sin \omega_L t \\ \dot{x} &= \frac{eE_0}{m_e \omega_L} \cos \omega_L t. \end{aligned} \quad (1.21)$$

The kinetic energy given to the electron averaged over an EM oscillation is,

$$\left\langle \frac{1}{2} m_e \dot{x}^2 \right\rangle = \frac{m_e}{4} \left( \frac{eE_0}{m_e \omega_L} \right)^2, \quad (1.22)$$

using this, the rate of energy lost from the laser ( $dU_L/dx$ ) to electrons ( $n_e$ ) within an area  $A$  can be defined (per unit length),

$$\frac{dU_L}{dx} = -\frac{t}{\tau_{ei}} n_e A \left( \frac{e^2 E_0^2}{4m_e \omega_L^2} \right) \quad (1.23)$$

where the electron-ion collision time  $\tau_{ei}$  is defined in Equation 1.20. The total laser

energy in an area  $A$  over time  $t$  can be written in terms of laser intensity  $I$ ,

$$U_L = IAt = \frac{1}{2} \sqrt{1 - \left( \frac{\omega_{pe}}{\omega_L} \right)^2} \epsilon_0 E_0^2 cAt \quad (1.24)$$

the term in the square root is the dielectric permittivity  $\epsilon_r$  which for a plasma is defined by the electron plasma wave  $\omega_{pe} = \sqrt{e^2 n_e / m_e \epsilon_0}$  (defined in Chapter 4). Rearranging Equation 1.24 for  $E_0$  and substituting into Equation 1.23 we get,

$$\frac{dU_L}{dx} = -\kappa_{IB} U_L = - \frac{n_e e^2}{2c\tau_{ei} m_e \omega_L^2 \sqrt{1 - \left( \frac{\omega_{pe}}{\omega_L} \right)^2}} U_L \quad (1.25)$$

which gives laser energy absorption into a medium in terms of the inverse bremsstrahlung absorption coefficient  $\kappa_{IB}$  and where  $\tau_{ei}$  is from Equation 1.20. The derivation given above is simplified. A complete derivation (Bornath et al. [2001]) gives the coefficient,

$$\kappa_{IB} = \frac{Z^2 n_i n_e e^6 \ln \Lambda}{3\epsilon_0^3 c (2\pi m_e k_B T_e)^{3/2} \omega_L^2 (1 - \omega_p^2 / \omega^2)^{1/2}} \quad (1.26)$$

and is the same coefficient given in Equation 3.31.

Alongside IB absorption, Laser plasma instabilities (LPI) can occur up to the critical surface ( $n_c$ ) however these will be explored more fully in Chapter 4. LPI lead to less laser energy being coupled into thermal energy in the plasma. Figure 1.5 shows that LPI can produce backscattered light (electromagnetic waves), hot electrons (electron plasma waves/langmuir waves) or ion acoustic waves. LPI become worse at higher intensities and longer wavelengths. Energy coupling of laser light to target has long been a focus of high energy plasma research, resulting in the use of frequency tripled Nd:YAG lasers at the National Ignition Facility (NIF, Miller et al. [2004]), Laser Megajoule (LMJ, Fleurot et al. [2005]) and OMEGA Laser (Boehly et al. [1997]) which is the shortest wavelength laser that can be scaled to Megajoule facilities currently. Shock ignition schemes, discussed in Section 1.3, enter a new intensity regime ( $I > 10^{15} \text{W/cm}^2$ ) which has now brought focus onto the amount of hot electrons generated and their effect on the target. The effects of hot electrons will be explored in Chapters, 4, 5 and 6.

### 1.2.5 Energy Transport

Energy transport occurs throughout an ICF implosion, however there are two key points where it plays a dominant role: transferring energy from where the laser

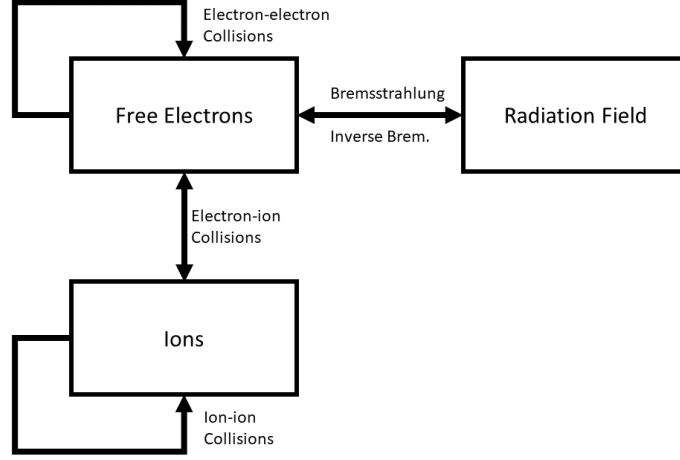


Figure 1.7: Three fluid system used to simulate HEDP, made up of free electrons, ions and a radiation fluid. The (dominant) interactions between the fluids are shown with arrows, including the looping arrows which represent relaxation time to establish thermodynamic equilibrium and set the particle distribution to a Maxwellian.

deposits via IB (at  $n_e < n_c$ ) to the ablation front, and transferring energy from the hotspot to the cold fuel. There are also two main types of energy diffusion that occur in HEDP, radiation transport and electron thermal conduction (ion conduction also occurs but due to the high ion mass and fast ion-electron equilibration time it is secondary to electron conduction). The terms diffusion and conduction will be used interchangeably in this Thesis. The focus of Chapter 3 will be electron thermal conduction, which can be directly applied to ion conduction (with modification of a coefficient shown in Chapter 2) and less directly to radiation transport (using multi-group diffusion). A derivation of electron thermal conduction from the plasma kinetic equation will be demonstrated in Chapter 2, but this section will continue to outline some key features assuming the result of the derivation.

On a macroscopic scale, it is common to apply a three fluid approximation as seen in Figure 1.7 where each fluid is individually in thermodynamic equilibrium, but the temperature of each fluid can be different. When the collisions shown in Figure 1.7 take place in the presence of a temperature gradient, there is a favoured direction of motion (mean free path is longer in one direction than another) and energy transport occurs. The transport is diffusive, reducing maxima and increasing

minima. The equation governing electron thermal diffusion is,

$$\rho c_v \frac{d(T_e)}{dt} = -\frac{d}{dx} \left( \kappa(T) \frac{dT_e}{dx} \right) \quad (1.27)$$

where the spatial axis  $x$  is aligned with the temperature gradient  $dT_e/dx$ ,  $n_e$  is the electron number density,  $c_v = (\partial e / \partial T)_v$  is the specific heat capacity (and  $e$  is the internal energy per unit mass) and  $\kappa$  is the conduction coefficient given by (Braginskii [1965]),

$$\kappa(T) = \kappa_0 T_e^{\frac{5}{2}} \quad (1.28a)$$

$$\kappa_0 = f(Z) \frac{12\pi^{3/2} \epsilon_0^2 k_B^{7/2}}{e^4 \sqrt{2m_e} \ln \Lambda} \quad (1.28b)$$

where  $\kappa_0$  has units  $[\text{J m}^{-1} \text{s}^{-1} \text{K}^{-1}]$ ,  $\ln \Lambda$  is the Coulomb logarithm and  $f(Z)$  is a charge dependant term defined in Chapter 2 (Epperlein and Haines [1986]). The equation above is for an unmagnetized plasma. Modification to the electron thermal conduction model shown in Equation 1.27 is required for, Fermi-degenerate, strongly coupled and relativistic plasmas. In addition, changes must be made for steep temperature gradients (which violate  $\lambda_{mfp} \ll L$ ).

Thermal conduction moves energy from where it is deposited by the laser to the ablation surface. It also helps to smooth non-uniformities in energy deposition, which can be due to laser beam alignment or target non-uniformities. Despite the smoothing effect of thermal conduction asymmetries are one of the most disruptive factors in an ICF implosion, moving experimental energy yields far from 1D simulation. These issues will be explored in the next section.

### 1.2.6 Summary of Issues

The most significant issue for direct drive laser fusion are asymmetries, leading to hydrodynamic instabilities. ICF implosions require high velocities and low adiabats creating the perfect environment for hydrodynamic instabilities (Lindl and Mead [1975]). These instabilities can seed from sub-micron surface roughness on the target, from laser imprint or the target stalk (used to fill the target and hold it in place). The instabilities disrupt an implosion by mixing materials, reducing the purity of the fuel and cooling the hotspot, but they can also lead to loss of confinement if the shell breaks apart.

The Rayleigh-Taylor (RT) instability occurs when a dense fluid is accelerated by a less dense fluid. A small perturbation grows into the characteristic “fingers”

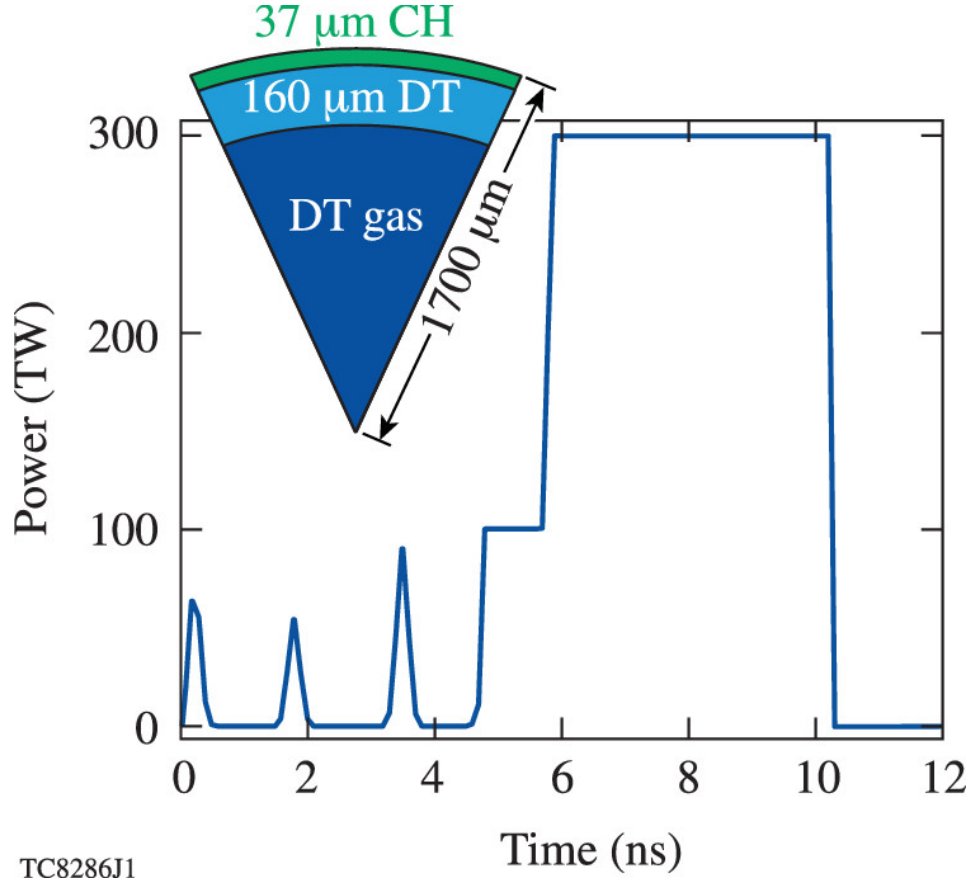


Figure 1.8: Target and laser pulse shape predicted to give energy gain of 48 times larger than incident laser energy of 1.5MJ. (Top, Left) Capsule layout with DT central gas region, DT shell and CH plastic ablator all cooled to cryogenic temperatures. (Axes) A laser pulse shape assumed to be emitted with spherical uniformity. The power is from all incident beams. The drive phase which generates the majority of the kinetic energy is between 6.0 – 10.5ns. All features before 6ns are to set the adiabat of the implosion and create compressional shocks. There are 3 “picket pulses” at  $\approx 0.5$ ns,  $\approx 1.9$ ns and  $\approx 3.7$ ns (Goncharov et al. [2003]). There is a “foot” between 4.8 – 6.0ns (Dittrich et al. [2014], terminology more common to indirect drive ICF). Peak velocity of the shell occurs at  $\approx 10.0$ ns and stagnation occurs at  $\approx 11.5$ ns. Ignition occurs at  $\approx 11.3$ ns and the burn fraction is predicted to be 20% of the DT fuel. Figure reproduced from Craxton et al. [2015].

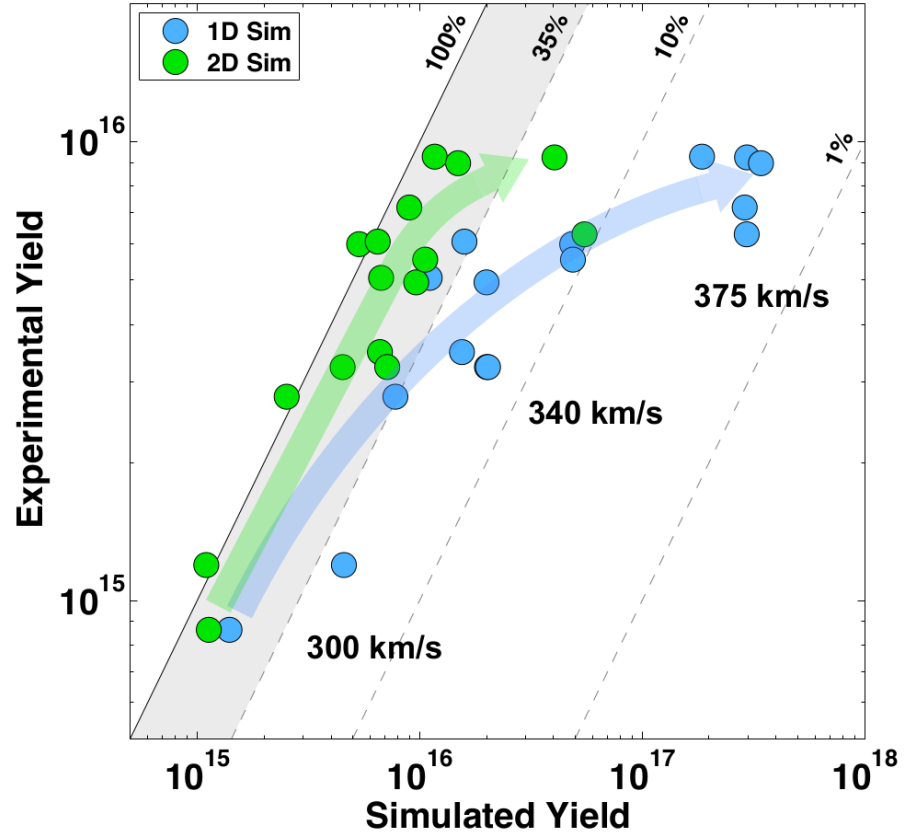


Figure 1.9: Predictive capabilities of 1D (blue) and 2D (green) simulations compared to experiment for different implosion velocities. Dashed lines represent the loss in yield compared to experiment. They also correspond approximately to increased implosion velocities. The high velocity implosions that show large yields in 1D, but the growth of hydrodynamic instabilities mean that both experiment and 2D simulation see no net benefit from increasing implosion velocity to the speeds required for ignition. Figure reproduced from Presentation by Richard Town, NIF, 2017



of RT, and finally the movement of the two fluids past one another seeds a Kelvin-Helmholtz instability. The rate of RT growth ( $\gamma$ ) is governed by (Lindl and Mead [1975]; Takabe et al. [1983]),

$$\gamma = \sqrt{Akg} - \beta kv_{abl} \quad (1.29a)$$

$$A = \frac{\rho_1 - \rho_2}{\rho_1 + \rho_2} \quad (1.29b)$$

where  $k$  is the wave-mode,  $g$  is the acceleration,  $v_{abl}$  is the ablation velocity,  $A$  is the Atwood number (where  $\rho_1$  is the heavier fluid and  $\rho_2$  the lighter) and  $\beta$  is a constant, dependent on the interface and defined empirically (see Craxton et al. [2015] for values). Stabilization of the highest modes is achieved by ablating mass from the target (“Fire-polish”) thus it is the intermediate modes that cause the most disruption. It was found Craxton et al. [2015] that modes with approximately the same length as the shell thickness were the biggest issue for ICF experiments. Laser pickets, seen in Figure 1.8, can be used to increase the ablation velocity  $v_{abl}$  without increasing acceleration  $g$  (Goncharov et al. [2003]).

A lower implosion velocity leads to lower acceleration and deceleration mitigating RT. Figure 1.9 shows that experiment (with indirect-drive) can achieve stable implosions with  $v_{imp} < 300\text{kms}^{-1}$  however these implosions have neither the kinetic energy nor areal density required to ignite. Higher velocities cause faster instability growth, degraded yield and no net benefit. The velocity limit for stable implosions is,  $v_{imp} < 300\text{kms}^{-1}$  and a similar limit for adiabat  $\alpha > 3$  can be found empirically (Craxton et al. [2015]). A higher adiabat reduces fuel compressibility, but it also increases ablation velocity and reduces RT growth.

### 1.3 Shock Ignition

The aim of shock ignition is to ignite a low velocity and low convergence implosion with a large impulse of laser energy as the shell reaches peak velocity. This mitigates many of the hydrodynamic issues discussed in the previous section. The impulse generates a shock that travels through the shell and collides with the back pressure wave from the stagnating inner surface. The collision of the shocks creates a non-isobaric hotspot with pressure and ion temperature peaked at the centre, starting fusion. The shock also compresses the cold fuel to an areal density necessary to stop the alpha particles and ignite the target Betti et al. [2007]. Shock ignition is explained in more detail in Chapter 6.

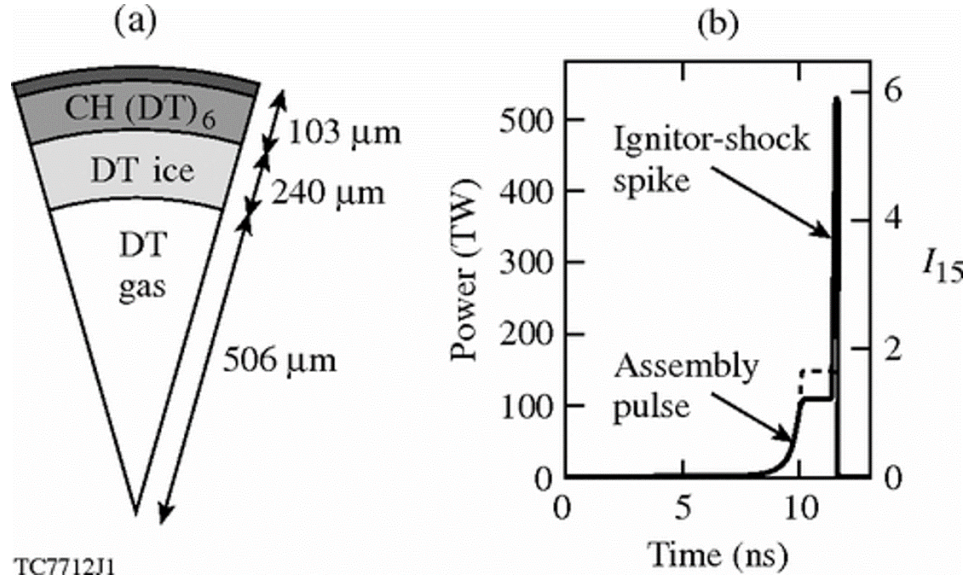


Figure 1.10: Shock ignition (SI) target and pulse shape to contrast with conventional target and pulse in Figure 1.8. (a) Target cross-section, CH foam “wetted” with DT ice, pure DT ice and a central DT gas region. The radius of the SI target is much less than that of the target in Figure 1.8. (b) As shown in Figure 1.8 the laser power against time but with a second axis indicating the approximate intensity of the laser in units of  $10^{15} \text{W/cm}^2$ . The solid line corresponds to SI with a gain of  $\times 55$  the input laser energy of  $\approx 300 \text{kJ}$  and the dashed line corresponds to a conventional laser pulse that does not ignite. Figure reproduced from Betti et al. [2007].

A shock ignition laser pulse and target are shown in Figure 1.10 which enters a higher intensity regime ( $10^{15} - 10^{16} \text{W/cm}^2$ ) that causes a large fraction of laser energy to be coupled into LPI. The increase in LPI increases backscattered light and increases hot electron generation (Seaton and Arber [2020]). The possible drawback of such high intensities will be explored in Chapter 4 and Chapter 6.

## 1.4 Summary of Odin’s Conservation Equations

Odin is a 2D radiation-magnetohydrodynamics code (Mihalas and Mihalas [2013]) with an Arbitrary Lagrangian-Eulerian (ALE) mesh refinement (Caramana et al. [1998b,a]; Benson [1992]). Odin simulates a single fluid with multiple species. There is a single electron species, but a simulation may have many ion species defined by the material. Quasi-neutrality within a cell fixes the colocation of the species as a single neutral fluid with  $n_e = Z^* n_i$  (where  $n_e$  is the number density of free electrons,  $n_i$  is the number density of ions and  $Z^*$  is the mean ion charge state over the different ion species). There are separate equations which govern the internal energy within the electrons and ions (similar to Equation 1.40). But the mass and momentum equations (Equations 1.37 and 1.38) for the cell are solved with the combined pressure  $P = P_i + P_e$  and density  $\rho = \rho_i + \rho_e$  of the electrons and ions (in this quasi-neutrality is invoked). This means that the electrons and ions flow together as a single fluid.

A complete description of radiation-magnetohydrodynamics and Arbitrary Lagrangian-Eulerian (ALE) mesh refinement is beyond the scope of this Thesis (see Goffrey [2014] and Bennett et al. [2021]). Below is a brief outline of the method used to derive the mass and momentum equations used by Odin’s hydrodynamic solver. The form of the energy equation is not enlightening for energy transport as Odin is operator split, so the hydrodynamic step is solved with a compatible energy update (see Caramana et al. [1998b] or Goffrey [2014]), then energy is deposited by the (laser or hot electron) drivers and finally energy is diffused between cells (by conduction or radiation diffusion, using a form similar to Equation 1.27) all within one time step but in stages. Equation 1.40, presents a form of the energy equation that is true for Odin and shows the energy terms relevant for this Thesis in a single expression, although it is not one of Odin’s governing equations.

To evaluate the flow in a Lagrangian frame, it will be useful to define the convective derivative,

$$\frac{Df}{Dt} = \frac{\partial f}{\partial t} + u \cdot \nabla f \quad (1.30)$$

for a scalar variable  $f$ . Each of the Euler Equations 1.8 can be put in the Lagrangian

form (see Goffrey [2014]), here without derivation, the mass equation,

$$\frac{D\rho}{Dt} = -\rho \nabla \cdot \mathbf{u}, \quad (1.31)$$

the momentum equation,

$$\rho \frac{D\mathbf{u}}{Dt} = -\nabla P, \quad (1.32)$$

and the energy equation,

$$\rho \left( \frac{De}{Dt} + \frac{1}{2} \frac{Du^2}{Dt} \right) = -\nabla \cdot (\mathbf{u}P). \quad (1.33)$$

a more relevant form for Odin's energy equation can be achieved using the momentum equation to eliminate the kinetic energy,

$$\begin{aligned} \rho \frac{De}{Dt} + \rho \mathbf{u} \cdot \frac{D\mathbf{u}}{Dt} &= -\nabla \cdot (\mathbf{u}P) \\ \rho \frac{De}{Dt} - \mathbf{u} \cdot \nabla P &= -\mathbf{u} \cdot \nabla P - P \nabla \cdot \mathbf{u} \end{aligned} \quad (1.34)$$

which leaves the convective derivative of the internal energy,

$$\rho \frac{De}{Dt} = -P \nabla \cdot \mathbf{u}, \quad (1.35)$$

internal energy per unit mass is used within Odin's core solver.

For the momentum and mass equations, Reynolds transport theory (3D version of the Leibniz rule, see Marsden and Tromba [2003]) is required to attain the final form used in Odin. Reynolds transport theory,

$$\frac{D}{Dt} \int_{\Omega} f dV = \int_{\Omega} \left[ \frac{Df}{Dt} + f(\nabla \cdot \mathbf{v}) \right] dV \quad (1.36)$$

can be used to evaluate the flux into a cell volume  $\Omega(t)$  that changes with time. It is also useful to define the volume averaged  $\bar{f} = 1/V \int f dV$  and mass averaged  $\tilde{f} = 1/M \int f \rho dV$  quantities for each cell  $\Omega$  bounded by the surface ( $\mathbf{S}$ ). Using Equations 1.36 and 1.31, it is possible to rephrase the mass equation (Equation 1.31),

$$\frac{D}{Dt} \int_{\Omega} \rho dV = \frac{D}{Dt} \bar{\rho} V = \frac{D}{Dt} M = 0 \quad (1.37)$$

where the cell mass is defined by  $M = \bar{\rho} V$ . Using Equations 1.36, 1.32 and the

divergence theorem, the momentum equation (Equation 1.32) becomes,

$$\frac{D}{Dt} \int_{\Omega} \rho \mathbf{u} dV = M \frac{D\tilde{\mathbf{u}}}{Dt} = - \int_{\partial\Omega} P d\mathbf{S}. \quad (1.38)$$

where  $\partial\Omega(t)$  is the time dependant surface of the cell and  $d\mathbf{S}$  is normal to it. Equations 1.37 and 1.38 give the final form in which the mass and momentum equations are evaluated in Odin. The equivalent energy equation (Equation 1.35) is,

$$M \frac{D\tilde{e}}{Dt} = -\bar{P} \int_{\partial\Omega} \mathbf{u} \cdot d\mathbf{S} \quad (1.39)$$

although it is not used in Odin (the solver uses sub-zonal pressures defined within quadrants of the cell to solve conservatively, see Goffrey [2014] or Caramana et al. [1998b] for details) it is in a form which will allow us to state the various energy contributions and transport mechanisms. Equation 1.39, although not used by the solver is still approximately true for Odin.

The focus of Chapters 3 and 5 is energy transport, so it is useful to state an energy equation. Starting with Equation 1.39, energy transport within the electron species can be defined by,

$$M \frac{D\tilde{e}_e}{Dt} = -\bar{P}_e \int_{\partial\Omega} \mathbf{u} \cdot d\mathbf{S} - \int_{\partial\Omega} \mathbf{Q} \cdot d\mathbf{S} + \frac{dE_{equil}}{dt} + \frac{dE_{laser}}{dt} + \frac{dE_{hot}}{dt}, \quad (1.40)$$

where  $\tilde{e}_e$  and  $P_e$  are the mass averaged internal energy and volume averaged pressure for the electron species (fluid velocity  $\mathbf{u}$  is defined for all the mass within a cell); the energy flux,  $\mathbf{Q} = \kappa(T)\nabla T$ , is in brackets on the RHS of Equation 1.27 (used explicitly in Equation 2.13);  $E_{equil}$  is the energy passed between the ion and electron species (equilibration as seen in Spitzer [2006] and dependent on the ion-electron collision time in Equation 1.20),  $E_{laser}$  is the energy deposited by the laser (see Equations 1.25 and 3.31) and  $E_{hot}$  is the energy deposited by hot electrons (see Equation 5.11). In Equation 1.40, several terms have been neglected including, radiation diffusion, ohmic heating and viscous heating. The heat flux  $\mathbf{Q}$  is conservative and redistributes energy within the electron species down temperature gradients whereas,  $E_{equil}$ ,  $E_{laser}$  and  $E_{hot}$  are all source terms, putting energy into the fluid from an external source. For  $E_{equil}$  the external source is the ion species within the cell. An equation similar to Equation 1.40 can be defined for ions but without the laser and hot electron terms, since Odin models energy deposition from these sources as exclusively into the electron population. Then it is possible to solve Equation 1.38 for the cell using the combined ion and electron pressure.

The original work presented in Chapters 3 and 5 are code developments on the Odin project. The original work in Chapters 4, 6 and 7 are simulations and analysis using the code.

## Chapter 2

# Theory: Thermal Conduction

The first section (Section 2.1) will present derivation of the transport coefficients from the 1D plasma kinetic equation (where the magnetic field  $\mathbf{B} = 0$ ). Section 2.2, show the isotropic coefficients obtained in Spitzer Jr and Härm [1953] with a more sophisticated collision operator. Following this Section 2.2.1 is dedicated to extensions of isotropic conduction for a magnetized plasma or in the presence of steep temperature gradients. In Section 2.3, the modifications needed to compute ion conduction will be highlighted. Presented in this chapter is a literature review of previously published work, and no original work is provided. It is presented as context for original work in Chapter 3.

### 2.1 Simplified Derivation from Plasma Kinetic Equation

The aim of this section is to derive from kinetics the form and dependencies of Equation 1.27, by a simplified collision operator. The coefficients will be approximate, but the general form of the equation will be correct.

The plasma kinetic equation for electrons (without the subscript  $e$ ) can be approximated, in 1D space and  $\mathbf{B} = 0$  as,

$$\frac{\partial f}{\partial t} + v_x \frac{\partial f}{\partial x} - \frac{e}{m} E \frac{\partial f}{\partial v_x} = -\frac{f - f_M}{\tau_c}, \quad (2.1)$$

where the electron particle distribution ( $f$ ) only varies by a small amount from a Maxwellian ( $f_M$ ),  $E$  is the electric field, and  $\tau_c$  is the collision time-scale. The RHS is called the Krook operator and if collisions are negligible it is zero in which case the LHS is the Vlasov equation. Equation 2.1 is set up with an applied tempera-

ture gradient assuming enough time has passed to reach a state of equilibrium and pressure balance has occurred with a density gradient,

$$\frac{\partial n}{\partial x} = -\frac{n}{T} \frac{\partial T}{\partial x}, \quad (2.2)$$

which removes the time dependence of Equation 2.1, so we can set  $\frac{\partial f}{\partial t} = 0$  and rearrange to give,

$$f = f_M - \tau_c v_x \frac{\partial f_M}{\partial x} + \frac{\tau_c e}{m} E \frac{\partial f_M}{\partial v_x} \quad (2.3)$$

where the modification from a Maxwellian is given by the two terms on the right of the RHS. Thermal motion is random in direction so the contribution from all three spatial dimensions, including the two ignorable directions for this problem, are necessary therefore a 3D Maxwellian is used,

$$f_M(x, v) = n(x) \left( \frac{m}{2\pi k_B T(x)} \right)^{\frac{3}{2}} \exp \left( -\frac{mv^2}{2k_B T(x)} \right) \quad (2.4)$$

to find the change in the  $x$  direction we take,

$$\frac{\partial f_M}{\partial x} = \frac{\partial f_M}{\partial T} \frac{\partial T}{\partial x} + \frac{\partial f_M}{\partial n} \frac{\partial n}{\partial x} = \left( \frac{mv^2}{2k_B T^2} - \frac{5}{2T} \right) f_M \frac{\partial T}{\partial x} \quad (2.5)$$

and with respect to  $v_x$ ,

$$\frac{\partial f_M}{\partial v_x} = -\frac{mv_x}{k_B T} f_M. \quad (2.6)$$

Combining Equations 2.5 and 2.6 with Equation 2.3 we get,

$$f = f_M - \left( \frac{\tau_c m v^2 v_x}{2k_B T^2} - \frac{5\tau_c v_x}{2T} \right) f_M \frac{\partial T}{\partial x} + \frac{\tau_c e v_x}{k_B T} f_M E \quad (2.7)$$

which is the modified distribution function in the presence of a temperature gradient and/or electric field. The second term on the RHS shows that the particle distribution has some spatial dependence from the temperature gradient. To change from particle quantities to macroscopic properties, we define the current density,  $j_x \equiv -e \int v_x f dv$  and the heat flux,  $Q_x \equiv 0.5 \int m v^2 v_x f dv$ . The integral  $\int f_M v dv = 0$  since the velocity is randomly distributed around 0 but this is also true for  $\int f_M v^i dv$  where  $i$  is odd. Both  $j_x$  and  $Q_x$  are odd moments hence the first term of Equation 2.7 goes to zero hence, the current density and heat flux can be written,

$$j_x = \tau_c n e \left( \frac{\langle v^2 v_x^2 \rangle}{aT} - \frac{5\langle v_x^2 \rangle}{2T} \right) \frac{\partial T}{\partial x} - \frac{2\tau_c n e^2}{ma} \langle v_x^2 \rangle E \quad (2.8a)$$



$$Q_x = -\tau_c mn \left( \frac{\langle v^4 v_x^2 \rangle}{2aT} - \frac{5\langle v^2 v_x^2 \rangle}{4T} \right) \frac{\partial T}{\partial x} + \frac{\tau_c ne}{a} \langle v^2 v_x^2 \rangle E \quad (2.8b)$$

where  $a = 2k_B T/m$  and  $\langle v_k^i \rangle = 1/n \int v_k^i f_M dv_k$ , which are called velocity moments. The moments can be evaluated,

$$\langle v_k^2 \rangle = \int_{-\infty}^{\infty} \frac{1}{\pi a} v_x^2 \exp\left(-\frac{v_x^2}{a}\right) dv_x = a/2 \quad (2.9)$$

which results in  $\langle v_k^4 \rangle = 3a^2/4$  and  $\langle v_k^6 \rangle = 15a^3/8$ . Using the calculated moments, the current density becomes,

$$j_x = \delta \frac{\partial T}{\partial x} + \frac{1}{\nu} E, \quad (2.10a)$$

$$\delta = 0, \quad (2.10b)$$

$$\nu = \frac{m}{ne^2 \tau_c}, \quad (2.10c)$$

and the heat flux becomes,

$$Q_x = -\kappa \frac{\partial T}{\partial x} - \beta E, \quad (2.11a)$$

$$\kappa = \frac{5nk_b^2 T \tau_c}{2m}, \quad (2.11b)$$

$$\beta = \frac{5nk_b T e \tau_c}{2m}, \quad (2.11c)$$

where  $\delta = 0$  occurs due to the Krook collision model but with the full Vlasov Fockker-Plank (VFP) calculation it would be non-zero.  $\delta \neq 0$  would allow us to set  $j_x = 0$  and use Equation 2.10a rearranged for  $E$  to be substituted into Equation 2.11a to get  $Q_x \propto \partial T / \partial x$  only. The correct form and dependencies have been derived however the coefficients are approximate due to the simplified collision operator. The collision time  $\tau_c$  cannot be determined by the Krook model.

## 2.2 Isotropic

Spitzer Jr and Härm [1953] is accredited with first determining the isotropic electron thermal transport coefficients, and later improvement came from Braginskii

[1965]. Manheimer et al. [2008] more recently devised an analytic function to match the empirically tabulated dependencies of the transport coefficients on charge state ( $f(Z)$  below). Both of these will be used where Equation 1.27 will be restated below in terms of flux ( $Q_x$ ),

$$\rho c_v \frac{d(T)}{dt} = -\frac{d}{dx} Q_x \quad (2.12)$$

where the spatial axis  $x$  is aligned with the temperature gradient  $dT_e/dx$ ,  $n_e$  is the electron number density,  $c_v = (\partial e / \partial T)_v$  is the specific heat capacity (and  $e$  is the internal energy per unit mass) and the flux is defined as,

$$Q_x = \kappa(T) \frac{d}{dx} T \quad (2.13a)$$

$$\kappa(T) = f(Z) \frac{nk_B^2 T \tau_c}{m} \quad (2.13b)$$

$$\tau_c = \frac{12\epsilon_0^2}{ne^4 \ln \Lambda} \sqrt{\frac{m_e (\pi k_B T)^3}{2}} \quad (2.13c)$$

$$f(Z) = 13.6 \frac{Z + 0.24}{Z + 4.24}. \quad (2.13d)$$

where  $\ln \Lambda$  is the Coulomb logarithm and  $f(Z)$  is an ion charge state dependant term (Epperlein and Haines [1986]). The term  $f(Z) \approx 13.6$  is constant for large  $Z$ , heavy nuclei, but as  $Z \rightarrow 1$  it varies to account for the increasing role that electron-electron scattering plays on angular deflection (Epperlein and Haines [1986]). All of this is for an unmagnetized plasma.

### 2.2.1 Beyond Spitzer-Härm

For a magnetized plasma, the heat flux has two more terms, one perpendicular to the temperature gradient and one perpendicular to the magnetic field Braginskii [1965].

To define a steep temperature gradient, we first must define the electron mean free path,  $\lambda_{mfp} \equiv v \tau_c$  (where  $\tau_c$  is the collision time with any species) and temperature length scale is defined by  $L = T / \frac{dT}{dx}$ . In steep temperature gradients (where  $0.01 > \frac{\lambda_{mfp}}{L}$ ) the thermal conduction described by Spitzer Jr and Härm [1953] no longer agrees with experiment or kinetic theory. The first fix was to set a

maximum flux defined by the free streaming limit,

$$Q_* = n_e v_{rms} E_{th} = \frac{n_e (3k_B T_e)^{3/2}}{2\sqrt{m_e}} \quad (2.14)$$

where  $Q_*$  assumes all particles are in a Maxwellian distribution travelling down the temperature gradient at the RMS velocity ( $v_{rms} = \sqrt{3k_B T/m_e}$ ) depositing the mean thermal energy ( $E_{th} = 3/2 k_B T$ ) (Malone et al. [1975]). To match observations, the flux limit is often set as some fraction of the free-streaming limit  $f_{fl} Q_*$ . The factor  $f_{fl}$  is a free parameter that is problem dependant. An example of this problem dependency can be seen as it is common for simulations of direct driven targets to use  $f_{fl} \approx 0.05$  (Malone et al. [1975]) and indirect drive (x-ray driven targets) to use a “high flux” model with  $f_{fl} \approx 0.15$  (Rosen et al. [2011]).

Even for an electron population that remains nearly Maxwellian the high energy tail of the distribution can lead to non-local transport (Bell et al. [1981]). The best solution to this issue was to add a non-local flux to fluid simulations (Schurtz et al. [2000]).

### 2.3 Conduction by Ions

Ion thermal conduction can play a role, especially in the hotspot where the ion temperature can exceed the electron temperature. However, electrons quickly equilibrate to the ion temperature and due to their lower mass they provide more rapid energy transport. Ion conduction can be applied by modifying Equation 2.13,

$$Q_i = \kappa_i(T_i) \frac{d}{dx} T_i \quad (2.15a)$$

$$\kappa_i(T_i) = \left[ 3.906 \sqrt{\frac{2m_e}{m_i}} f_i(Z) \right] \frac{nk_B^2 T_i \tau_c}{m_e} \quad (2.15b)$$

$$\tau_c = \frac{12\epsilon_0^2}{ne^4 \Lambda} \sqrt{\frac{m_e (\pi k_B T_i)^3}{2}} \quad (2.15c)$$

$$f_i(Z) = \frac{1}{Z^4} \quad (2.15d)$$

where  $T_i$  is ion temperature and all other modifications have been enclosed in square brackets.

## Chapter 3

# Application and Tests: Thermal Conduction

Thermal conduction in extreme environments presents considerable challenges for any numerical method and the wide range of possible uses for Odin limits the choice of method. The thermal conduction module took approximately 18 months of work to develop and test, furthermore the additional features Odin required to simulate ICF (such as the ray model and the quiet start feature in Section 3.8) took at least 6 months to implement and test. Developing core code for an ALE code is difficult, and the extreme environments make tolerances very small. Details about the challenges and requirements will be covered in Section 3.1. Having detailed the design brief, the possible implementations of thermal conduction will be listed, all aiming to achieve the same well-defined result. However, the finite difference methods vary considerably, and the selection criteria are in the next section, 3.2. The chosen method will be outlined and its modification from the original source (Sheng and Yuan [2008]) discussed in Section 3.3. Alongside the method developed for this Thesis, a method written by Tony Arber based on Pert [1981] and the issues it faces in extreme conditions, will be covered in Section 3.4. Having laid out the spatial differencing, the choice of an implicit time stepping routine and the matrix inversion are in Section 3.5. Section (3.6) will contain a list of desired future work on this project. The choice of regression tests and other applied tests used to check the thermal conduction module will be covered in Section 3.7. Lastly, in Section 3.8 additional features such as radial ray tracing and Odin's quiet start will be covered which made possible the simulation of full ICF implosions. Implosions comprise the final test of the conduction model which will also be required for simulation of experiments in Chapters 6 and 7. The conduction model presented

below follows closely work by Sheng and Yuan [2008] however the implementation and modifications were completed by the author as original work for this Thesis in addition to the matrix inversion, quiet start and ray tracing models.

### 3.1 Design Brief

The fluid approximation states that a volume contains enough particles that it no longer acts as a series of discrete points and can be treated as a continuous material, with continuous properties, viewed on a macroscopic scale. In this chapter we will assume the fluid approximation holds (shocks and non-local transport are possible exceptions) but even within fluids there are significant challenges for the chosen numerical method. Odin is designed to simulate the most extreme environments created on the planet. Temperatures high enough to not just melt but ionize any material ( $> 10^7\text{K}$ ); Densities and pressures that squeeze matter to degeneracy ( $> 100\text{Gbar}$ ); and material flows that are greater than 1% the speed of light.

Firstly, the extreme conditions. The chosen method needs to produce stable (non-fluctuating, non-negative) diffusion in all conditions, this is a significant barrier when the temperature difference for experiments can vary from cryogenic ( $< 20\text{K}$ ) to hotter than the core of the sun ( $> 1\text{keV} \approx 10^6\text{K}$ ) over a distance of microns. Alone the temperature gradient is a challenge but with the additional requirement that thermal conduction must not dictate the time step and must not be the slowest step we have a significant hurdle that points to a clear solution as seen in the section on explicit vs implicit methods (Section 3.5). The method will be first order in time. A major benefit of selecting a first order in time method is the diffusive nature of the error. For a model designed to achieve diffusion, diffusive error is an asset.

A phenomenon critical for ICF is shock propagation. As discussed in the introduction, compression to the required densities relies on spherical convergence of the shell and shock compression. Shocks occur in all fluids on a macroscopic scale but is a microscopic process, often just hundreds of atoms in width. Fluid codes must apply careful corrections to make sure they are non-diffusive to the narrow shock front (Caramana et al. [1998b]) but what is critical for thermal conduction is that these shocks are discontinuities in density, pressure, fluid velocity and temperature meaning that any calculation of diffusion must be robust to these. Another common, discontinuity that must also be modelled consistently is contact discontinuities i.e. material boundaries.

Additional challenge is presented by the grid used to capture the flow. There are two “standard” ways of simulating fluids, Eulerian and Lagrangian. Eulerian

enforces an unmoving grid on the domain being simulated and allows material to pass through it. Eulerian codes must track material boundaries beyond the cell resolution otherwise they will cause numerical mixing of materials.

The other method is called Lagrangian. Simply put, the mesh follows the fluid. Lagrangian is the method of choice for 1D HEDP simulations as numerical mix is not an issue however, when extended to two spatial dimensions a new problem arises. The issue is called “grid tangling”; it occurs in Lagrangian simulations where cells overlap, often due to a fluid instability (mixing on many scales that worsens as it grows) but does not occur in Eulerian simulations with a stationary grid.

The advantages of both these methods can be harnessed with an Arbitrary Lagrangian-Eulerian mesh refinement scheme (ALE). With ALE mesh refinement, as the grid tangles, the user can specify a remapping of the grid onto the material or hold the grid stationary and allow the material to flow through. An example of when this might occur, if a simulation started with a Lagrangian mesh becomes Rayleigh-Taylor (RT) unstable and the grid can no longer follow the non-linear growth, it is then switched to an Eulerian grid for the fluids to mix and then switched back to Lagrangian for the conservative properties it bestows. The remap need not be spatially uniform, but can be focused on the area that featured the RT growth. The drawback of ALE methods is that a Lagrangian mesh can have mixed material cells (and an Eulerian mesh can be non-uniform). This is important for thermal conduction, as the most extreme environments must be simulated without a regular grid and with mixed material cells. The chosen thermal conduction method must be robust to all these complications.

Finally, the diffusion routine will be implemented in a research code that will be drastically modified by multiple developers and users. We know from the outset that the model will later be augmented with both non-local transport and anisotropic thermal conduction, furthermore, at time of writing, the solver has been used for multi-group radiation diffusion. Simplicity and clarity will be a great asset in such a changeable, team based environment.

In summary, the greatest challenges for the chosen method are: extreme environments, discontinuities, computational efficiency, non-uniform grids and material boundaries.

## 3.2 Finite Difference Method Selection

In the preceding section, the difficulties presented by the simulation grid and by the environments simulated were covered; in this section the numerical schemes designed

to cope with the challenges will be discussed and although there is no single clear “best” method a reasoned choice will be described.

A concise and clear way of comparing diffusion finite difference methods was described by Morel et al. [1998]. In the paper, four desirable characteristics were given:

1. Spatially second order accurate on all grids
2. Only cell-centred unknowns
3. Local stencil
4. Symmetric positive-definite inversion matrix

and a list of which methods exhibit which behaviour. Of all the methods evaluated in Morel et al. [1998] and in this Thesis, none exhibit all four characteristics. The mutually exclusive nature has not been proven but without the possibility of achieving all four, the reasoning for the three selected will be outlined.

Considering the key characteristics and the project brief, by process of elimination, the choice of the three key characteristics will be explained. Firstly, second order accuracy on all grids is not required, but convergence on all grids is. All the desirable schemes explored in this literature review that do not achieve second order accuracy also do not converge for random or discontinuous grids, Pert [1977]; Kershaw [1981]; Breil and Maire [2007]. For convergence some require additional limiters that are an issue for simplicity and clarity but in practice, are also an issue for robustness in extreme environments, see tests in Section 3.7. The second point, only cell-centred unknowns; to use edge or vertex centred unknowns would require a bottom up rewrite of the entire code, since Odin operates off cell centred state variables. The work required and the payoff prohibits this choice. The third point, gives the option to work without a local stencil. There are several key fundamental issues with a non-local stencil: the code requires parallelisation for computational speed which is much more challenging with a non-local stencil; the simplicity and clarity of the code is lost and later augmentations will be far more difficult; finally a non-local method is computationally more expensive.

The only one of the four properties that can be sacrificed is point 4. A symmetric positive definite inversion matrix provides a known symmetry that can be used to accelerate convergence and allows improved preconditioning. Although not having a symmetric positive definite matrix is a substantial loss our selection fits the priorities laid out in the design brief.

			Ideal Properties			
Paper	Citations	Family	1	2	3	4
Kershaw [1981]	177	ECCFDM		X	X	X
Pert [1981]	34	ECCFDM			X	X
Shashkov et al. [1996]	230	SOM	X	X		
Morel et al. [1998]	131	SOM	X		X	X
Aavatsmark [2002]	553	MPFA	X	X	X	
Breil and Maire [2007]	134	MPFA		X	X	X
Sheng and Yuan [2008]	64	MPFA	X	X	X	
Basko et al. [2009]	39	ECCFDM		X	X	X

Table 3.1: A brief literature review of which finite difference methods exhibit which ideal properties. Citations recorded at time of writing. X means that the method has the property.

Table 3.1 shows the desirable properties for several of the most prominent finite difference methods for thermal diffusion. The methods fit into several main families: support operators methods (SOM), enhanced cell-centered finite difference methods (ECCFDM), and multi-point flux-approximation (MPFA), see Klausen and Russell [2004] where the relationship between these families are discussed.

From Table 3.1 both Aavatsmark [2002]; Sheng and Yuan [2008] have all the key characteristics except for a symmetric positive definite inversion matrix. Aavatsmark [2002] is a theoretical paper that acts as an introduction to the family of MPFA methods with their strengths and weaknesses; it is a great resource for further references. Sheng and Yuan [2008] is a specific example of MPFA that has been tested and is laid out clearly and concisely for a programmer.

MPFA has several additional features that make it a desirable scheme. As standard, the method consists of a 9 point stencil where energy flux is passed from the centre cell in Figure 3.1 to all 8 neighbours, however, it reduces to a 5 point stencil on a rectangular grid. The resulting 5 point stencil is one that has been extensively tested and is widely accepted as the best method for a rectangular grid (Morel et al. [1998]). The chosen method Sheng and Yuan [2008] has a clear and simple geometric explanation, from this point we can show that all corner fluxes will cancel.

Monotonicity has not been proven for many of the methods discussed, as show in Sheng and Yuan [2012], including for the selected method Sheng and Yuan [2008]. For the non-local mimetic methods, Shashkov et al. [1996] and Morel et al. [1998], it was demonstrated by Lipnikov et al. [2011]. For linear, control volume, nine-point methods it is impossible to have monotonicity, local conservation and



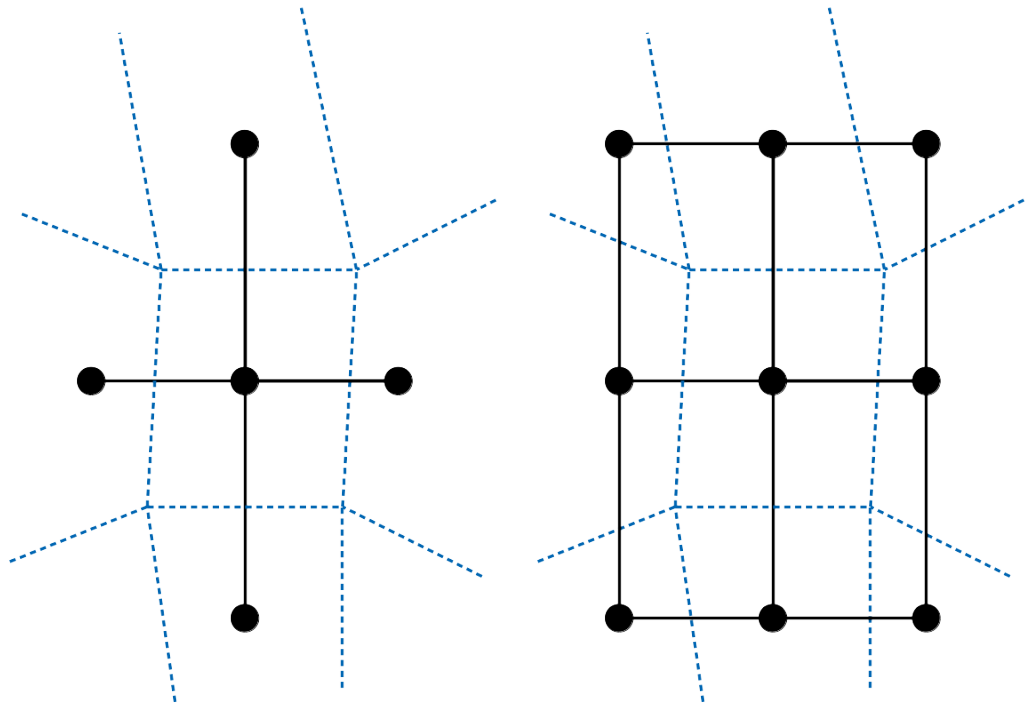


Figure 3.1: Schematic detailing 5 and 9 point stencil. Blue dashed lines represent cell boundaries, black dots are the cell centred values and the solid lines represent inter-cell flux.

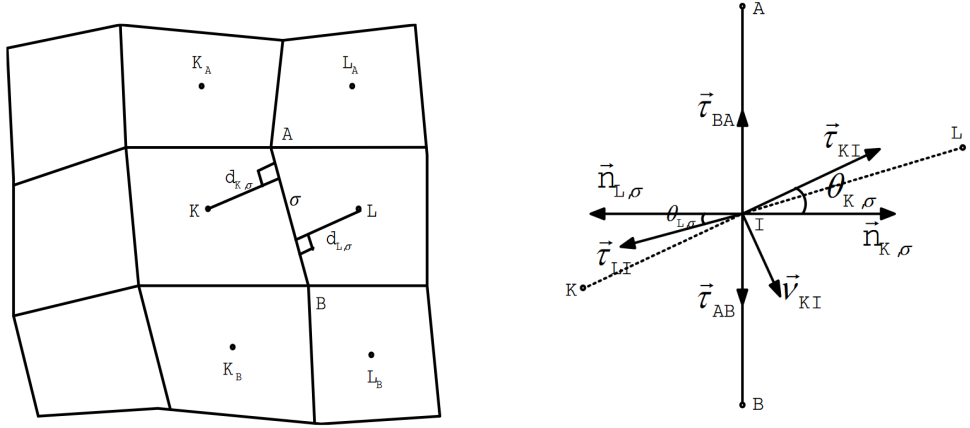


Figure 3.2: Diffusion notation. Left: image showing the grid with cell centres  $K, K_A, K_B, L, L_A$  and  $L_B$ , vertices  $A$  and  $B$ , and the edge  $\sigma$ . Right: Centred and reoriented is the line joining the vertices  $A$  and  $B$ . The key vectors for the flux calculation from  $K$  are the edge normal  $\vec{n}_{K,\sigma}$  and the non-orthogonal basis  $\vec{\tau}_{BA}$  and  $\vec{\tau}_{KI}$  (one parallel to the edge and the other parallel to an extension of a line joining cell centre to edge centre) with cell  $L$  also having a face normal  $\vec{n}_{L,\sigma}$  and non-orthogonal basis  $\vec{\tau}_{LI}$  and  $\vec{\tau}_{AB}$ . Reproduced from Sheng and Yuan [2008].

exact reproduction of linear solutions (Nordbotten et al. [2007]). It is possible that time steps causing large temperature changes (large time steps) will also cause nonphysical oscillations, breaking monotonicity. Thermal conduction is a non-linear parabolic differential equation, meaning that large times steps must be avoided to ensure accurate conduction.

### 3.3 Sheng et al 2008: Applied Method

The method in full can be seen in Sheng and Yuan [2008], a summary (using the same notation) and the modifications will be presented. Modifications were aimed to make it more effective for HEDP in an ALE code. Starting from the static diffusion problem,

$$-\nabla \cdot (\kappa(x)\nabla u) = f(x), \quad (3.1)$$

where  $\kappa(x)$  is the diffusion coefficient (thermal conduction coefficient),  $u$  is the diffused variable (temperature) and  $\kappa(x)\nabla u$  is the (energy) flux. We can subdivide the plane into cells ( $K, K_A, K_B, L, L_A$  and  $L_B$ ), vertices ( $A$  and  $B$ ) and an edge ( $\sigma$ ), laid out as in Figure 3.2. Using Green's formula, we can find the integral of  $f(x)$

over the region of the cell  $K$  and create a flux problem for the edge  $\sigma$ ,

$$\mathcal{F}_{K,\sigma} = - \int_{\sigma} \kappa(x) \nabla u(x) \cdot \vec{n}_{K,\sigma} dl, \quad (3.2)$$

where the direction of the unit normal  $\vec{n}_{K,\sigma}$  to the edge  $\sigma$  can be seen in Figure 3.2 and  $dl$  is the length of the edge. Sheng and Yuan [2008] proceeds with the geometric argument that the face normal  $\vec{n}_{K,\sigma}$  can be split into a non-orthogonal set,

$$\vec{n}_{K,\sigma} = \frac{1}{\cos \theta_{K,\sigma}} \vec{\tau}_{KI} - \tan \theta_{K,\sigma} \vec{\tau}_{BA}, \quad (3.3)$$

where the set is made from a term parallel to a line joining cell centre and edge centre  $\vec{\tau}_{KI}$ , and a term parallel to the edge  $\vec{\tau}_{BA}$  (on a rectangular grid  $\vec{\tau}_{KI} = \vec{n}_{K,\sigma}$  and  $\tan \theta = 0$  hence recovering a 5 point stencil). This step and the finite difference method is only valid for convex quadrilaterals. Taking a finite difference, first order Taylor expansion approximation of  $\nabla u(x)$  in the direction of  $\vec{\tau}_{KI}$ ,

$$\nabla u(x) \cdot \vec{\tau}_{KI} = \frac{u(I) - u(K)}{|I - K|}, \quad (3.4a)$$

and  $\vec{\tau}_{BA}$ ,

$$\nabla u(x) \cdot \vec{\tau}_{BA} = \frac{u(A) - u(B)}{|A - B|}. \quad (3.4b)$$

Combining equations 3.3 and 3.4 into 3.2 we get,

$$F_{K,\sigma} = -\kappa(K)|A - B| \left( \frac{1}{\cos \theta_{K,\sigma}} \frac{u(I) - u(K)}{|I - K|} - \tan \theta_{K,\sigma} \frac{u(A) - u(B)}{|A - B|} \right). \quad (3.5)$$

We have made the additional assumption that  $\kappa(x)$  can be approximated by  $\kappa(K)$ . Equation 3.5 can be rewritten as,

$$F_{K,\sigma} = -\tau_{K,\sigma}(u(I) - u(K) - D_{K,\sigma}(u(A) - u(B))) \quad (3.6)$$

where  $\tau_{K,\sigma} = \frac{|A-B|\kappa(K)}{|I-K|\cos \theta_{K,\sigma}}$  and  $D_{K,\sigma} = \frac{|I-K|\sin \theta_{K,\sigma}}{|A-B|}$ . We can determine a similar condition for flux from cell  $L$  through the edge  $\sigma$ ,

$$F_{L,\sigma} = -\tau_{L,\sigma}(u(I) - u(L) - D_{L,\sigma}(u(B) - u(A))), \quad (3.7)$$

with similar definitions for  $\tau_{L,\sigma}$  and  $D_{L,\sigma}$ . Finally we can use the flux matching condition  $F_{K,\sigma} = -F_{L,\sigma}$  and get,

$$F_{K,\sigma} = -\tau_{\sigma}(u(L) - u(K) - D_{\sigma}(u(A) - u(B))), \quad (3.8a)$$

$$F_{L,\sigma} = -\tau_\sigma(u(K) - u(L) - D_\sigma(u(B) - u(A))), \quad (3.8b)$$

where,

$$\tau_\sigma = \frac{1}{2(\tau_{K,\sigma}^{-1} + \tau_{L,\sigma}^{-1})} \quad (3.9)$$

half the harmonic mean and,

$$D_\sigma = D_{L,\sigma} + D_{K,\sigma} = \frac{(A - B) \cdot (L - K)}{|A - B|^2} \quad (3.10)$$

twice the arithmetic mean (Sheng and Yuan [2008] features a minor typographical error which has been corrected here).

With an expression for the flux through the edge  $\sigma$ , the issue remains that Odin does not define temperatures at the vertices ( $u(A)$  and  $u(B)$ ). Sheng and Yuan [2008] give two methods for calculating the vertex temperatures, the first is a distance weighted average of the surrounding cell centres, the second is also a weighted average but aims to correctly evaluate temperature for a vertex on or near a discontinuity. The distance weighted average is applied to Odin, and the other method is left for future work.

Using the notation defined in Figure 3.2 the vertex values can be approximated from the surrounding cell centres and a weight,

$$u(A) \approx \omega_{A_{K_A}} u(K_A) + \omega_{A_K} u(K) + \omega_{A_L} u(L) + \omega_{A_{L_A}} u(L_A) \quad (3.11)$$

where the terms  $\omega$  are the weights which can be calculated from the distance of the cell centre to the vertex using,

$$\begin{cases} \omega_{A_{K_A}} + \omega_{A_K} + \omega_{A_L} + \omega_{A_{L_A}} = 1 \\ x_{K_A A} \omega_{A_{K_A}} + x_{K A} \omega_{A_K} + x_{L A} \omega_{A_L} + x_{L_A A} \omega_{A_{L_A}} = 0 \\ y_{K_A A} \omega_{A_{K_A}} + y_{K A} \omega_{A_K} + y_{L A} \omega_{A_L} + y_{L_A A} \omega_{A_{L_A}} = 0 \end{cases} \quad (3.12)$$

where the  $x$  and  $y$  correspond to orthogonal distances. This is a 3 by 4 matrix  $\overline{\mathbf{M}}$ , that can be solved via a conjugate gradient (CG) method with a single iteration Saad [2003]. The method involves finding the transpose  $\overline{\mathbf{M}}^T$  and creating a 3 by 3 matrix  $\overline{\mathbf{A}} = \overline{\mathbf{M}} \overline{\mathbf{M}}^T$ . The inverse  $\overline{\mathbf{A}}^{-1}$  is computed and multiplied by vector  $\underline{v}_0 = (1, 0, 0)$  (defined by the RHS in Equation 3.12) giving a 3 by 1 vector,  $\underline{v}_1 = \overline{\mathbf{A}}^{-1} \underline{v}_0$ . The 4 by 1 solution vector is obtained by,  $\overline{\mathbf{M}}^T \underline{v}_1 = \underline{\omega} = (\omega_{A_{K_A}}, \omega_{A_K}, \omega_{A_L}, \omega_{A_{L_A}})$ . The CG method minimizes the  $\mathbf{L}_2$  norm (described by Equation 3.29).

We can now write the final form of the Sheng and Yuan [2008] flux calculation,

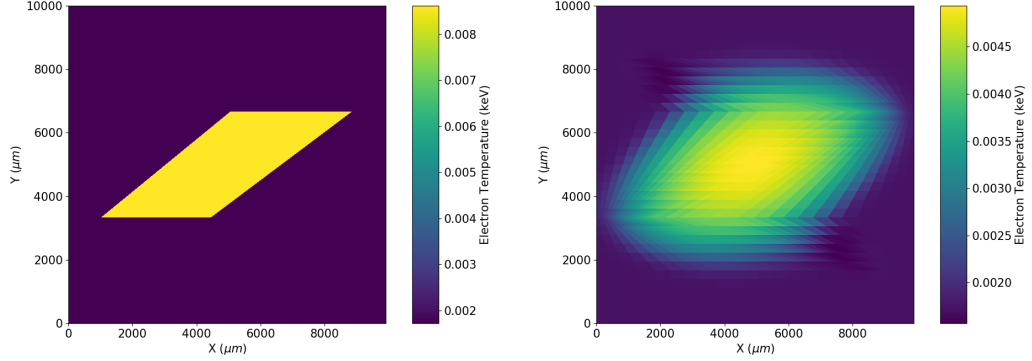


Figure 3.3: Energy conservation test (no hydrodynamics). Left: initial temperature state with a hot quadrilateral  $T_h = 10^5 \text{K}$  and a cold background  $T_c = 2 \times 10^4 \text{K}$ . Right: final diffused state. Images of explicit simulation. The final state breaks monotonicity with minima lower than  $T_c$  visible in the right image at top left and bottom right of the diffused heat. Both arithmetic averaging for implicit and explicit conduction were susceptible to violate the lower extremum depending on time step size. In the test arithmetic and harmonic averaging for implicit conduction achieved a relative energy conservation  $10^{-10}$  while explicit conduction achieved  $10^{-16}$ .

$$F_{K,\sigma} = -\tau_\sigma \left\{ u_L - u_K - D_\sigma \left[ \omega_{A_1} u_{K_A} + \omega_{A_2} u_K + \omega_{A_3} u_L + \omega_{A_4} u_{L_A} \right. \right. \\ \left. \left. - \left( \omega_{B_K} u_K + \omega_{B_{K_B}} u_{K_B} + \omega_{B_{L_B}} u_{L_B} + \omega_{B_L} u_L \right) \right] \right\}, \quad (3.13)$$

where the notation has been modified to indicate that all the temperatures ( $u$ ) are defined in the code and not calculated.

### 3.3.1 Modifications

A runtime option was added for a modification to the calculation of value  $\tau_\sigma$  (Equation 3.9). As stated in Basko et al. [2009] there are several possible benefits to using an arithmetic average instead of a harmonic average to calculate edge centred coefficients. The calculation,

$$\tau_\sigma = \frac{1}{4}(\tau_{K,\sigma} + \tau_{L,\sigma}), \quad (3.14)$$

was added to Odin. In tests, see Section 3.7, several benefits from the arithmetic version were observed, in addition full scale ICF implosions appear to be more stable to spacial asymmetries if an arithmetic average is used. In the limit of small,

$\delta = \tau_{K,\sigma} - \tau_{L,\sigma}$  the harmonic and arithmetic averages converge. However, the harmonic method is derived to be conservative while the arithmetic version has no derivation. When tested, both arithmetic and harmonic averaging give similar levels of energy conservation, as described by Figure 3.3.

Flux limiters were added to Odin. In Section 2 the concept of the free streaming limit  $Q_*$  for thermal energy was discussed (Equation 2.14). HEDP simulations commonly use flux limiters to regulate thermal conduction to a multiple of the free streaming limit (Colvin and Larsen [2013]). In Odin a runtime option was added such that the user can specify an asymptote for thermal flux, the definition Olson et al. [2000] is for a radiation flux limiter however with modification,

$$\kappa_{fl} = \left( \left( \frac{1}{\kappa} \right)^2 + \left( \frac{\nabla T}{Q_* f_{fl}} \right)^2 \right)^{-\frac{1}{2}}, \quad (3.15)$$

where  $\kappa_{fl}$  is the flux limited coefficient and the empirically determined limit  $f_{fl}$  is often found to be  $0.01 < f_{fl} < 0.1$ . This version is preferred as it gives a smooth transition from unlimited to limited conduction.

Other notable modifications are the correction for a non-Cartesian geometry (using cylindrical polar coordinates) which allows the 2D Odin to simulate spherical targets, implementation of boundary conditions and the corrections required to have multiple materials in a cell. Thermal conduction is a non-linear process ( $\kappa \propto T^{5/2}$ ), linearity was assumed in Sheng and Yuan [2008] and I will outline my solution in Section 3.5.2.

### 3.4 Pert 1981: Comparison Method

The method described in Pert [1981] was already applied to thermal conduction in Odin before this Thesis. The method was applied using an explicit time step with super-stepping as described in Section 3.5.1, this is in contrast to the implicit time step used for the Sheng and Yuan [2008] as described in Sections 3.3 and 3.5.2. The weaknesses and strengths of the Pert [1981] compared to the Sheng and Yuan [2008] will be examined. Pert [1981] is one of the earliest diffusion methods that attempts to work on a 2D Lagrangian grid, along with the seminal work by Kershaw [1981] significant improvement was not attained until more than a decade later with introduction of SOM by Shashkov et al. [1996] and then another half decade until the wide spread adoption of the MPFA family (Aavatsmark [2002]) of method described in Section 3.3. Even with the significant time and increase in computational performance that separates the two methods applied to Odin they

both offer different benefits and drawback but as will be demonstrated in Section 3.7 the benefits of Sheng and Yuan [2008] are better targeted toward the needs of ALE codes and extreme conditions.

The drawback of Sheng and Yuan [2008] is that it produces a non-symmetric inversion matrix which is computationally more expensive per step. There are three main fundamental issues with Pert [1981], it does not suggest a method for finding vertex unknowns, it requires monotonicity and extrumum limiters (see Pert [1981]), and it relies on assumptions of smooth mapping (see Sheng and Yuan [2008]). Each of these issues individually make Pert [1981] poorly suited for our design brief but together, when tested the method fails with simulations giving negative energies in some cells (including attempts to simulate ICF).

### 3.5 Time Stepping Options

In addition to the selection of a finite difference method discussed in the previous sections, a temporal solver is allocated to Sheng and Yuan [2008] method. The choice of solver is within a continuum, explicit methods at one end and implicit methods at the other, all points between are called semi-implicit methods. The environment and computational limitations determine which is the best choice. Without the limitation of computational expense the continuum of options all give the same answer. The problem arises when you have extreme conditions as described in Section 3.1 and limited compute (limited by the largest supercomputer, simulation time and the problems inherent ability to be parallelized).

Numerical stability increases along the continuum of solvers with implicit methods being unconditionally stable (regardless of input and time step size) and explicit methods requiring careful monitoring of environment to calculate a valid step size. Implicit routines are more difficult to code and generally more expensive per time step. The latter point means that improved computational accuracy can be achieved with more, faster explicit steps than the expensive implicit steps. However, in Odin the time step size is dictated by the fluid flow (advective time step limit),

$$\Delta t_{ad} \sim \frac{\Delta x}{|v|}, \quad (3.16)$$

though in many systems the thermal gradients (conductive time step limit),

$$\Delta t_{cond} \sim \frac{\Delta x^2}{\kappa}, \quad (3.17)$$

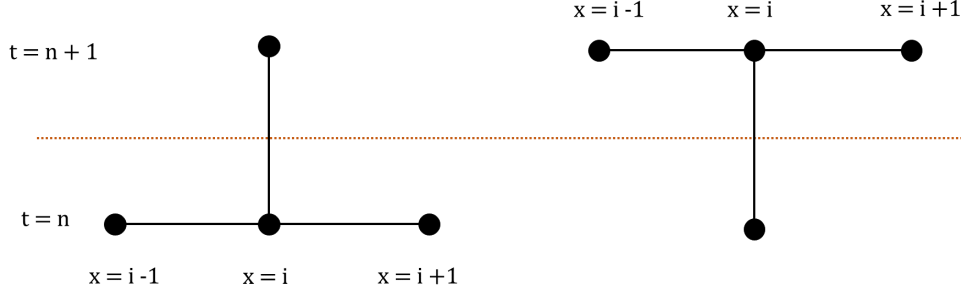


Figure 3.4: Left: Explicit stencil for 1D. 3 point spatial stencil and 1 output at  $t = n + 1$ . Right: Implicit stencil for a 1D code. Spatial 3 point stencil this time at  $t = n + 1$  which have to be solved as a series of simultaneous equations with the boundary condition and the 1 input point at  $t = n$  providing closure. Crossing the orange dotted line implies a change in time step. A semi-implicit method would use all 6 points from the two schematics (i.e. 3 spatial point stencil from  $t = n$  and 3 points from  $t = n + 1$ ). The weighting of the  $t = n$  vs  $t = n + 1$  is what determines how implicit a method is.

can be far more limiting to time step size meaning that to run a simple explicit solver for thermal conduction in an ICF problem the code's time step might need to be reduced by  $10^6$ . Such large reductions in time step render simulations untenable. There are many methods for improving the stability (time step limitations) and accuracy of an explicit solver of which super-stepping is one (which was applied to Pert [1977] method in Odin). Super-stepping will be briefly explored in 3.5.1 but to achieve a valid answer with the least possible compute for an arbitrary sized time step we must select an unconditionally stable method hence an implicit time step was applied.

Now the choice of time step solver has been justified, the explicit and super-stepping method will be summarized for the context of the tests and comparisons.

### 3.5.1 Explicit Super-stepping: Comparison Method

The super-stepping routine was not developed for this Thesis. The routine is based on the paper Meyer et al. [2012, 2014] and is part of an established family of numerical methods called Runge-Kutta methods (Kutta [1901]). Runge-Kutta methods probe the change over time (temporal gradient of a function) with a number of smaller steps (super-steps) in time, with more information about the gradient they can make a more accurate full sized time step. Super-stepping is designed to use



these smaller steps to drastically soften the stability condition, in addition to improving the accuracy. The super-steps do come at a computational cost, but critically the cost is designed to be less than a stable non super-stepping method.

The stability of super-stepping scales with the square of the number of super-steps Meyer et al. [2014]. For example if a time step of 1ps is required for stability than by using  $n = 50$  super-steps that time step can be increased to  $1\text{ps} \times 50^2 = 2.5\text{ns}$  with minimal loss in accuracy Meyer et al. [2014].

There are two reasons that led to the adoption of implicit over super-stepping. Firstly, the domain of stability, for non-linear parabolic equations it is not well characterized and is more limited than the linear stability. Currently, the time step size is calculated based off the stability of the linear problem and although it has been tested in Meyer et al. [2014] for a specific non-linear problem this provides a significant risk to robustness. Secondly, the increase in stability of super-stepping has only been proven up to  $n = 64$  (Meyer et al. [2014]). Using a larger value for  $n$  would risk robustness and a time step  $dt_{ss} = 64^2 dt \approx 5000dt$  is too limiting for the extreme conditions commonly found in Odin. In our tests (Figure 3.9), it was found that the implicit and super-stepping method would take a similar duration for a single time step ( $n = 64$ ) however neither method was optimized (see Meyer et al. [2014] for a more formal tests).

### 3.5.2 Implicit: Applied Method

Starting from the diffusion equation,

$$\frac{\partial u}{\partial t} = \nabla \mathcal{F}, \quad (3.18)$$

where  $\mathcal{F}$  is the energy flux. We can apply Green's formula over a cell and discretise to get,

$$\frac{\Delta u_K}{\Delta t} = \sum_{\sigma \in \mathcal{E}_K} F_{K,\sigma}, \quad (3.19)$$

where  $\mathcal{E}_K$  is all the edges of cell  $K$  and  $F$  is the flux through an edge described by Equation 3.13. Explicit methods are intuitive, the spatial stencil used in the current time step to calculate a flux for the next step and then the grid is updated. Using the diffusion equation the RHS is at time  $t = n$  and the left side is the difference between  $t = n$  and  $t = n + 1$  (dropping the the  $K$ ),

$$\frac{u_{n+1} - u_n}{\Delta t} = \sum_{\sigma \in \mathcal{E}} F_{\sigma,n} \quad (3.20a)$$

$$u_{n+1} = \left( \sum_{\sigma \in \mathcal{E}} F_{\sigma,n} \right) \Delta t + u_n \quad (3.20b)$$

this is an explicit discretisation of time. Implicit methods apply the spatial stencil to the future step (see Figure 3.4) and then require a matrix inversion to calculate the contributions for flux from the current step; using the method described below the flux is never explicitly calculated and the output is the “relaxed” temperature system after diffusion has taken place. The energy change must be calculated from the final temperatures. The fluxes are never calculated because the inverse of a sparse matrix is not necessarily sparse so rather than handling an object of size  $9 \times N_x \times N_y$  (which is true for the number of flux terms in a 9 point explicit diffusion step) the flux calculation could be of order  $(N_x \times N_y)^2$  which would be computationally expensive.

The diffusion equation for implicit methods,

$$\frac{u_{n+1} - u_n}{\Delta t} = \sum_{\sigma \in \mathcal{E}} F_{\sigma,n+1}, \quad (3.21a)$$

$$u_n = u_{n+1} - \left( \sum_{\sigma \in \mathcal{E}} F_{\sigma,n+1} \right) \Delta t, \quad (3.21b)$$

which is a problem since the desired output is  $u_{n+1}$  in order to resolve this issue, a system of linear equations must be solved,

$$u_n = \overline{\mathbf{A}} u_{n+1}, \quad (3.22)$$

where  $\overline{\mathbf{A}}$  is a 9 diagonal banded matrix, size  $(N_x N_y)^2$ , where each non-zero element is equivalent to a term in Equation 3.13. A matrix inversion will give the desired output,  $u_{n+1}$  in terms of our input  $u_n$ ,

$$u_{n+1} = \overline{\mathbf{A}}^{-1} u_n. \quad (3.23)$$

A full term on the lead diagonal is given to illustrate how Equation 3.13 is formed into linear equations (there are 4 edges involved:  $\sigma 1, \sigma 2, \sigma 3$  and  $\sigma 4$ ; 4 vertices:

$A, B, C$  and  $D$ ; and the cell  $(1, 1)$  corresponds to the cell labelled  $K$  in Figure 3.2),

$$\begin{aligned}\bar{\mathbf{A}}_{11} = & 1 - (\tau_{\sigma 1}(1 + (D_{\sigma 1}(\omega_{A_K} - \omega_{B_K}))) \\ & \tau_{\sigma 2}(1 - (D_{\sigma 2}(\omega_{C_K} - \omega_{B_K}))) \\ & \tau_{\sigma 3}(1 - (D_{\sigma 3}(\omega_{D_K} - \omega_{C_K}))) \\ & \tau_{\sigma 4}(1 + (D_{\sigma 4}(\omega_{D_K} - \omega_{A_K}))))\Delta t\end{aligned}\tag{3.24}$$

this is one term, each cell has nine terms. Overall, these terms create a nine diagonal banded matrix which must be inverted and applied, as in Equation 3.23.

For ideal linear conduction the diffusion coefficient  $\kappa$  (see Equation 3.1) is independent of the temperature, however plasma theory gives  $\kappa \propto T^{5/2}$  (Spitzer Jr and Härm [1953]). An explicit method time-step could evaluate  $\kappa(T)$  at time step  $t = n$  but for an implicit method  $\kappa(T)$  must be evaluated at  $t = n+1$  (see Equation 3.23), the most accurate way to resolve this problem is to use an iterative solver which improves the guess for  $\kappa(T_{n+1})$  and  $T_{n+1}$  on each iteration (Basko et al. [2009]). This can be considered a case for future work, in this Thesis the approximation  $\kappa(T_{n+1}) = \kappa(T_n)$  is made, which will be valid in the majority of cases since the time step should limit  $\Delta T$  but the larger the time step (given a fixed temperature gradient) the less accurate the approximation and the more non-linear conduction should be.

## Matrix Inversion

The inversion of a large sparse matrix can be achieved directly, however the computational expense led Sheng and Yuan [2008] to choose an iterative method that can be parallelized. This Thesis follows the method outlined in Sheng and Yuan [2008] using Bi-CG-STAB inversion Van der Vorst [1992] and a HyPre BoomerAMG preconditioner Falgout and Yang [2002]. The method was applied using the PETSc matrix inversion library Balay et al. [2018].

Once the thermal conduction module for Odin was complete, some high frequency noise was observed in large parallel simulations. It is a known issue that for non-symmetric matrices, AMG preconditioners can fail to remove high frequency noise Wathen [2015]. It is the nature of a large multi-physics hydrodynamic simulation that makes identifying the source of numerical noise non-trivial. It is possible that small fluctuations are not being diffused effectively with the current choice of solver and preconditioner and that with a different combination and optimization the issue could be reduced for some problems or even removed. In the next section, an alternative solution will be highlighted that provides diffusion robust to grid scale

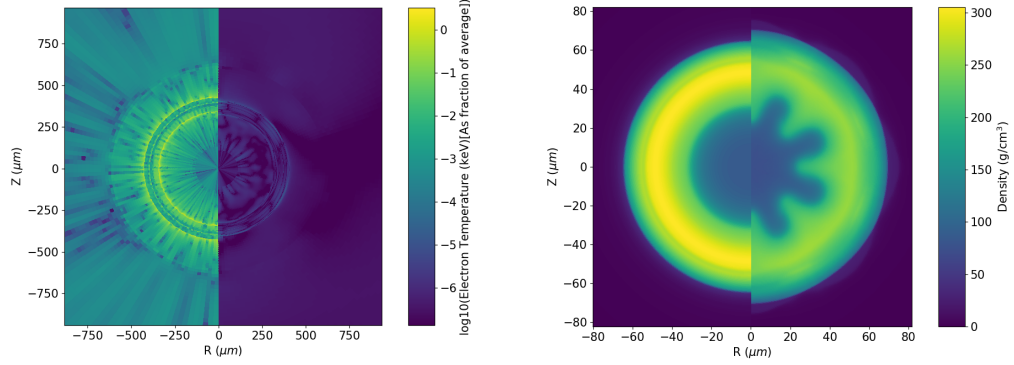


Figure 3.5: Left: Numerical asymmetries present in a late stage capsule implosion without filtering (left half) and with a median filter (right half) the noise is reduced several orders of magnitude. The image includes the coronal region, which is very susceptible to tangling due to the high velocity flows and low densities. Right: Two simulations using the median filter focusing on the high density capsule during peak compression, a uniform implosion (left half) compared to a simulation that was driven asymmetrically with laser perturbations (right half). This demonstrates median filtering capabilities with non-uniform simulations.

noise.

### Addition: Median Filter

All tests done in this section and the majority of the simulations run for this Thesis were without any filtering. The method presented above is robust to extreme temperature gradients, discontinuities and distorted grids, it fits the design brief and the requirements of HEDP on high performance (parallel) computers. It is noted however that large simulations run in parallel with significant target convergence can exhibit the growth of high frequency noise (specifically at the boundaries between parallel processed domains). The method devised in this section is presented to reinforce the robustness of large simulations in Odin. The filter is a non-physical addition that will reduce energy conservation but with the benefit of dampening non-physical disruptive grid scale noise.

A median filter was applied,

$$e_i = \text{sum}(e_{i-1}, e_i, e_{i+1}) - \min(e_{i-1}, e_i, e_{i+1}) - \max(e_{i-1}, e_i, e_{i+1}) \quad (3.25)$$

where  $e_i$  is the energy density in cell  $i$ . This is in 1D that can then be applied again in more directions or on other parameters featuring grid noise. The median filter is

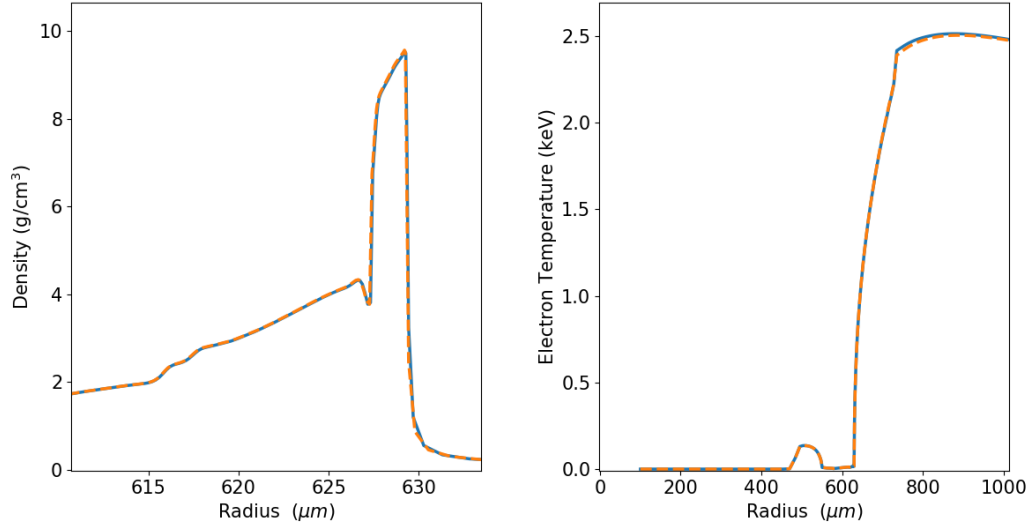


Figure 3.6: The figures show for simulation of a target implosion the differences between an unfiltered (solid blue line) and a filtered (dashed orange line) simulation. Left: shell density, slight differences are visible at the ablation front (630 microns). Right: electron temperature throughout the target and ablation plasma, there is a difference in temperature in the coronal plasma (800microns).

a destructive process since information is irretrievably removed from the system. It is a process that does not conserve energy by definition, however the median filter is designed to only remove noise on the grid scale and preserve larger features such as well resolved, lower mode non-uniformities. These features are both demonstrated in Figure 3.5. The energy conservation of a system can be measured by taking the initial system as a zero point and accounting for all inputs and outputs. Odin's energy conservation for a full physics implosion is approximately  $\approx 1\%$  ( $\approx 1.5\text{kJ}$  for  $150\text{kJ}$  of input laser energy at the snapshot pictured in Figure 3.5 left). When the same simulation is run with median filtering the additional variation is of order  $\approx 0.01\%$  ( $\approx 15\text{J}$  for  $150\text{kJ}$  input, this minor loss of energy is also observed in simulations which have been intentionally driven asymmetric such as Figure 3.5 right). Figure 3.6 depicts the small variations in density and temperature that might be observed when running a simulation with or without a median filter. These variations have been acceptable for the non-predictive simulations, however the thermal conduction module is fully functional without a median filter but the preconditioner and solver will require optimisation when run on large parallel systems.

### 3.6 Future Work

Several significant additions have been made to the selected numerical methods, including a median filter and the arithmetic face centred unknowns. Some additions were discussed as future work such as improved weighting for discontinuous vertex unknown and an iterative solve for non-linear conduction coefficient  $\kappa(T)$ , further work is outlined below.

For large temperature gradients in HEDP particle kinetics becomes important for energy transport. Kinetic physics cannot be modelled on a macroscopic scale with a fluid code however there is a well established improvement to Spitzer Jr and Härm [1953] known as the SNB model, (Schurtz et al. [2000]; Sherlock et al. [2017]) this model can be added to the current implementation of thermal conduction as a piece of further work. The correction becomes important as particle mean free path approaches 1% of the temperature scale length.

Another improvement would be the addition of a Braginskii [1965] transport model which accounts for magnetic fields. When applied Braginskii [1965] transport creates a component of energy transport perpendicular to the temperature gradient and suppresses some of the component parallel.

### 3.7 Tests

The two diffusion solvers described above were implemented, Sheng and Yuan [2008] implicit method (referred to here onward as the implicit method) and Pert [1977] super-stepping method Meyer et al. [2012] (referred to as the explicit method) in Odin. The tests described aim to evaluate: correct implementation, accuracy, convergence and robustness of each diffusion model. There is a tradition in diffusion numerics of testing each model on the Z-grid (Kershaw [1981]), it was intentionally designed to be challenging with distorted cells as seen in Figure 3.7, this grid was used to demonstrate correct implementation, accuracy and limits of robustness in Section 3.7.1. Section 3.7.2 uses a uniform grid to show the convergence rate of the implicit method. In Section 3.7.3, the harmonic mean and arithmetic mean of edge centred coefficients were tested to show the accuracy and robustness of each. In the last section (3.8), the use of the implicit conduction model in full scale ICF simulations will be demonstrated, in addition to the ray tracing model and the quiet start features which were added to simulate implosions.

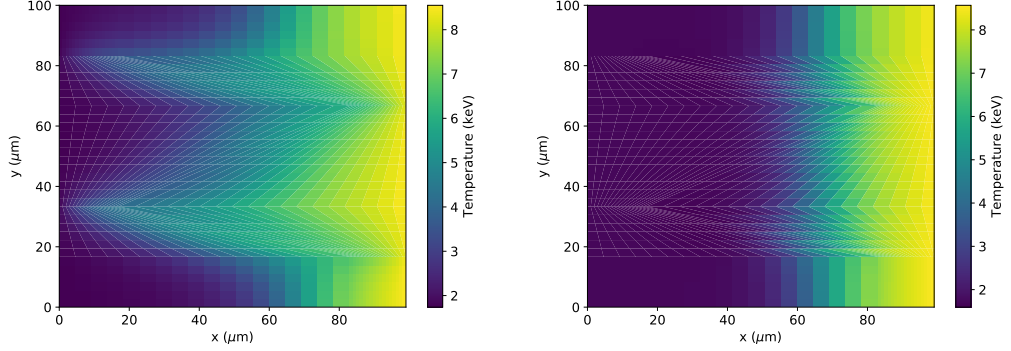


Figure 3.7: Left: Implicit conduction using a 5 point method. Right: Implicit conduction using Sheng and Yuan [2008] full 9 point method. Both images are a snapshot of a heatwave propagating from right to left. Simulation using the 5 point method leads to the grid affecting the diffusion front despite the uniform material properties and boundaries in the y-direction. The nine point method shows improved uniformity.

### 3.7.1 Kershaw’s Z grid

In Figure 3.7 the Z-grid is used to show the improvement of a nine-point stencil over a five point method (five point stencil in Figure 3.1 and Z-grid from Kershaw [1981]). The figure gives a qualitative idea of the difference between the five and nine point stencils. The five point scheme does not converge for non-uniform grids. The problem is designed to have no hydrodynamics (stationary) and an easily derived static analytic solution for long times. The warped grid structure is meant to replicate the complexities of diffusion for Lagrangian flow. The material is uniform, and so should be the heat-front and static solution. The right boundary is held at a high temperature ( $T_R = 10^8\text{K} \approx 8.6\text{ keV}$ ) and the left at a low temperature,  $T_L = 2 \times 10^7\text{K} \approx 1.7\text{ keV}$  with the starting temperature in the domain also  $T_L$ . A heat wave travels from hot to cold and then reaches an equilibrium state. Qualitative improvement is seen from the Sheng and Yuan [2008] method compared to the five point method.

Figure 3.8 shows a Z-grid comparison between simulation and an analytic model,

$$T(x) = (ax + b)^{\frac{2}{7}}, \quad (3.26a)$$

$$a = \frac{T_R^{\frac{7}{2}} - T_L^{\frac{7}{2}}}{x_R - x_L}, \quad (3.26b)$$

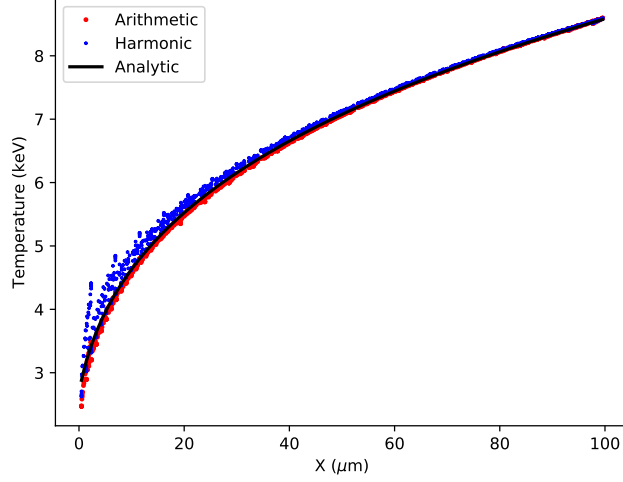


Figure 3.8: Implicit method comparison between harmonic averaging (blue dots) and arithmetic averaging (red dots) for edge centred coefficients compared to an analytic solution at infinite time (black line). The simulations are at an equilibrium state for the Z-grid diffusion problem. All cell centres (dots) should converge to the black line.

$$b = -x_L \frac{T_R^{\frac{7}{2}} - T_L^{\frac{7}{2}}}{x_R - x_L} + T_L^{\frac{7}{2}}, \quad (3.26c)$$

where  $x_L$  and  $x_R$  are the spatial positions of the left and right boundaries. The analytic solution (Equation 3.26) is derived from,

$$\rho \frac{d\epsilon}{dt} = \frac{d}{dx} (\kappa_0 T^{5/2} \frac{d}{dx} T) \quad (3.27)$$

where  $\kappa_0 T^{5/2} = \kappa(T)$ . If the LHS of the equation is set to zero (equilibrium hence no change in time) it can be integrated to get,

$$C_2 x = \frac{2}{7} \kappa_0 T^{7/2} + C_3 \quad (3.28)$$

using the temperatures and positions for the left and right boundaries the constants cancel to get Equation 3.26.

In Section 3.3.1 an arithmetic averaging modification to the harmonic method by Sheng and Yuan [2008] was described. Figure 3.8 shows that the harmonic average technique achieves lower accuracy when compared to the arithmetic average. Despite this, harmonic averaging is used for Odin’s regression test since it the



method described in Sheng and Yuan [2008]. The regression test can be run in  $\sim 1s$  and provides a clear analytic comparison. Explicit super-stepping (not shown) required 100 times longer ( $\approx 100s$ , both run in serial, not in parallel) to run the test problem but achieved a similar level of accuracy to arithmetic averaging (it required  $\approx 100$  times more steps with  $n = 64$  to remain stable). When run with this test problem, the super-stepping was susceptible to breaking if the number of super-steps exceeded 100 per explicit step.

The tests run in this section suggest that the implicit method based on Sheng and Yuan [2008] with an arithmetic average modification provides the best accuracy and robustness for minimal computational expense. But both methods are provided to the user as options.

### 3.7.2 Convergence

A second test was devised to check the convergence of the time step methods (also without hydrodynamics). A uniform grid was used to reduce each method to a 5 point stencil (eliminating the difference between Sheng and Yuan [2008] and Pert [1981] methods). The test case is a heat front moving into a cold medium, which enables the evaluation of the accuracy for dynamic problems (non-equilibrium). Rather than solving analytically, the highest resolution super-stepping simulation  $N_x = N_y = 256$ , was used as the “exact” solution and convergence with increasing resolution was tested for these  $N_x = 2, 4, 8, 16, 32, 64, 128$  seven resolutions. A 2D simulation was run to ensure each solver reduced to a 5 point method (preserving spatial symmetry). Figure 3.9 shows the results of the convergence test, and the gradients give the order of convergence. In the convergence test shown a non-linear conduction problem ( $\kappa \propto T^{\frac{5}{2}}$ ) was tested and the three most commonly used measures of error were calculated,  $\mathbf{L}_1$ ,  $\mathbf{L}_2$  and  $\mathbf{L}_\infty$  norms whose value can be found using:

$$|\mathbf{L}_p| \equiv \frac{1}{n} \left( \sum_i^n |T_i - T_{i,exact}|^p \right)^{1/p} \quad (3.29)$$

where  $p$  dictates which norm is calculated,  $T_{i,exact}$  is the exact solution for cell  $i$  and  $T_i$  is the solution for cell  $i$  determined by the model being tested. In the case of  $p = \infty$  the maximum error (difference to the exact value) on the grid is the Norm. For the gradients in Figure 3.9, the scaling was taken from the 3rd data point onward as it is where the gradient becomes most linear, but it is clear that no straight line will map perfectly onto the curve. Both the super-stepping and implicit show somewhere between first and second order convergence for this problem. The error

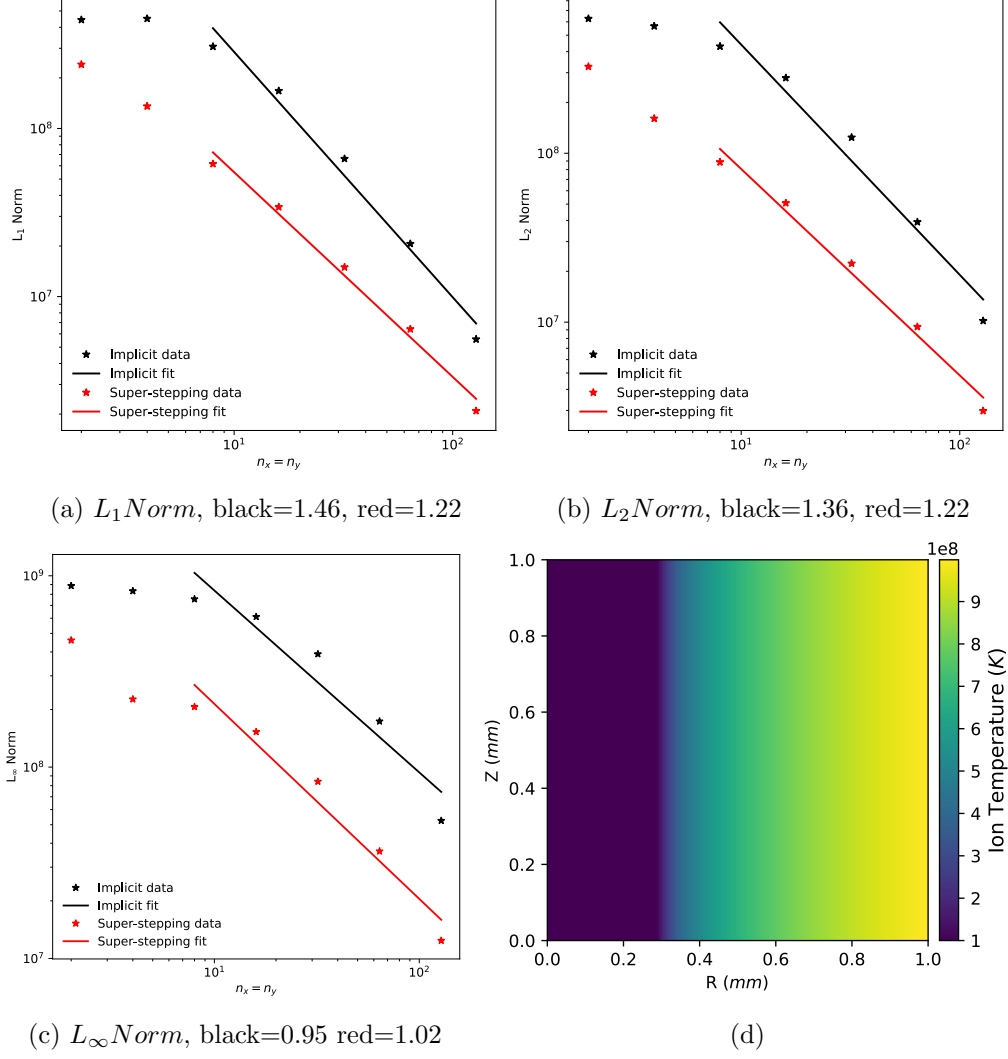


Figure 3.9: Convergence test for the implicit and explicit models. Gradients (Order of convergence) is given below each plot except (d) which shows the test problem at the point the test was taken, this is a snapshot of a heat wave travelling across the domain. The initial temperature of the domain is,  $T_c = 10^8 K$  and the right boundary is held at  $T_h = 10^9 K$ .

for super-stepping was on average lower, but the test was intentionally optimized to show the explicit method at its best, this can be explained by the choice of time-step size which was the same for both implicit and explicit methods but selected at the limit of stability for the explicit method with the number of super-steps at  $n = 64$  (the maximum proven stable for linear problems Meyer et al. [2014]) and that the “exact” solution was taken from the explicit method. The computation was done in serial (not parallel) and both method took approximately the same duration to compute a solution.

In Figure 3.9, that the explicit method can be used to achieve an error roughly half the size of the implicit method. It shows that both methods feature between first and second order convergence. The larger error of the implicit method is expected as it does not use super-steps to improve accuracy and although the difference in error is significant, this test was aimed to show the largest possible difference between the two methods. If the time step was increased further, the explicit method would no longer be stable, but the implicit method would only continue to reduce in accuracy. This test demonstrates an important distinction between the methods and demonstrates why only the implicit method fulfils the robustness criterium of the design brief in Section 3.1.

### 3.7.3 Heat-front into Cold Medium

In Section 3.3.1 the use of arithmetic averaging was examined, in Section 3.7.1 the benefit to accuracy for a static solution were examined, in this section the original impetus for an arithmetic average will be demonstrated. In Basko et al. [2009] the extreme example of a heat-front into a cold medium ( $T = 0$ ) is tested against an analytic solution. They find that an arithmetic method achieves near perfect agreement with the analytic model while a harmonic based solution features numeric artefacts. In Figure 3.10, harmonic method’s issues are reproduced for the Sheng and Yuan [2008] method. Basko et al. [2009] evaluates the location of the heat front for a non-linear problem analytically and then with a modified harmonic average (following the notation from Equation 3.9),

$$\tau_\sigma = \frac{1}{2} \left( \frac{1}{\tau_{K,\sigma}^{-1} + \tau_{L,\sigma}^{-1}} + \delta \cdot \max(\tau_{K,\sigma}, \tau_{L,\sigma}) \right) \quad (3.30)$$

and finds it converges to the analytic solution (arithmetic solution) as  $\delta \rightarrow 0.5$  (i.e the arithmetic method). Figure 3.10 shows a harmonic average will not allow conduction of heat into a cold medium and even with the modification will not properly replicate the heat front until it converges with the arithmetic average.

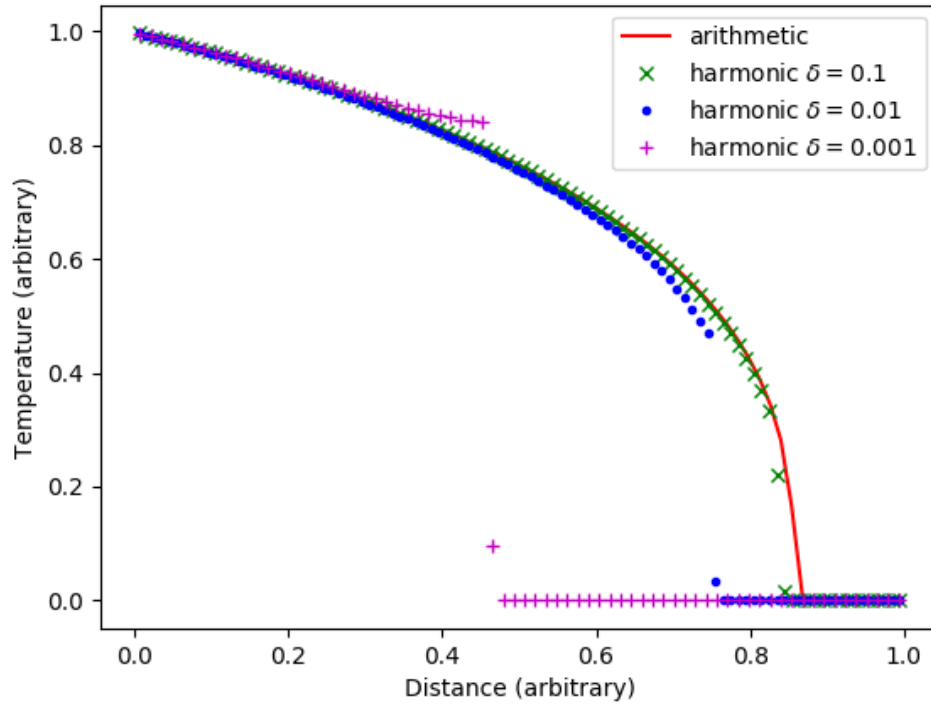


Figure 3.10: Simulation of a heat-front moving into a cold medium. Reproduction of a test shown in Basko et al. [2009] to highlight the benefit of an arithmetic average over the harmonic average derived from the flux matching condition. Using a harmonic average heat cannot flow into a cold medium  $T_c = 0$ .

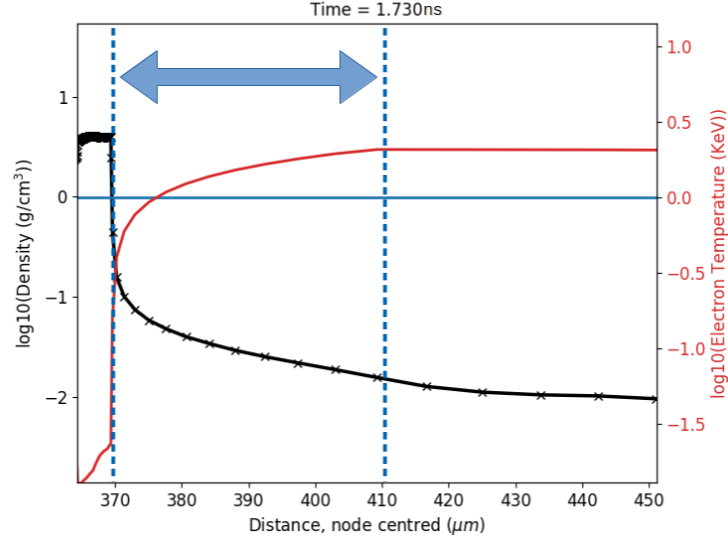


Figure 3.11: Full scale ICF simulation, a cross-section of a 2D simulation. Density is plot in black and temperature in red, the blue dashed lines correspond to, the ablation front at the edge of the shell (left) and the critical density beyond which laser light cannot propagate (right). The blue arrow indicates the region where thermal conduction plays its most critical role in direct drive ICF (transporting energy to ablate the target).

This problem is critical since HEDP regularly exhibits extreme temperature differences, comparable to a heatwave into a cold medium. It is important that the chosen numerical method achieves accurate and robust diffusion in such extreme environments, hence arithmetic conduction is given as a user option in Odin.

### 3.8 Inertial Confinement Implosion

The final test is something which has not been achieved with Pert [1981] explicit, super-stepping method due to issues with robustness, it is a full scale ICF simulation and subsequent observation of the phenomena known as the stand-off distance or conduction zone. Figure 3.11 depicts thermal conduction transporting laser energy from the critical surface (the maximum depth light rays can propagate) to the ablation front (defined by material velocity). This marks an important milestone, as Odin can now be used to effectively simulate ICF implosions. In order to create this simulation, Odin required a direct laser driver, and code to zero the pressure for a “quiet” start before the driver hits, these additions were original work for this Thesis and will be described in more detail below.

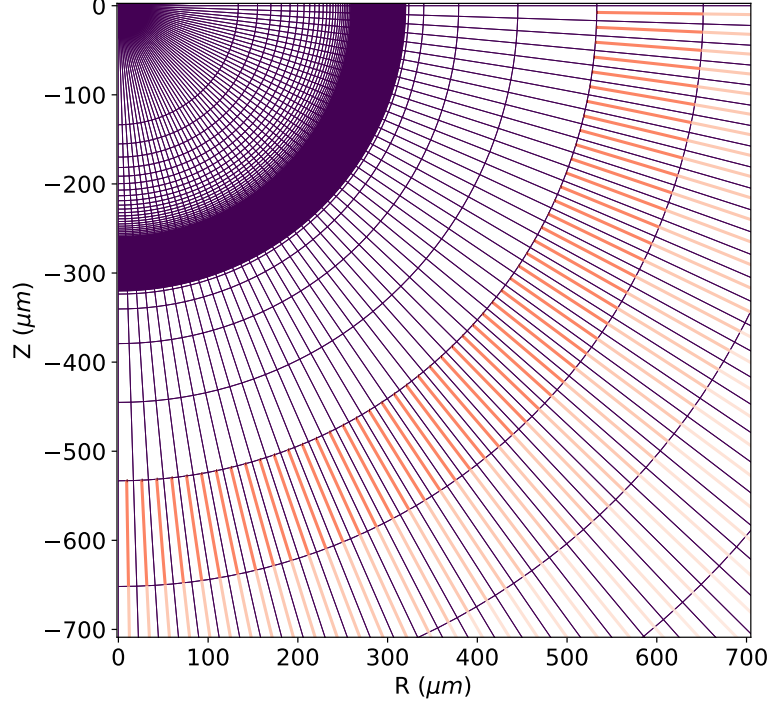


Figure 3.12: Laser rays (red, where darker corresponds to more energy deposited, normalized per ray) travelling on radial trajectories across 2D Odin mesh (purple). The target shell is visible at  $|Z| \sim 300\mu\text{m}$  and the hotspot  $|Z| < 250\mu\text{m}$ .

### 3.8.1 Simplified Laser Model

In order to simulate direct laser driven ICF Odin required a laser model. The module implemented is designed to be a temporary stopgap before a full 3D model is added. The purpose is to be able to investigate hydrodynamics of a target without being held back by the computational expense of a 3D laser model. The rays used in the module trace simple straight paths depositing energy via inverse bremsstrahlung (IB) as they travel, when they reach a material that is over-dense (can no longer propagate) the module has 2 options; it can either deposit all of the energy via idealized resonant absorption (“dumpall”) or the ray can be “reflected” at the critical surface depositing a user defined fraction of its energy and follow the same trajectory back continuing to deposit via IB. The rays do not refract, diffract or perform any of the wavelike behaviour of light, it is a simple straight line model often used with

radial convergence. Figure 3.12 shows radial rays depositing the majority of their energy near the critical surface, also visible is a 2D representation of the conduction zone shown by the gap between the location where the rays deposit their energy ( $\approx 550$  microns) and where the ablation occurs ( $\approx 320$  microns). The simplified trajectories are designed to be computationally efficient, but this is at the expense of accuracy.

The formula for inverse bremsstrahlung was derived in Section 1.2.4 to give deposition,

$$\frac{dE_L}{ds} = -\kappa_{IB} E_L \quad (3.31a)$$

$$\kappa_{IB} = \frac{e^6}{3\epsilon_0^3 c (2\pi m_e k_B)^{3/2}} \frac{Z^2 n_i n_e \log \Lambda}{T^{3/2} \omega_L^2 (1 - \omega_p^2 / \omega_L^2)^{1/2}} \quad (3.31b)$$

where  $E_L$  is the energy in the laser,  $\ln \Lambda$  is the Coulomb logarithm,  $Z$  is the ionic charge state,  $n_e$  is the electron number density,  $T$  is the electron temperature,  $\omega_L$  is the laser angular frequency and  $\omega_p$  is the plasma frequency (see Chapter 4). In Equation 3.31, the first fraction is all physical constants and the second fractions parameters must be determined from the simulation. It is worth noting that as  $Z \rightarrow 0$  so does  $\kappa_{IB}$ , meaning that a different mechanism is required for unionized material. In reality, unionized material is rapidly ionized by high-powered lasers, so it is common to put a lower limit on charge state ( $Z_{min} = 0.02$  was used as default for our model). For uniform illumination when Odin is run in cylindrical geometry weights are applied to the ray's energy depending on their start location.

### 3.8.2 Cold Start (Quiet Start)

Fluid codes are designed to model liquids, gases and plasmas (and other exotic states like warm dense matter), the correction for a solid EoS is to reduce pressure to zero in the region where a material would behave like a solid. The region of transition between states are more difficult to model and ICF is commonly initiated at the triple point for DT. For DT the solid, liquid, gas triple point is  $\approx 18.7K$  (Grilly [1951]) and this is the cryogenic temperature at which many ICF experiments are started. The reason for starting at the triple point is to have a solid DT shell with a gaseous DT fill. The difficulty arises when trying to simulate a material for a long duration (many time-steps) at a transition region. The states should exist in an equilibrium with very little pressure gradients and no bulk sublimation (or the reverse process), however in simulations it is common for materials to slightly deviate one way or another and without the exothermic or endothermic balance on

a microscopic level the system can deform significantly.

Cold start (commonly referred to as “Quiet Start”, see Larsen and Lane [1994a]) is a widely adopted method to force zero pressure in certain regions of the EoS. The EoS itself is not modified since a DT gas beyond  $T \approx 18.7K$ , should exert a pressure therefore it is not wrong it is just numerically sensitive to fluctuations. The method selected to prevent sublimation was to reduce pressure to,

$$p_{cold} = \frac{p_i}{2} \left( 1 + \tanh \frac{5(T_i - T_{cut})}{c} \right), \quad (3.32)$$

where the pressure in a cell with cold start ( $p_{cold}$ ), is equal to the pressure taken from EoS tables  $p_i$  multiplied by a factor that tends to 1 as the temperature in the cell  $T_i$  is greater than the temperature cut-off for the cold start  $T_{cut}$  with a user defined factor  $c$  which controls the width of the tanh function. To ensure, under cooling, no cell will re-enter cold start there is also a binary mask for the grid. Once a cell has reached  $T_i = T_{cut} + 2c$  then the pressure is set to  $p_i$  and cold start feature is off for the rest of the simulation for that cell (no cell can re-enter cold start once heated).

With the addition of the modules shown in this Chapter (including thermal conduction, the diffusion operator for radiation transport, simplified ray tracing and cold start). Odin is capable of simulating ICF implosions to a standard required for experimental analysis and theory. Until a full 3D ray tracking and refraction module is implemented Odin will not have predictive capabilities.



## Chapter 4

# Theory: Hot Electrons

The introduction described mass ablation due to high energy lasers used to accelerate targets. The ablated plasma follows a roughly exponential decrease in density as you travel away from the target. Section 4.1 will describe the conditions and collective behaviour in the plasma, the next section (4.2) will cover how plasma waves can resonate and if undamped lead to laser plasma instabilities (LPI). Lastly, Section 4.3 examines attempts to characterize generated hot electron populations from PIC simulations and experiments.

Presented in this chapter is a literature review of previously published work, except Section 4.3 which includes figures and analysis of the impact of hot electrons on shock ignition (SI) which is original to this Thesis. It is all presented as context for original work in Chapters 5, 6 and 7.

Plasmas consist of free moving electrons and ions. If we assume a hydrogen plasma in thermal equilibrium, the kinetic energy of the particles can be matched so that,  $m_e v_e^2 = m_i v_i^2 \rightarrow v_e/v_i = (m_i/m_e)^{1/2} \approx 43$  giving an electron speed approximately 43 times that of the ions. In laser driven ablation plasmas the ratio can be much higher, as it is the electrons that absorb most of the energy from the laser in a much shorter time ( $\approx 1/\omega_{pe}$ , Equation 4.2) than the electron-ion collision time ( $\approx \tau_{ei}$ , Equation 1.20). Therefore, it is the fast moving electrons that act to neutralize charge imbalance in the plasma. The scale this occurs over is called the Debye length,

$$\lambda_D = \sqrt{\frac{\epsilon_0 k_B T_e}{e^2 n_e}}. \quad (4.1)$$

Interactions on shorter lengths than the Debye length are called “thermal” collisions, which distinguishes them from the plasma’s collective behaviour that give rise to plasma waves. If a small charge imbalance arises, the electrons will move to neutralized but if undamped, they will overshoot and oscillate around the imbalance

at the electron plasma frequency,

$$\omega_{pe} = \sqrt{\frac{n_e e^2}{\epsilon_0 m_e}}, \quad (4.2)$$

which is a standing wave. Damping takes the form of particle collisions that thermalize (randomly distribute) the energy away from the oscillation or Landau damping which accelerates electrons in the thermal population with speeds similar to a plasma wave's propagation speed also damping energy away from the wave (Kruer [2019]).

If an incoming light wave oscillates at the same frequency as the plasma, collisionless absorption will transfer energy to the electrons. This is distinct from the collisional absorption called inverse bremsstrahlung (Section 1.2.4). Equation 4.2 can be rearranged for the wave resonance that defines the critical density for an incoming light wave with frequency  $\omega_L$ ,

$$n_c = \frac{\epsilon_0 m_e \omega_L^2}{e^2}. \quad (4.3)$$

The resonant absorption of laser light that occurs at the critical surface transfers laser energy directly into a small population of electrons (the part of the thermal population that happens to oscillate near the laser frequency  $\omega_L$ ). This population is accelerated from a thermal distribution and so also has a near thermal distribution but at a much higher temperature. They are often referred to as hot electrons. This is the most direct method of creating a hot electron population from laser light. However, laser light rarely reaches the critical surface in ICF plasmas due to the dominance of inverse bremsstrahlung and refraction before reaching the surface. The next two sections will investigate less direct ways of creating a hot electron population.

## 4.1 Plasma Waves

Figure 4.1 shows frequency ( $\omega$ ) against wave-number ( $k$ ) for electron plasma waves (EPW, or langmuir wave), ion acoustic waves (IAW) and electromagnetic waves (EM). The point EM meets EPW is the electron plasma frequency  $\omega_{pe}$ , it is at this point that resonant absorption could occur between the waves. However, the plot is normalized to the laser frequency in a vacuum, so laser energy will be focussed at  $\omega/\omega_0 \approx 1$ . The laser propagates toward the target with wave-number  $kc/\omega_0 \approx 1$ , which defines the positive direction. As the light propagates up the density ramp  $kc$  will become smaller, but  $\omega$  will remain near constant. The EPW will increase

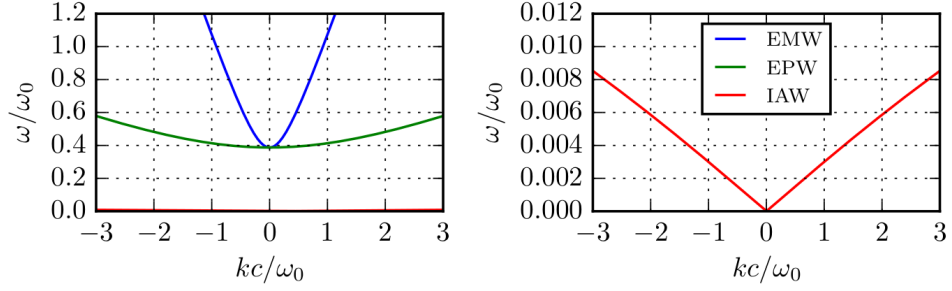


Figure 4.1: The 3-wave dispersion relation of a Maxwellian plasma interacting with light. The three waves are the electromagnetic wave (EM, blue), the electron plasma wave (EPW, green), and the ion-acoustic wave (IAW, red). The dispersion relation depends on the plasma parameters,  $n_e = 0.15n_c$ ,  $T_e = 3.5\text{keV}$ ,  $T_i = 1.7\text{keV}$  and  $Z = 1$  which is typical for LPI in ICF, except  $Z = 3.5$  for the CH plastic material ablated from the targets. The frequency and wave number have been normalised with the laser wave frequency in a vacuum (for  $\lambda_L = 351\text{nm}$ ),  $\omega_0 = ck_0 = \omega_L$ . This image is reproduced from Seaton [2019]

in frequency (as density increases) until resonance occurs at  $\omega_{pe} \approx \omega_L$  and,  $k \approx 0$  which defines a standing wave at the critical density seen in Equation 4.3.

The equation governing the relationship between frequencies and wave-numbers for EM waves in a plasma can be found from a linearized fluid or kinetic description of the interactions (see Kruer [2019]),

$$\omega_{\text{EM}}^2 = \omega_{\text{pe}}^2 + c^2|\mathbf{k}_{\text{EM}}|^2 \quad (4.4)$$

where  $\omega_{\text{EM}}$  and  $\mathbf{k}_{\text{EM}}$  are the frequency and wave-number of the EM wave and the vacuum frequency ( $\omega_0 = ck_0 = \omega_L$ ) of the laser is distinguished from all the EM oscillations that could occur in a plasma  $\omega_{\text{EM}}$ .

The EPW dispersion relation can be derived by linearizing the two-fluid equations,

$$\omega_{\text{EPW}}^2 \simeq \omega_{\text{pe}}^2 + 3v_{th}^2|\mathbf{k}_{\text{EPW}}|^2 \quad (4.5)$$

where  $v_{th}^2 = k_B T/m_e$  which is the thermal velocity for electrons and  $\mathbf{k}_{\text{EPW}}$  is the wave-number of the EPW wave. The equation is accurate for  $k_{\text{EPW}}\lambda_D \ll 1$ . Where EPW with  $k_{\text{EPW}} > 0.25\lambda_D$  are strongly damped for a Maxwellian distribution.

The IAW can be derived in the same fashion as the EPW however IAW are strongly damped by collisions with electrons unless  $T_i \ll T_e$ . For  $k_{\text{IAW}}\lambda_D \ll 1$  the

dispersion relation can be given as,

$$\omega_{IAW} \simeq c_s |\mathbf{k}_{IAW}| \quad (4.6)$$

where  $\mathbf{k}_{IAW}$  is the wave-number and  $c_s$  is the speed of sound in the plasma,

$$c_s = \sqrt{\frac{Zk_B T_e + 3k_B T_i}{m_i}}. \quad (4.7)$$

Equation 4.6 is the same equation that governs sound waves. A more detailed investigation of IAW can be found in Kruer [2019] or Williams et al. [1995].

Equations 4.4, 4.5 and 4.6 correspond to the lines drawn in Figure 4.1. Each point on the line corresponds to an oscillation that would continue if undamped. They do not describe how energy is coupled to the waves from the laser. There are many mechanisms which couple energy to a plasma wave, including resonant absorption the 2-wave interaction described above. The next section will describe the most common 3-wave interactions for ICF (assuming energy starts in the EM wave), although derivation of the growth rates is beyond the scope of this work.

## 4.2 Laser Plasma Instabilities

Considering Figure 4.1 the only way energy can be transferred from the laser with  $\omega_L/\omega_0 \approx 1$  and  $kc/\omega_0 \approx 1$  to another wave is if the momentum,  $p = \hbar k$ , and the energy,  $E = \hbar\omega$ , are conserved. To balance energy and momentum, at least 3-waves are needed (except resonant absorption at the critical density). The main 3-wave interactions for ICF and their names:

$$\begin{aligned} \text{EM} &\rightarrow \text{EPW} + \text{EPW} \quad (\text{two plasmon decay, TPD}) \\ \text{EM} &\rightarrow \text{EM} + \text{IAW} \quad (\text{stimulated Brillouin scattering, SBS}) \\ \text{EM} &\rightarrow \text{EM} + \text{EPW} \quad (\text{stimulated Raman scattering, SRS}). \end{aligned} \quad (4.8)$$

In 1D there is forward and backward SRS and backward scattering SBS, the direction refers to the EM wave-number (where  $\mathbf{k} > 0$  is forward). A useful tool for identifying a conservative interaction is to draw a parallelogram on Figure 4.1 where each corner aligns with a line (blue, green or red) and one corner is on the origin. In order for it to disperse energy from the laser one of the corners also must align with the laser energy at  $\omega_L/\omega_0 \approx 1$  and  $kc/\omega_0 \approx 1$ . This method and Figure 4.1 only consider 1D solutions, however LPI can balance  $\mathbf{k}$  in 3D which gives rise to side-scatter SRS and TPD. For TPD the resultant EPW are not parallel or anti-parallel to the initial

laser propagation. Cross-beam energy transfer (CBET) which is common in ICF is a special case of Doppler shifted SBS with energy transferred between two EM waves travelling in opposite directions and creating an IAW to balance momentum and energy.

For an SRS event that occurs at the  $n_c/4$  we can use Equation 4.2 to find,

$$\omega_{EPW} = \sqrt{\frac{n_c e^2}{4m_e \epsilon_0}} = \frac{\omega_L}{2} \quad (4.9)$$

this can be combined with energy conservation in an interaction,  $\omega_0 = \omega_1 + \omega_2$  to give,

$$\omega_L = \omega_{EM} + \omega_{EPW} = \omega_{EM} + \frac{\omega_L}{2} \quad (4.10)$$

showing that SRS that occur near the  $n_c/4$  surface distributes energy evenly between backscatter (EM) and hot electrons (EPW). SRS is the dominant LPI for SI (Seaton and Arber [2020]; Rosenberg et al. [2018]) and it mostly occurs near the quarter critical surface (but always at  $n < n_{crit}/4$ ). In the rest of this Thesis it will be assumed that hot electrons and backscattered light are given equal amounts of energy unless otherwise stated.

Density scale length ( $L_n$ ) is a key parameter that along with laser intensity ( $I$ ), electron temperature ( $T_e$ ) and density ( $n$ ) indicate which LPI might dominate in a plasma. LPI also relies on a full description of the laser (phase, polarity, etc.) and other factors, making LPI growth and saturation very difficult to predict. Density scale length is defined as,

$$L_n = n_e / \frac{dn_e}{dr} \quad (4.11)$$

where  $n_e$  is the electron number density and  $r$  is the spatial dimension over which the density changes. For SI the key parameters are commonly density scale length  $L_n \sim 500\mu\text{m}$ , intensity between  $I = 10^{15} - 10^{16}\text{W/cm}^2$  and electron temperature  $T_e = 4\text{keV}$ .

LPI in general are non-linear interactions that occur on many scale lengths, requiring collective behaviour and particle dynamics. They are very computationally expensive to simulate on the scales seen in ICF. Experimental diagnostics and Particle-in-cell (PIC) simulation can help diagnose the hot electrons ( $\sim$  EPW) and backscatter light (EM) that they produce. The next section will briefly outline some observed properties of the hot electron population and the inconsistencies.

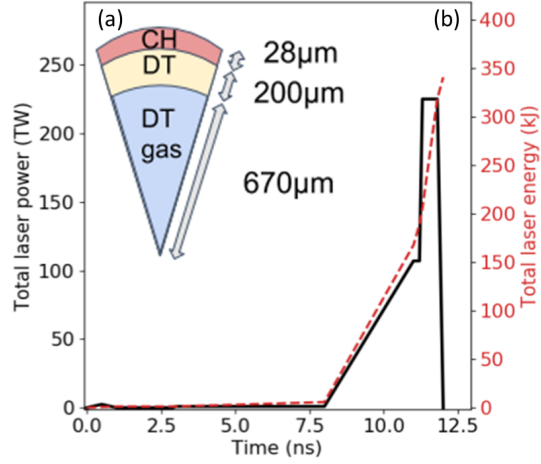


Figure 4.2: (a) A cross-section of the target used in implosion simulations. The capsule shell features a plastic outer layer (CH)  $\rho = 1.05\text{g/cm}^{-3}$ , a DT inner layer  $\rho = 0.25\text{g/cm}^{-3}$ , and a DT gas filled core  $\rho = 0.06\text{g/cm}^{-3}$ . (b) black, solid line shows the laser power deposited due to IB and (“dump-all”) resonant absorption of radial rays at critical density. This is equivalent to laser power emitted after losses due to CBET, target convergence and SRS backscatter are considered and the red, dashed line shows the time integrated power deposited (energy) equivalent to  $\approx 350\text{kJ}$ . As in Atzeni et al. [2019] the predicted laser power at the source to achieve the implosion is between,  $500 - 700\text{kJ}$  which corresponds to laser-target coupling of  $\sim 50 - 75\%$  typical of ICF and SI. The peak power of  $220\text{TW}$  corresponds to a laser intensity at  $n_{crit}/4$  ( $\approx 1100\mu\text{m}$ ) of  $I \approx 10^{16}\text{W/cm}^2$ .

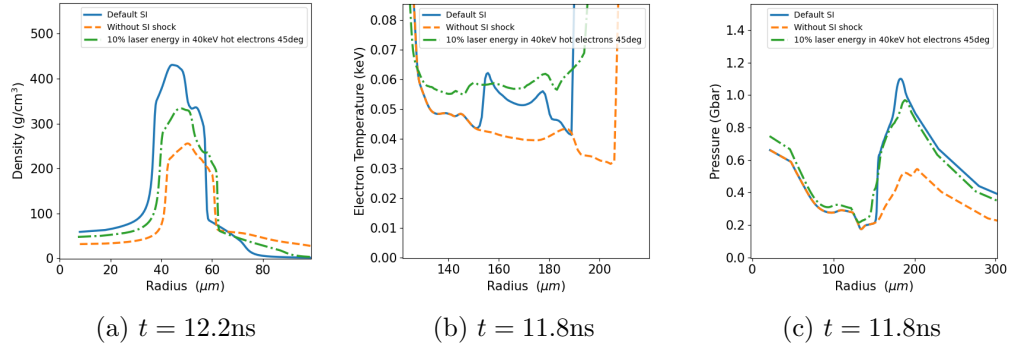


Figure 4.3: Simulations investigating the effect of hot electrons on SI. Blue solid lines are from a SI simulation without hot electrons. Orange dashed lines are from a simulation without a SI spike. All simulations are run without alpha heating. Green dash-dot lines are from a simulation which will be the base of a parameter scan of hot electron characteristics. The base hot electron characteristics are beam size corresponding to a uniform solid angle of  $2\pi(2 - \sqrt{2})/2$  sr equivalent to a half cone angle of  $45^\circ$ , laser to hot electron conversion percentage 10% and temperature of 40keV. (a) shows the density at peak compression, a simple measure of implosion success, (b) shows the background electron temperature near peak velocity in the cold fuel demonstrating hot electron preheat, and (c) shows the fluid pressure near peak velocity. Also visible is the hot electrons' effect on the SI shock ( $\approx 175\mu\text{m}$ , green, dash-dot), spreading it over a larger length to appear more like a pressure wave (as seen in the orange, dashed line).

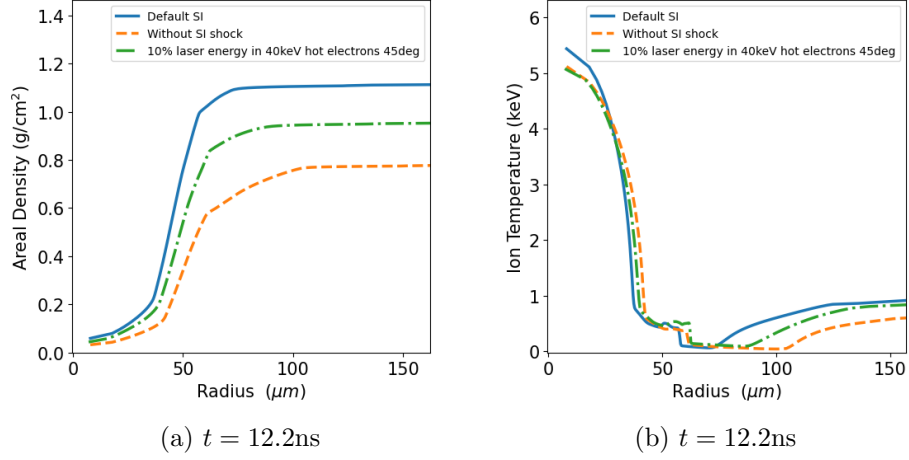


Figure 4.4: The same simulations as Figure 4.3 but looking at the ignition parameters, (a) areal density and (b) ion temperature from Equation 1.5 during peak compression. The maximum areal density decreases  $\approx 15\%$  when hot electrons are simulated and again by  $\approx 15\%$  when the SI spike is removed, however there is very little change in hotspot ion temperature. The areal density and ion temperature of the SI simulation without hot electrons (blue line) is comparable to direct drive, central hotspot ignition simulation seen in Craxton et al. [2015], (fig.3–5) which achieves a gain of  $\sim 50$ .

### 4.3 Hot Electron Characteristics

At the intensities of interest to SI,  $I \sim 10^{15} \text{W}/\text{cm}^2$  to  $10^{16} \text{W}/\text{cm}^2$  for laser wavelength 351nm, hot electrons are predicted to have a thermal distribution with  $20\text{keV} < T_h < 100\text{keV}$ . The hot electrons are thought to be generated with a total population kinetic energy between 1% and 30% of the incident laser energy increasing with intensity (scattered light takes between 5% and 80%) Shang et al. [2017]; Scott et al. [2021]; Colaitis et al. [2016]. The most common notation in the literature is,  $\eta = E_{he}/EL$  where  $E_{he}$  is the total energy deposited by the hot electrons and  $E_L$  is the total emitted laser energy in the pulse (see Rosenberg et al. [2018]). This measure is very sensitive to target geometry, and laser pulse shape. Due to the variety of experiments being modelled and the practicalities of programming a hot electron model, this Thesis will use a different metric. The instantaneous laser to hot electron conversion fraction at the quarter critical surface  $\eta_{qc}$  (by definition  $\eta_{qc} > \eta$ ), is used as a user input into Odin and is directly comparable across laser pulse shapes and target geometries. Values for  $\eta_{qc}$  are approximately within a range  $0.01 < \eta_{qc} < 0.3$ .

There are many experiments aimed at investigating backscatter fraction, hot



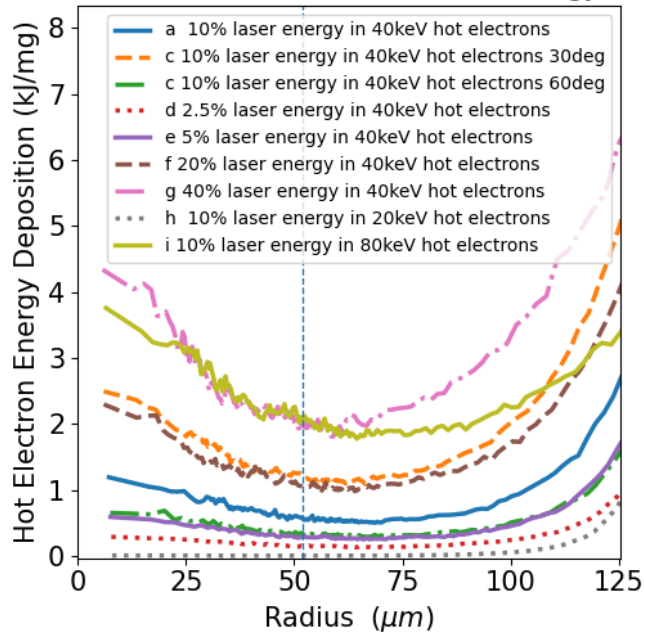


Figure 4.5: Hot electron characteristics parameter scan examining preheat at 12.0ns (time-integrated preheat). Centralized is the blue dashed vertical line which indicates the separation between hotspot and shell. The solid blue line is the base hot electron characteristics shown in Figure 4.3, a uniform beam over a cone with half angle of  $45^\circ$ , laser to hot electron conversion percentage 10% and temperature of 40keV. Preheat is most deleterious in the cold fuel between  $50 - 75\mu\text{m}$ .

electron energy fraction ( $\eta$ ) and hot electron temperature ( $T_h$ ) for direct drive ICF (a good summary can be found in Craxton et al. [2015]) but there is currently no published studies reporting hot electron parameters for the plasma conditions and intensities seen in SI  $\sim 10^{15}\text{W/cm}^2$  to  $10^{16}\text{W/cm}^2$  (Scott et al. [2021]). PIC simulations on the relevant scales for SI are computationally expensive due to the volume of plasma needed to model growth, saturation and pump depletion of LPI, but attempts can be seen in Seaton [2019], Yin et al. [2012], Klimo et al. [2010] and Myatt et al. [2014], to name some of the most relevant to ICF and SI. The hot electron’s angular distribution is not well characterized by experiment, with the only relevant experiment (Yaakobi et al. [2013]) giving an estimate of  $\sim 1/4$  of hot electrons incident on the target. PIC simulation (Seaton [2019]) shows a large fraction of the hot electrons are beamed. There is still a large uncertainty in the angular distribution of the hot electrons and whether it is sensitive to plasma parameters or laser intensity. For the purpose of this work, the hot electrons will emit uniformly over a solid angle (cone) characterized by a half cone angle  $\theta$ .

#### 4.3.1 Parameter Scan Setup and Comparison Simulations

To investigate SI implosion sensitivity to a range of hot electron characteristics, a parameter scan changing hot electron energy conversion fraction from laser energy  $\eta$ , temperature  $T_h$ , and cone angle  $\theta$  was performed using Odin simulations (with target and pulse shape based on Atzeni et al. [2019]) and the hot electron model described in Chapter 5. The target layout and laser pulse shape are shown in Figure 4.2 and will be used for SI simulations throughout chapters 6 and 7. The parameter scan shown in this section differs from other SI simulations in this Thesis as radiation transport was not modelled, and a lower radial resolution was used (due to computational expense). The target is uniformly illuminated using the ray model discussed in Section 3.8.1. The hot electrons are emitted from each ray at the quarter critical surface (schematic in Figure 5.1) meaning that they too are incident uniformly on the target. The entire implosion keeps close to spherically symmetric.

To evaluate the effect of hot electrons on a SI implosion, a comparison simulation without the final igniter shock was also simulated. The “worst-case” for SI is that the hot electrons generated disrupt the implosion to the extent that the late stage spike offers no benefit to achieving ignition.

### 4.3.2 Base Hot Electron Simulation for Parameter Scan

Figure 4.3 shows the two comparison implosions and a “base” simulation for the parameter scan with hot electron characteristics approximately in the middle of the ranges predicted for SI, with a beam size corresponding to a uniform solid angle of  $2\pi(2 - \sqrt{2})/2 \text{ sr} \approx 1.84 \text{ sr}$  equivalent to a half cone angle of  $\theta = 45^\circ$ , laser to hot electron energy conversion at quarter critical 10% ( $\eta_{qc} = 0.1$ ) and temperature of  $T_h = 40 \text{ keV}$ . Due to the uncertainty in hot electron characterization from experiment and PIC simulation, the selection of hot electron characteristics could also be made to cause a peak compression density halfway between the no hot electron simulation and the “worst-case” mentioned above. The author is not claiming this is the most likely hot electron population, it is just roughly in the middle of characterizations seen in literature and when SI is simulated causes a peak compression density in between the unaffected implosion and “worst case” implosion densities. Figure 4.3 (a) shows density at peak compression,  $\approx 12.2 \text{ ns}$  (near stagnation), but capsule temperature (b) and shock pressure (c) at peak velocity  $11.8 \text{ ns}$  a critical time for SI as the igniter shock is about to collide with the hotspot back pressure shock.

In the plot of areal density shown in Figure 4.4 (a) areal density of the simulation with hot electrons is also halfway between the comparison simulations. There is a reduction in peak areal density of 15% due to hot electrons and so using the simple implosion metrics given in Equation 1.5,  $\chi \propto \rho R$ , the degradation in  $\chi$  due to hot electrons is also  $\sim 15\%$  (since Figure 4.4 (b) shows ion temperature at peak compression is almost unmodified by the hot electrons). To understand the cause of the implosion degradation, it is useful to define target preheat.

### 4.3.3 Target Preheat

Preheat occurs when hot electrons from the high energy tail of the thermal distribution penetrate into the cold fuel and deposit their energy. It is commonly quoted as hot electrons with kinetic energy  $> 100 \text{ keV}$  (Rosenberg et al. [2018]). They heat the cold fuel of the target before peak convergence, increasing the target adiabat and reducing compressibility. Another definition more relevant for SI would be the amount of hot electron energy that is deposited beyond the igniter shock. Preheat is visible as the change of the capsule temperature in Figure 4.3 (b). The maximum acceptable levels of preheat for a direct drive implosion is given in Radha et al. [2016] as  $\sim 0.1\%$  of laser drive energy, which is  $\sim 1 \text{ kJ}$  for a Megajoule laser pulse. The limit  $\sim 0.1\%$  and an estimated cold fuel mass of  $\sim 1.0 \text{ mg}$  can be used to give

a preheat limit per unit mass of cold fuel  $\sim 1.0\text{kJ/mg}$  which are the units used in Figure 4.5.

#### 4.3.4 Preheat Variation in Parameter Scan

Time integrated hot electron energy deposition is shown in Figure 4.5 for a capsule starting to decelerate toward stagnation. The Figure shows the change in preheat if the parameters:  $\theta$ ,  $\eta_{qc}$  or  $T_h$  are varied from the “base” values one at a time (an OAT parameter scan). Energy deposition between  $50 - 75\mu\text{m}$  in Figure 4.5 is particularly harmful as that is in the unshocked material at the edge of the hotspot. The material at the edge of the shell is susceptible to melt/ablate into the hotspot increasing hotspot mass and the energy required to ignite it (Colaitis et al. [2016]). All simulations that exceed  $\approx 1\text{kJ/mg}$  at  $50\mu\text{m}$  do not appear to benefit over the “worst-case” implosion that is simulated without a SI spike.

Figure 4.5 shows that changing either hot electron beam size ( $\theta$ ) or total energy fraction ( $\eta_{qc}$ ) can cause very similar amounts of preheat. To calculate why, we can investigate target geometry. During the SI spike ( $11.3 - 11.8\text{ns}$ ) the radius of the ablation front is  $\approx 300\mu\text{m}$  and the quarter critical is  $\approx 1000\mu\text{m}$ , giving a target solid angle of  $\approx 0.84\text{sr}$  (cone half angle  $30^\circ$ ) which means for the base hot electron angular distribution ( $\approx 1.84\text{sr}$ ) that  $\approx 46\%$  of hot electrons are initiated pointing within the ablation front (capable of causing preheat, twice the amount seen in Yaakobi et al. [2013]). When the angle of the cone is reduced to  $30^\circ$ , as denoted by the orange dashed line in Figure 4.5, then  $\approx 100\%$  of hot electrons are initiated pointing within the ablation front and the line matches closely with the brown dashed line corresponding to doubling the number of hot electrons. A similar argument can be made for the alignment of the green dash-dot line solid angle  $\pi\text{sr}$  and the purple line, which corresponds to half the total number of hot electrons. The equivalence is not exact because hot electron energy that misses the target will not increase shock pressure.

#### 4.3.5 Parameter Scan Implosion Analysis

Figures 4.6, 4.7 and 4.8 plot peak compression density (a), peak velocity capsule temperature (b) and pressure (c) as was done for the “base” simulation in Figure 4.3, but each displays what occurs when a different hot electron characteristic is varied. Laser to hot electron energy conversion fraction  $\eta_{qc}$  is varied in Figure 4.6, hot electron cone angle  $\theta$  is varied in Figure 4.7 and, hot electron temperature  $T_h$  is varied in Figure 4.8. Each time, only one parameter is varied from the “base” value

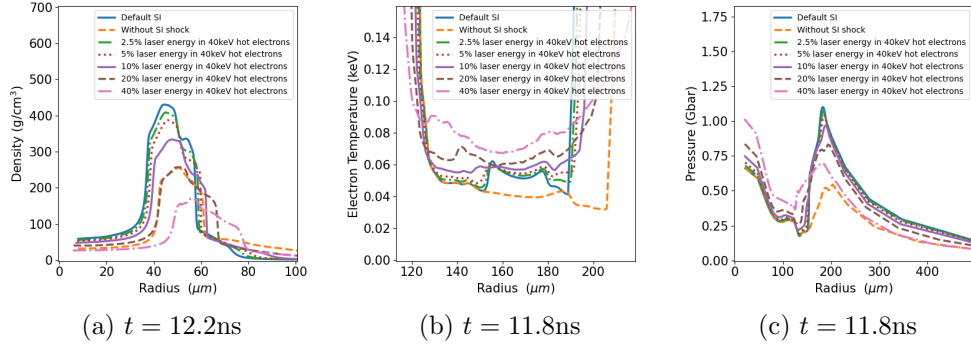


Figure 4.6: Parameter scan of hot electron energy fraction at quarter critical ( $\eta_{qc}$ ), where modification is made from the “base” hot electron characteristics simulation shown in Figure 4.3. From peak compression density (a) it is visible that a  $\eta_{qc} = 0.4$  (pink, dash-dot line) is worse than the simulation without a SI spike (orange, dashed line) despite having a stronger shock in (c). Also visible is the increase in shell width at peak compression as  $\eta$  increases. The background electron temperature in (b) shows  $\eta_{qc} < 0.1$  does not significantly preheat ahead of the shock at  $\approx 150\mu\text{m}$ . The igniter shock pressure (c) demonstrates that hot electrons can modify shock timing  $\eta_{qc} = 0.4$  (pink, dash-dot line).

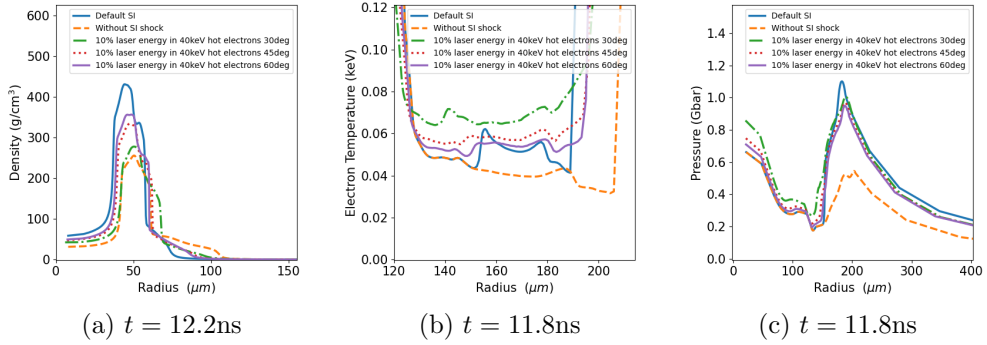


Figure 4.7: Parameter scan of hot electron beam size where angles quoted correspond to a half cone angle ( $\theta$ ). Emission is uniform over the cone/beam. Modification is made from the “base” hot electron characteristics simulation shown in Figure 4.3. The target (defined by material within the ablation surface), when viewed from quarter critical, occupies a solid angle of  $\approx 0.84\text{sr}$  (cone half angle  $30^\circ$ ) meaning that the green dash-dot line corresponds to the most deleterious angle. If the angle were further reduced, the change in deposition would be small (although path length and incident angle to the target would be reduced) since the dominant effect of modifying beam size appears to be the fraction of hot electrons that are incident on the target. An isotropic distribution of hot electrons would result in preheat four times smaller than the purple solid line, which occupies a solid angle of  $\approx \pi\text{sr}$ . More drive energy would be wasted, so even an isotropic distribution would not improve peak compression density much compared to that of the purple line.

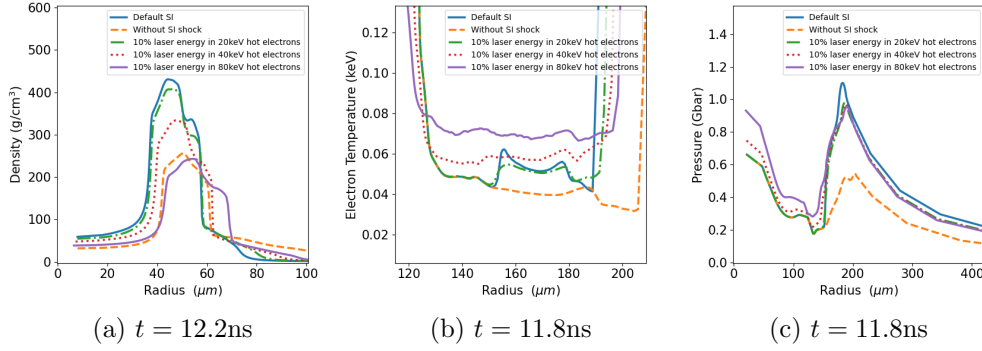


Figure 4.8: Parameter scan of hot electron temperature ( $T_h$ ), where modification is made from the “base” hot electron characteristics simulation shown in Figure 4.3. It is expected that a low hot electron temperature would improve shock formation, but the green dash-dot line in (c) shows even a cold population is deleterious to shock formation. This is not due to preheat as very little is visible in (b) but is better explained by wasted laser drive energy from hot electrons not incident on the target or not making up the density ramp to the ablation front. The peak compression density shown in (a) is almost unaffected by the low temperature hot electrons  $T_h = 20\text{keV}$ . High temperature hot electrons  $T_h = 80\text{keV}$ , purple solid line appear to leave the shock front in (c) unaffected compared to the base characteristics (red dotted line) and cause near uniform preheat throughout the target. The high temperature population would be easy to model (with a straight line model or preheat multiplier over the entire grid) due to its near uniform energy deposition and would likely not prevent SI if  $\eta_{qc} < 0.05$  or  $\theta > 60^\circ$  taking it below the  $1\text{kJ/mg}$  limit on Figure 4.5

at a time (an OAT parameter scan). Each simulation corresponds to a line in the preheat comparison shown in Figure 4.5.

All hot electron populations modelled in Figures 4.6, 4.7 and 4.8 have a deleterious effect on the implosion, achieving ignition. It is possible to modify two or more parameters to create a hot electron population that causes shock support that outweighs the deleterious effects of preheat. Shock support is defined for SI as the energy of hot electrons deposited behind the shock front. Some simulations (Shang et al. [2017]) have shown that energy deposited in this region can drive the igniter shock more efficiently. The parameters explored here show little explicit shock support, however in Figure 4.7 (c) the strongest shock (of the hot electron simulations) has the smallest cone angle. Shock timing modification is visible in Figure 4.6 (c) where  $\eta_{qc} = 0.4$  and is often attributed to either preheat or shock support. Modification in shock timing is critical for SI and can compound the deleterious effects of preheat if not accounted for. Chapter 6 will explore the role hot electrons have on shock timing in more detail.

Figure 4.8 reveals the importance of a full kinetic particle tracking and scattering model for hot electrons  $\sim 40\text{keV}$ . Much hotter and uniform energy deposition occurs, implying a large portion of the population deposit energy without scattering (a straight line model could achieve high accuracy). Much cooler and the hot electrons don't penetrate to the ablation front, implying a diffusive model could provide sufficient accuracy.

## Chapter 5

# Application and Tests: Hot Electrons

This Thesis presents original work to create a 3D Monte-Carlo hot electron model for simulation in the hydrodynamic code Odin. The particle paths were tracked and scattered in 3D space, but the resulting energy deposition is done on the 2D Odin grid. Listing the sections in order and the contributions made by the author to each: the application will be described in Section 5.1, followed by the tests used to verify the model in Section 5.2. The application is split into path tracking (Section 5.1.1, which was work primarily done by Keith Bennett with some contributions and bug fixes from the author); energy sampling (Section 5.1.2), deposition (Section 5.1.3) and scattering (Section 5.1.4) all of which were original work with some minor contributions and bug fixes from development team; hot electron refluxing (Section 5.1.5) is not well quantified in the literature and the novel approach was implemented by the author (with theoretical discussion from Philip Bradford); and the final part of the application (Section 5.1.6) will cover possible future work. The test section will be split into a test focused on checking energy deposition (Section 5.2.1), followed by a test comparing scattering to the MCNP code (see Werner et al. [2018], Section 5.2.2).

### 5.1 Application

The aim of the project is to model hot electrons generated from LPI near the quarter critical surface, propagate them to accurately capture energy deposition (including preheat) and determine the effect they have on an implosion, especially shock dynamics. Figure 5.1 gives a schematic of hot electron generation, scattering



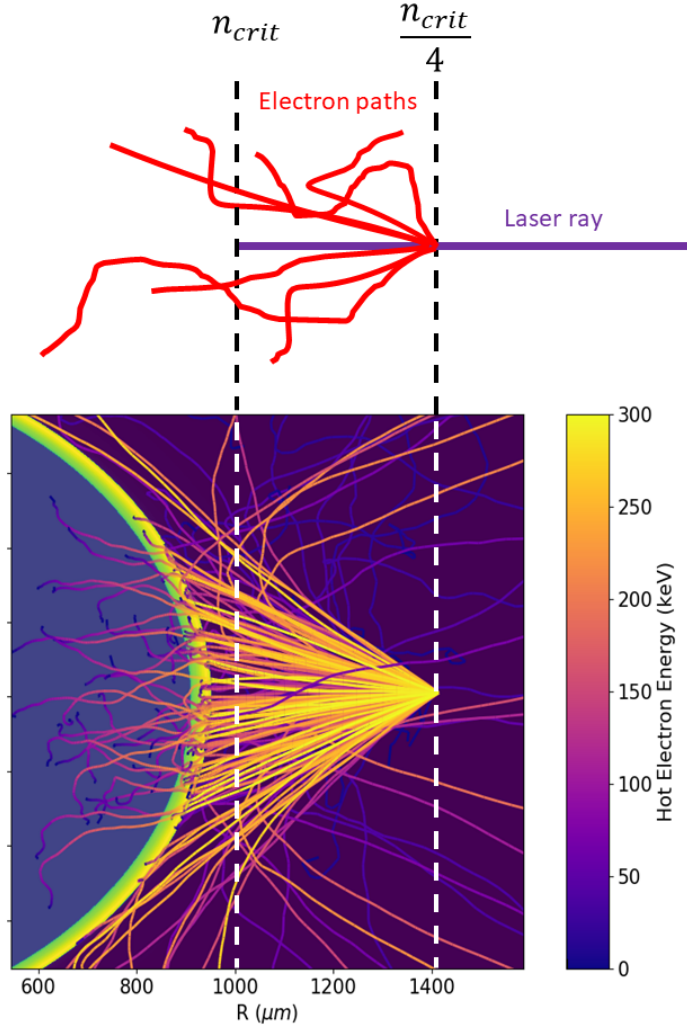


Figure 5.1: Top: Schematic demonstrating how hot electrons are generated from laser rays at the quarter critical surface. Bottom: Odin diagnostic showing the density of a solid plastic target (colour bar not shown) with electrons paths emitted from a single ray overlaid (for more details on the target, see Chapter 6). The colour axis refers to the hot electron path energy.

and deposition in addition to an Odin diagnostic output. The method selected to trace the particles is a hybrid scheme where alongside Odin’s charge neutral, fluid of ions and electrons, there is a smaller population of non-local, kinetically modelled hot electrons (which aren’t confined to a cell). The hot electrons also have a thermal population, which is modelled with a number of mono-energetic macro-particles. The creation of hot electrons breaks particle and charge continuity (it is a source and their final stopping location is a sink). The size of the hot electron population is small ( $< 10^{11}$  particles) compared to the number of electrons in a single cell ( $> 10^{15}$  particles) so the movement of mass is neglected in this approach. A return current is inferred which locally preserves charge neutrality (Robinson et al. [2014]) but is not modelled. The calculation of ohmic heating due to the return current in Section 5.1.3 demonstrates that it is small compared to the deposition of hot electron kinetic energy and so its addition is left for future work.

There is a comprehensive particle tracking toolkit, called GEANT4 (Agostinelli et al. [2003]), which can be coupled to a fluid code. This would provide state-of-the-art kinetics, however it would mean that the fields generated by the particles could not contribute to MHD in Odin. The field contribution has not been added in this work, but its addition is seen as a critical future step for Odin’s hot electron module, and so GEANT4 was not used. Field contributions will be discussed in the future work Section 5.1.6.

The majority of the application section follows the literature with little modification, however there is no published work describing the addition of a reflux model to a Monte-Carlo particle tracker in a fluid code as seen in Section 5.1.5.

### 5.1.1 Path Tracking

The particle tracking was performed in 3D, it required the rotation of the 2D Odin domain and the mapping of the hot electron energy deposition output back onto the 2D domain. Odin’s cylindrical polar “RZ” coordinate system is rotated about the z-axis to create a mesh of hexahedrons (irregular cuboids). The total number of nodes in the direction of rotation is defined by  $N_\theta = (N_r N_z)^{1/2}$  the number of nodes in  $N_r$  and  $N_z$ . The faces of the hexahedrons that are in the radial plane are all exact reproductions of Odin’s RZ plane and the other faces are created by simply joining the vertices (cylindrical symmetry). Each cell in the RZ Odin grid forms a discretized torus in 3D space, after the energy is deposited on the 3D grid the rotation can be reversed (collapsing the torus to 2D) and the energy summed around each rotation. The routine is written to operate with shared memory in OpenMPI since the problem is not easily parallelized on distributed memory, the

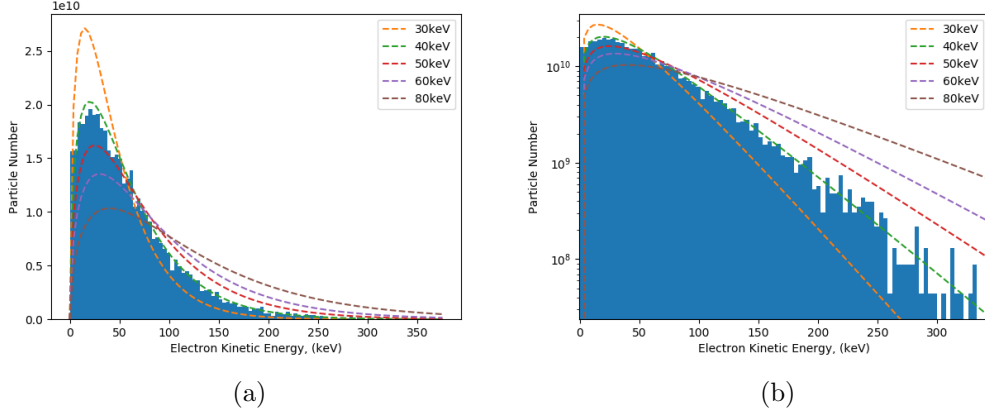


Figure 5.2: (Left) Linear and (Right) logarithmic particle distributions. The histogram represents a 40 keV thermal hot electron emission distribution using Odin’s direct sampler with 10,000 paths, each path is mono-energetic. Direct/Monte-Carlo sampling gives each path an equal number of electrons and uses the cumulative distribution function to weight initial electron energy.

rest of Odin is MPI parallel.

The path tracking updates the electron trajectory at mesh faces (of the hexahedrons). The issue with updating only at mesh faces is that scattering will be less accurate on poorly resolved grids when compared to the method described in Atzeni et al. [2008]. If the particle trajectory is poorly resolved, the energy deposition will also be less accurate.

### 5.1.2 Sampling

In Chapter 4 it was discussed that the hot electron populations can be modelled with a Maxwellian distribution. In order to represent a Maxwellian, a number of mono-energetic groups can be sampled from the particle distribution. As the number of groups tends to the particle number, the accuracy of the sampling converges. The energy taken from the laser path was split into the groups, each allocated an initial energy per electron and a number of electrons. Since each group had a different initial energy per electron they deposit energy and scatter at different rates, so each group was allocated a separate path.

In Odin, the two methods of sampling are defined by: an equal number of particles per group, with initial electron energies determined using inversion of the particle cumulative distribution function (Monte-Carlo/direct sampling) or uniformly distributing groups across energy space, and using particle weighting to form a Maxwellian (uniform sampler). The two options have complimentary strengths,

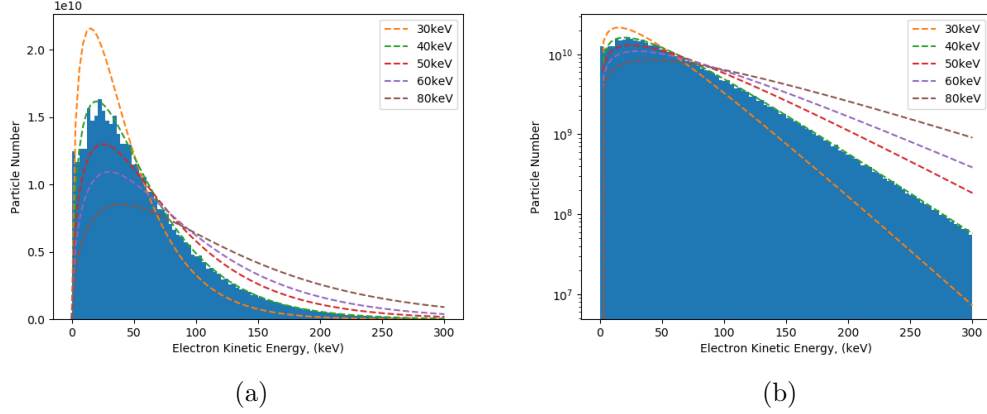


Figure 5.3: (Left) Linear and (Right) logarithmic particle distributions. The histogram represents a 40 keV thermal hot electron emission distribution using Odin’s uniform sampler between 0 and 300 keV with 10,000 paths, each path is mono-energetic. Uniform sampling spread the paths uniformly in energy space (initial electron energy) and use particle number weighting from the probability distribution function.

a uniform sampler covers energy space most effectively and is recommended for 1D/symmetric problems whereas the Monte-Carlo sampler allocates the most paths to the region of the particle distribution that has the most energy, and it will give the fastest convergence for asymmetric problems. The Maxwellian energy distribution being sampled is,

$$f(x) = 2\sqrt{\frac{x}{\pi\theta^3}} \exp\left(\frac{-x}{\theta}\right), \quad 0 < x \quad (5.1)$$

where  $x = 1/2mv^2$ , the kinetic energy of a particle and  $\theta = k_B T$ . Equation 5.1 is used to find the probability of a particle with kinetic energy  $x$  from a thermal distribution defined by  $\theta$ . The total number of particles in the distribution can be defined,

$$N_{part} = \frac{E_{tot}}{\langle x \rangle} \quad (5.2)$$

where  $\langle x \rangle = 3/2k_B T$ , the mean particle kinetic energy and  $E_{tot}$  is the total energy in the system (defined by the LPI).

Direct (Monte-Carlo) sampling is achieved through inversion of the cumulative distribution function (CDF) to find each sample’s initial particle kinetic energy  $x$ . Direct inversion of a CDF for a Maxwellian is given in Vujic [2008],

$$x = \theta \left( -\log \xi_1 - \log \xi_2 \cos^2 \frac{\pi}{2} \xi_3 \right) \quad (5.3)$$

where  $\xi$  are three independent pseudo-random numbers. The number of particles per sample/group is equal and defined by,

$$N_i = \frac{N_{part}}{n_{groups}} \quad (5.4)$$

where  $N_i$  is the number of particles in a group,  $N_{dist}$  is the total number of particles (in a distribution), and  $n_{groups}$  is the number of groups per distribution. There are two computational issues with this method, pseudo-random number generation can be expensive and if a new particle distribution is required (non-Maxwellian) the CDF must be inverted which can be non-trivial. Energy sampling done via the Monte-Carlo, direct inversion method can be seen in Figure 5.2. As seen on the logarithmic plot, there is a lack of paths representing the high energy electrons.

Uniform sampling is performed by,

$$x_i = \frac{x_{cut}}{n_{groups}} i \quad (5.5a)$$

$$N_i = 2\sqrt{\frac{x_i}{\pi\theta^3}} \exp\left(\frac{-x_i}{\theta}\right) \frac{N_{part}}{n_{groups}} \quad (5.5b)$$

where  $x_i$  is the expected energy of a particle in group  $i$ ,  $N_i$  is the number of particles in a group,  $N_{part}$  is the total number of particles,  $n_{groups}$  is the number of groups per distribution and the distribution must be sampled with an energy cut-off  $x_{cut}$ . For accurate sampling the cut-off should be sufficiently high to include the majority of the distribution's energy. For example a 50 keV thermal distribution of electrons has  $\approx 26\%$  of particles above 100 keV energy per particle, but they carry  $\approx 54\%$  of the distribution's energy, for many simulations this would represent too much of the population unaccounted for. The same distribution has  $< 1\%$  of particles with energy over 300keV and they carry  $\approx 3\%$  of the distribution's energy. Figure 5.3 shows uniform sampling, and it's strength in comparison to direct sampling in Figure 5.2.

### 5.1.3 Energy Deposition (Stopping Power)

Energy deposition is discretized per cell. The model used is reduced from a full physics kinetic model, as there is no collective behaviour or return current. A rough calculation of return current and ohmic heating can be estimated using Figure 5.3 for the hot electron number emitted in  $\Delta t \approx 0.1\text{ps}$  which is  $n_e \sim 10^{11}$  and information about the surface they were emitted from  $A \sim 2\pi \times 1\text{mm} \times 20\mu\text{m} \approx 10^{-7}\text{m}^2$ . The

surface is similar to Figure 5.1 where the cell width at quarter critical is  $\approx 20\mu\text{m}$  and the quarter critical surface is at  $\approx 1\text{mm}$  but in cylindrical polar coordinates giving the factor  $2\pi$ . The current density of the hot electrons is,

$$j_h = \frac{en_e}{At} = 10^{12}[\text{Am}^{-2}]. \quad (5.6)$$

Following the method shown in Robinson et al. [2014], this current density will generate an electric field at the rate,

$$\frac{E}{t} = -\frac{1}{4\pi\epsilon_0} \int j d\Omega \approx -\frac{j_h}{\epsilon_0} \approx 10^{12}[\text{Vm}^{-1}\text{ps}^{-1}] \quad (5.7)$$

within picosecond the field strength would be large enough to stop MeV hot electrons (assuming a wide hot electron beam angle). Hot electrons have been observed, so a return current,  $j_b$  must be created that cancels the hot electron current (Bell et al. [2006]),

$$j_h + j_b = 0. \quad (5.8)$$

The return current cancels locally otherwise large magnetic fields would be generated, that are not observed. Using a plasma resistivity,  $\eta \sim 10^{-7}$  and ohms law the resistive electric field is,

$$E \approx -\eta j_f \approx 10^5 \text{Vm}^{-1} \quad (5.9)$$

which results in ohmic heating of (power  $P$  per volume  $V$ ),

$$\frac{P}{V} = -\eta j_f^2 = 10^{17} \text{Wm}^{-3} \quad (5.10)$$

which is equivalent, at solid density, to  $\sim 1\text{J/mg}$  or  $\sim 0.5\text{eV}$ . This amount of ohmic heating from the return current and hot electrons is not significant compared to the  $\sim 1\text{kJ/mg}$  that the hot electron deposit from their kinetic energy. The deposition depends only on fluid properties and the 3D path length. The equation of energy deposition (stopping power per unit distance travelled)  $dE/dr$  is the same for all states of matter and is given by,

$$\frac{dE}{dr} = -\frac{n_e e^4}{4\pi\epsilon_0^2 m_e c^2 \beta^2} L_d \quad (5.11a)$$

$$L_d = \ln \frac{pv}{\sqrt{\gamma+1}\hbar\omega_p} - \frac{\ln 2}{2} + \frac{9}{16} + \frac{(1/2)\ln 2 + 1/16}{\gamma^2} - \frac{\ln 2 + 1/8}{\gamma} \quad (5.11b)$$

notation from Robinson et al. [2014] but equation from Seltzer and Berger [1984], where  $n_e$  is the electron number density (bound and free),  $\gamma$ ,  $v$  and  $p$  are the relativistic parameter, velocity and momentum of the hot electron,  $\omega_p$  is the plasma frequency (applying Equation 4.2 but  $n_e$  corresponds to all electrons bound and free).  $L_d$  is a dimensionless parameter called the drag term. At lower electron energies, it is called the Coulomb logarithm and assigned the symbol  $\ln \Lambda$ . The equation does not account for bremsstrahlung or atomic binding energies.

For ionized material, Equation 5.11b relies on the approximation that the hot electrons have kinetic energy several times greater than the average background population ( $m_e v_h^2 > kT_e$ ). For a Maxwellian distribution of hot electrons at  $T_h = 40\text{keV}$  and a coronal plasma at  $T_e = 4\text{keV}$  not all the electrons will fulfil this requirement ( $\approx 15\%$  of the energy in the  $T_h = 40\text{keV}$  Maxwellian distributions is below  $15\text{keV}$ ) however the low energy hot electrons deposit their energy within a single cell, meaning accuracy at low energies is less important to the hydrodynamics (the same argument can be applied to higher energy hot electrons as they cool, and their kinetic energy approaches that of the background population).

For unionized material, Equation 5.11b is only true if the hot electrons are highly relativistic, due to the approximation used for the density effect, an effect which was first published in Fermi [1940]. The density effect corresponds to a reduction in energy deposition due to the material polarization modifying the electric field of the incident particles. In general, the density effect is measured empirically and then fit numerically using an implicit calculation of the electron excitation states. The approximation used in this work starts with,

$$L_d = \ln \left( \sqrt{\gamma + 1} \frac{E}{I_{\text{ex}}} \right) - \frac{\ln 2}{2} + \frac{1}{16} + \frac{(1/2) \ln 2 + 9/16}{\gamma^2} - \frac{\ln 2 + 1/8}{\gamma} - \frac{\delta}{2} \quad (5.12)$$

in place of Equation 5.11b and uses,

$$\frac{\delta}{2} \rightarrow \ln \left( \frac{\gamma \hbar \omega_p}{I_{\text{ex}}} \right) - \frac{v^2}{c^2} \quad v \rightarrow c \quad (5.13)$$

(as seen in Solodov and Betti [2008]; Robinson et al. [2014]), to remove the dependency on  $I_{\text{ex}}$ , the mean electron excitation energy, from the stopping formula resulting in Equation 5.11b. The model is only accurate when  $\gamma \hbar \omega_p \gg I_{\text{ex}}$ . For solid density plastic  $\gamma \hbar \omega_p \approx 15\text{eV}$  and  $I_{\text{ex}} \approx 60\text{eV}$  (Davies [2002]) so unless the material is ionized the electron will need  $\gamma \gg 4$ .

A further approximation, is that hot electrons travel instantaneously, within a single hydrodynamic time step, distance travelled and electron velocity are used to

discretize Equation 5.11. The impact of the issue for ICF is thought to be small, and the fix is computationally expensive, so the instantaneous approximation is upheld by this Thesis, but further correction is left to future work. This approximation also affects the scattering.

#### 5.1.4 Scattering

Hot electron scattering is discretized by the mesh faces, the equation below shows the change in RMS scatter angle per unit distance travelled  $d\langle\theta^2\rangle/dr$  from interaction with a fully ionised fluid,

$$\frac{d\langle\theta^2\rangle}{dr} \approx \frac{n_e e^4}{2\pi(\varepsilon_0 p v)^2} \left[ (Z+1)L_s - \frac{1}{2} \ln \frac{\gamma+3}{2} \right], \quad (5.14a)$$

$$L_s \approx \ln \frac{2\lambda_D p}{\hbar} - 0.234 - 0.659 \frac{v^2}{c^2}, \quad \frac{2\lambda_D p}{\hbar} \gg 1, \quad (5.14b)$$

taken from Robinson et al. [2014] the equation also follows a similar form to Equation 5.11, where  $\lambda_D$  is the Debye length for the plasma and  $L_s$  is specific for a hot electron moving through fully ionized material. The Debye length is given by,  $\lambda_D = \sqrt{\varepsilon_0 k_B T / n_e e^2}$ . Scattering due to free electrons can be ignored for most materials as it is small compared to the ion contribution, except in hydrogen; the last term in the square brackets accounts for hot electron - free electron scattering. There is no electron binding energy correction to scattering, since scattering from nuclei dominates. Equation 5.14 assumes that all materials the hot electrons interact with are fully ionized, which is not correct, especially in the cold fuel. For unionized material the only difference to Equation 5.14 is that the screening potential  $\lambda_D$  is changed to  $a$  the atomic radius. There is no equation given in Robinson et al. [2014] for partially ionized materials, but an approximation which relies on tabulated ion radii which is left for future work. The effect is small since the term is within a logarithm and during the late stages of an implosion (when hot electrons are emitted) even the cold fuel which is not fully ionized is at a temperature of several eV (see Figure 4.3 (b)) where  $\lambda_D \sim a$ .

Equation 5.14 is only true for multiple small scatterings, for the implementation described above this is dependent on mesh resolution and hot electron energy. The lower the hot electron energy, the greater the required mesh resolution to determine particle trajectory. However, at lower hot electron energies and lower mesh resolutions, deposition is more likely to be correct since the trajectory need not be as well-defined. Most low energy electrons stop within the first cell, making sub-cell



trajectory irrelevant in many cases. If a grid is well resolved in one direction but not in another, this may lead to significant scattering and deposition errors given the implementation.

To calculate the half cone angle from RMS angle we use,

$$\langle \theta^2 \rangle \approx \arccos \left( \frac{\cos \theta_{cone} + 1}{2} \right)^2, \quad (5.15)$$

which can be inverted algebraically and has a maximum error of 3% for angles  $\langle \theta^2 \rangle < \pi/2$  when compared to,

$$\langle \theta^2 \rangle = \frac{2\theta_{cone} \sin \theta_{cone} - (\theta_{cone}^2 - 2) \cos \theta_{cone} - 2}{1 - \cos \theta_{cone}} \quad (5.16)$$

the correct derivation for the RMS angle of a uniform cone. Equation 5.14 is only correct for multiple small scatterings, and the approximation is more accurate as  $\theta_{cone} \rightarrow 0$ . It is possible for  $\langle \theta^2 \rangle > \pi/2$  or even worse  $\langle \theta^2 \rangle > \pi$ , since the calculation has been used over large distances. To resolve this issue  $0 < \theta_{cone} < \pi$  is enforced (the upper limit corresponds to uniform scattering over a solid angle  $4\pi$ ).

Scattering is carried out over a solid angle relative to the electron's velocity vector. Unbiased 3D vector rotation from a random starting direction vector is non-trivial. The initial direction of the hot electron's velocity is described by angles  $\theta$  and  $\phi$  adhering to the physics convention; the scattering angle will be given by polar rotation  $0 < \alpha < \theta_{cone}$  and azimuthal rotation  $0 < \beta < 2\pi$  which can be distributed uniformly using two-pseudo random numbers and an algorithm described in Fong [2019]; Reynolds [2017]. The scattering rotation is done in 3 steps which were reduced in Maple (Maplesoft [2019]) before adding to the code. First the initial vector is rotated to align with  $(0, 0, 1)$  (in spherical polar coordinates using rotations  $\theta$  and  $\phi$ ), then the result is scattered by  $\alpha$  then  $\beta$ , finally the scattered vector is rotated back by  $\theta$  and  $\phi$ . The resulting vector is scattered by an angle  $\alpha$  from the initial vector, but about a random axis defined by  $\beta$ . The reduced form of the rotations is,

$$\begin{bmatrix} \cos(\phi) \cos(\theta) \cos(\beta) \sin(\alpha) - \sin(\beta) \sin(\phi) \sin(\alpha) + \cos(\phi) \sin(\theta) \cos(\alpha) \\ \sin(\phi) \cos(\theta) \cos(\beta) \sin(\alpha) + \cos(\phi) \sin(\beta) \sin(\alpha) + \sin(\phi) \sin(\theta) \cos(\alpha) \\ -\sin(\theta) \cos(\beta) \sin(\alpha) + \cos(\theta) \cos(\alpha) \end{bmatrix} \quad (5.17)$$

which can be tested in the limit of small scattering where  $\sin \alpha = \sin \beta = 0$  and  $\cos \alpha = \cos \beta = 1$  the initial vector direction is retrieved.

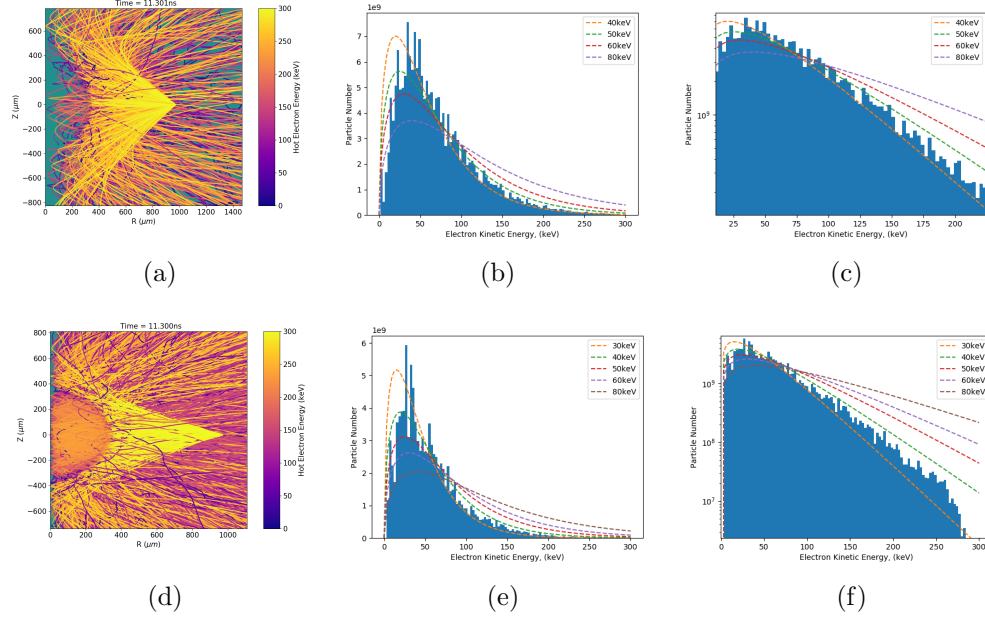


Figure 5.4: 40 keV thermal hot electron energy distribution for  $45^\circ$  (top) and  $27.5^\circ$  (bottom) half cone angle. The distribution was taken at the edge of the simulated domain which was  $\approx 10\text{mm}$  for this snapshot. Uniform sampling between 0 and 300 keV with 10,000 paths, each path is mono-energetic.

### 5.1.5 Reflux

This Thesis would like to acknowledge the theoretical guidance and references provided by Philip Bradford on the topic of hot electron reflux. Hot electrons travel along 3D paths until they deposit all their energy or leave the simulation domain. The amount of hot electrons leaving the domain depends on many factors. However it is clear that the domain will become charged if electrons leave at a faster rate than ions (assuming hydrogen ions). As the domain or target becomes charged there are three mechanisms restoring equilibrium, a return current through the experimental apparatus holding the target (stalk), outflow of ions, and the returning flow of hot electrons (reflux). The first of these mechanisms is described by Sinenian et al. [2013] for ICF relevant experiments, target discharging is expected to occur on a 1ns timescale. Ion (charged plasma) outflow is considered in 1D by Mora [2003] where reflux potential is related to the temperature of the escaping population. Hot electron reflux has been examined in several experiments varying from reduced models (Armstrong et al. [2019]) to more complete models (Poyé et al. [2015]), the former successfully applies a reflux model similar to the one presented below. Although there has been much work into the amount of refluxing that occurs the literature

is dominated by target normal sheath acceleration at regimes too high energy and short pulse to be relevant for this model. Wilks et al. [2001] shows that on short timescales (shorter than return current) the electric field  $E$  can be approximated by,

$$E \approx \frac{T_{hot}}{eL} \approx \frac{T_{hot}}{e\lambda_D} \quad (5.18)$$

where  $T_{hot}$  is a hot electron temperature and the plasma scale length  $L$  is approximated as the Debye length  $\lambda_D$ . Resulting in a potential barrier of size  $T_{hot}[\text{eV}] \sim V[\text{eV}]$ . Although for ICF and shock ignition the timescales considered are not short compared to the return current, the hot electron reflux approximation is added as a user option.

The reflux cut-off energy was thus selected as the temperature of the escape distribution seen in Figure 5.4. An approximation of  $T_{escape} = T_{initial} = E_{cutoff}$  was made, resulting in a reduced reflux model that can be applied to the Monte-Carlo particle tracker without fine-tuning by the user.

### 5.1.6 Future Work

During the description of the model several improvements were defined as future work. These include the improvement to: hot electron stopping increasing the range of validity of the density effect approximation (Equation 5.13), the scattering model assuming fully ionized background material, removal of instantaneous travel approximation, sub-cell scattering for hot electron paths and improvements to the reflux model to accurately capture electric potential. In addition to these, the model currently lacks electric and magnetic field creation and interaction.

### Electric and Magnetic Field Interactions

To summarise, the missing physics can be split into two sections: fields created by the fluid (background fields) that the hot electrons interact with and the fields created by the hot electrons. Odin has an MHD module, the fields created should modify the hot electron trajectories. The motion of hot electrons will also modify the electric and magnetic fields. The resistive heating created by the return current (approximated by Equation 5.10) is small compared with the hot electron heating, but can be added to improve the model. This is a coupled system with many interacting parts, and the physics is not limited to the phenomena listed here.

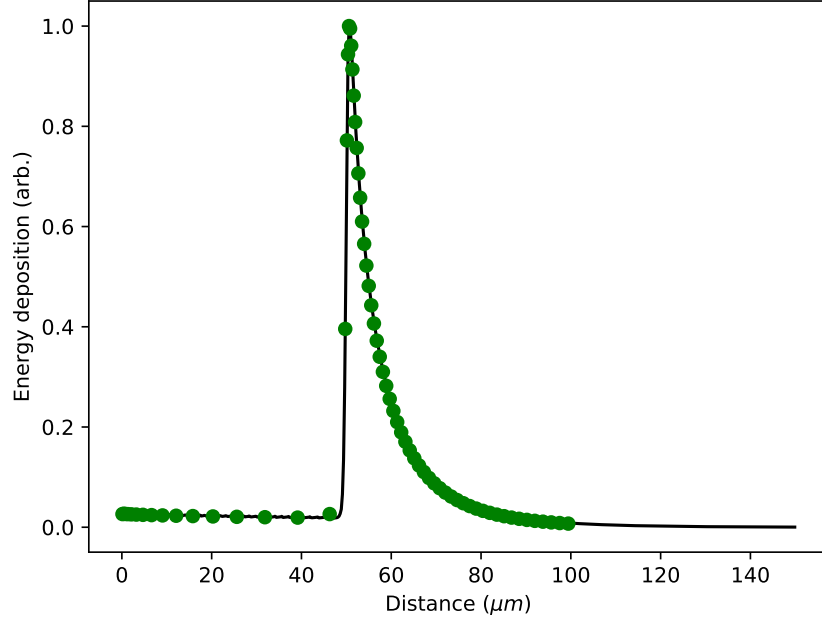


Figure 5.5: Direct comparison between Odin hot electron deposition (black line) to Fox [2014] (green dots) of 1D hot electron energy deposition for a Maxwellian beam at 30keV. The hot electron beam travels from a low density region,  $0.1\text{g/cm}^3$  on the left to a high density,  $10.0\text{g/cm}^3$  region on the right with the material boundary at  $50\mu\text{m}$ . The total energy deposition error compared to prior work was  $\mathbf{L_1} < 0.4\%$ .

## 5.2 Tests

The tests listed below aim to evaluate the correct implementation of hot electron energy deposition in Section 5.2.1 and scattering in Section 5.2.2. The work presented is original work for this Thesis.

### 5.2.1 Deposition Test

A simple 1D hot electron deposition test presented in Fox et al. [2013] and Fox [2014] but originally in Gus'kov et al. [2012]. Replication of the test can be seen in Figure 5.5. Hot electrons deposit energy into a dense slab of material, starting at  $50\mu\text{m}$  with low density plasma before. The test ensures hot electron transport through low density regions and accurate stopping. Energy deposition matches Fox [2014] to  $\mathbf{L_1} < 0.4\%$  (see Equation 3.29 for definition of  $\mathbf{L_p}$  Norms). This level of agreement for a Maxwellian distribution of hot electrons tests both the sampling and the deposition in Odin.

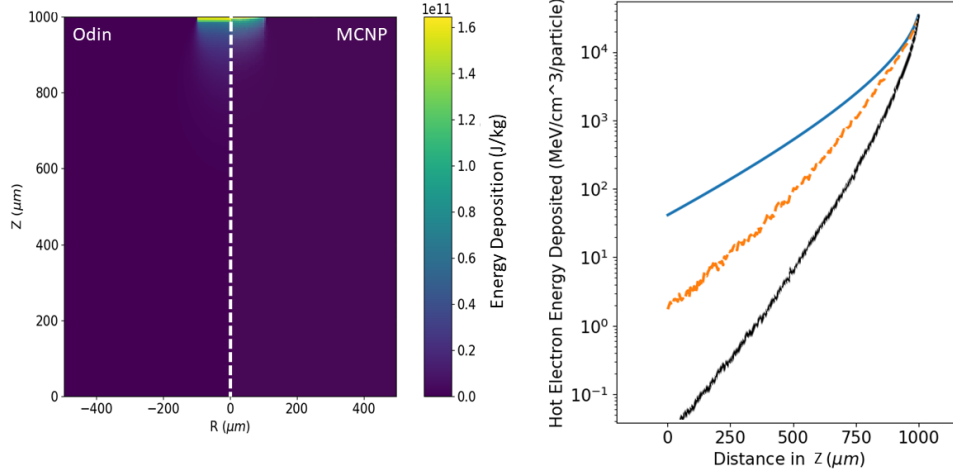


Figure 5.6: Code comparison to Werner et al. [2018]. (Left) Problem setup, a collimated electron beam with a thermal distribution of electrons at 40keV enters dense uniform material (ionized ideal gas hydrogen, at  $1\text{g}/\text{cm}^3$  and 7eV) centred on the point  $Z = 0, R = 0$  and a beam width of 200 microns (simulation grid was  $200 \times 200$  cells). (Right) Amount of energy deposited per source particle averaged radially, the black line is MCNP’s energy deposition (rescaled 30% so that deposition at  $1000\mu\text{m}$  is the same), the orange dashed line is Odin’s hot electron energy deposition with scattering, and the blue line is Odin’s hot electron deposition without scattering. There is a significant difference in the amount of hot electron dispersion that occurs, which is partially due to MCNP’s improved trajectory updating with sub-cell resolution.

### 5.2.2 MCNP Code Comparison: Scattering Test

Scattering is tested with a collimated hot electron beam with temperature 40keV hitting a uniform slab of material, shown in Figure 5.6. The hot electrons scatter and deposit energy across the slab. The rate at which energy deposition reduces in the  $Z$  direction tests the dispersion of hot electrons over distance travelled, and therefore the scattering routine. The comparison model from MCNP seen in Figure 5.6 relies on atomic scattering, whereas Odin assumes fully ionized background material, so the screening distance for nuclei is different. The screening distance for MCNP is the atomic radius  $a_0$  and for Odin is the Debye length  $\lambda_D$  (as seen in Equation 5.14b). At the point of overlap for the two models  $a_0 = \lambda_D(T)$  which can be used to find the temperature at which the fully-ionized and atomic scattering models should agree (see Equation 4.1). For  $\rho = 1\text{g}/\text{cm}^3$  hydrogen,  $n_e \approx 6.0 \times 10^{29}\text{m}^{-3}$

with an empirical atomic radius,  $a_0 \approx 25.0 \times 10^{-12}\text{m}$  the models should match at  $T \approx 7\text{eV}$  which was used as the temperature for these simulations. Figure 5.6 shows that exact agreement is not achieved, this could be due to two main factors; Odin's scattering and deposition is not as accurate as the routine seen in MCNP Werner et al. [2018] due to trajectory updates only occurring at mesh faces; and the approximation of the density effect (Sternheimer et al. [1984]) in Equation 5.11b which is most accurate for highly relativistic electrons and/or ionized material (see Section 5.1.3). The material in this simulation is not ionized nor are the hot electrons highly relativistic, which likely contributed to the disparity in energy deposition in Figure 5.6 (at  $Z = 1000\mu\text{m}$ ) which required rescaling of Odin's energy deposition by 30%.

Energy deposition was tested against published results in Section 5.2.1 which gave close agreement (error  $< 1\%$ ) for an ionized material. Future work for this project is to improve accuracy of the scattering and deposition formula used in Odin for unionized material. This involves the addition of an approximation of the density effect that has a wider range of validity than Equation 5.11b and a smooth transition between screening distances (atomic radius and Debye length) as charge state increase in Equation 5.14b (see Robinson et al. [2014]).

## Chapter 6

# NIF Solid Target Experiment

The National Ignition Facility (NIF, Miller et al. [2004]) is the largest laser facility in the world. It has not yet achieved ignition and although not designed to work in the same direct drive configuration as shock ignition (SI), there are simulations showing an alignment called polar direct drive (PDD) could be used to ignite a SI implosion (Anderson et al. [2013]). Scaled down SI experiments have shown that laser plasma instabilities (LPI) are a significant unknown not captured in the hydrodynamics, which can reduce laser drive and degrade implosion performance (Theobald et al. [2012]; Nora et al. [2015]). LPI lead to laser backscatter, and hot electron generation. The wasted drive energy that laser backscatter causes can be modelled effectively, however the impact of the hot electron population is less clear. Hot electrons are predicted to cause target preheat and reduce compression critical for ignition (Colaitis et al. [2016]; Rosenberg et al. [2018]; Radha et al. [2016]) but depending on the hot electron temperature, they also may lead to more efficient drive and stronger shocks (Betti et al. [2008]; Shang et al. [2017]).

Experimental characterization of a hot electron population in the  $10^{15} - 10^{16} \text{W/cm}^2$  intensity regime relevant to SI is presented in this chapter. The hot electron population was diagnosed in a PDD experiment at the NIF, using a solid plastic (CH) target rather than a hollow implosion capsule. The hot electron population was observed with a thermal distribution of energies at a temperature  $T_h = 56 \text{keV}$ , and a total population kinetic energy of 35kJ. The latter corresponding to an instantaneous laser energy conversion of 20% at the quarter critical surface ( $\eta_{qc} = 0.2$ , laser to hot electron energy fraction at  $n_{crit}/4$  or  $\eta = 0.043$ ) during the high intensity peak of the laser pulse shape. The solid target experiment was simulated using Odin and agreement with experimental diagnostics was achieved. The hot electron characteristics were then applied to a SI simulation to investigate the implosion's

susceptibility. This Thesis finds that hot electrons heat volumetrically beyond the ablation front and modify shock timing by changing energy transport. More than preheat or shock support, it is the depth the electrons penetrate and deposit their energy that effects shock timing. The modified energy transport and shock timings were observed in both the experimental simulation and the SI simulations. In addition, preheat and shock timing offset were detrimental to achieving ignition in the SI simulations, although some mitigation could be achieved with a delay of the SI spike in the laser pulse.

In Section 6.1 some context is given for why the experiment was done. Section 6.2 describes briefly the experiment, although more detail is found in the pre-print experimental paper, Anderson and Theobald [2021]. The next section (6.3), uses Odin to simulate the experiment and match experimental observations. Section 6.4 describes how the experimentally diagnosed hot electrons are applied to SI simulations, and the final section (6.5) analyses the simulations. This Thesis presents original work in the simulation presented below for analysis of the NIF strong shock solid target experiment (SSS). The use of experimental hot electron characterization being applied to SI simulations is also original work. The author would like to acknowledge the work of the experimentalists and collaborators Wolfgang Theobald and Ken Anderson alongside the experimental team at the National Ignition Laboratory. The work is being written for submission to Physics Review Letters.

## 6.1 Background

The National Ignition Facility (NIF) Miller et al. [2004] is investigating polar direct drive (PDD) inertial confinement fusion (ICF) to achieve more efficient coupling of laser energy to the target (Skupsky et al. [2004]; Collins et al. [2012]; Hohenberger et al. [2015]; Radha et al. [2016]). In direct drive ICF (Craxton et al. [2015]), laser ablation drives the capsule and the inertia of the capsule wall confines the implosion for the required nanosecond time-scale to achieve thermonuclear burn. Central hotspot ignition (Atzeni and Meyer-ter Vehn [2004]) relies on the capsule wall to carry the kinetic energy necessary to initiate isobaric ignition in the gas filled core. To create a burn wave in the colder capsule wall, an areal density of  $0.3\text{g}/\text{cm}^2$  must be achieved to reduce energy losses (Rosenberg et al. [2018]). The compressibility of the target is increased by cryogenically cooling it before the implosion and shocks are used to increase pressure and density near adiabatically. SI (Betti et al. [2007]; Theobald et al. [2008]; Ribeyre et al. [2008]; Perkins et al. [2009]) separates the assembly from the ignition phase with a late stage shock, leading to non-isobaric



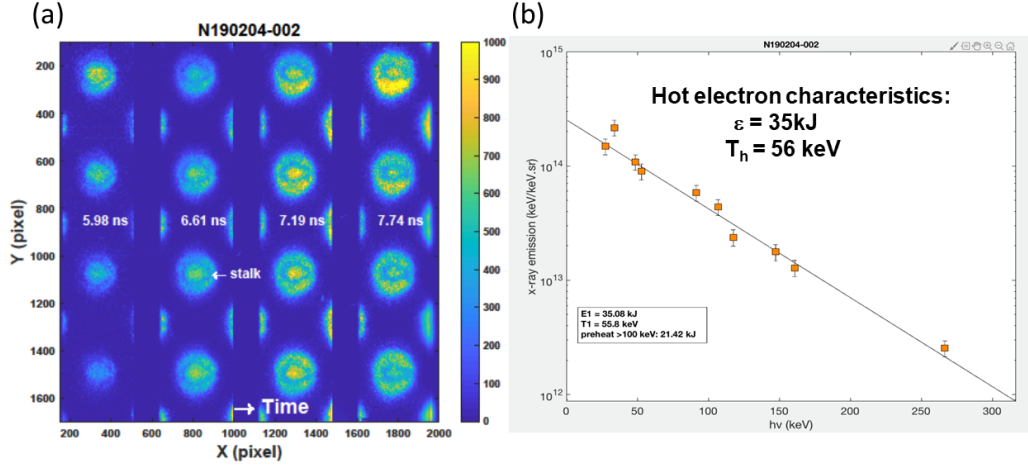


Figure 6.1: (a) GXD data showing the shock propagation. (b) FFLEX data showing x-ray bremsstrahlung temperature used to infer hot electron temperature ( $T_h = 56\text{keV}$ ) and total kinetic energy (35kJ) overlaid. National Ignition Facility (NIF) direct drive solid target strong shock (SSS) experiment N190204-002. Measurement of X-ray emission using the filter-fluorescer diagnostic system (FFLEX, McDonald et al. [2004], in the range 20 – 500keV). The peak intensity of the laser at quarter critical is  $I \sim 10^{16}\text{W/cm}^2$ .

hotspot ignition. The SI shock requires an increase in laser intensity above that used in the drive phase, often exceeding the  $10^{15}\text{W/cm}^2$  limit (Myatt et al. [2014]) where laser plasma instabilities are thought to dominate laser absorption. Sub-scale experiments and scaling simulations have been carried out (Palaniyappan et al. [2020]) however the physics of LPI depend on plasma density scale length and laser intensity making them scale dependant (Kruer [2019]; Rosenberg et al. [2018]).

LPI generate hot electrons that can penetrate the target and preheat material ahead of the shocks, reducing the compressibility and preventing ignition. Determining the hot electrons' temperature and laser energy fraction (Bell and Tzoufras [2011]; Gus'kov et al. [2012]; Batani et al. [2014]; Rosenberg et al. [2018]) determines whether they will cause harmful preheat (Nicolai et al. [2014]; Colaitis et al. [2016]) or be beneficial in shock creation (Betti et al. [2008]; Shang et al. [2017]). The balance of these factors rests on the characterization of the hot electron population.

From linear theory, stimulated Ramen scattering (SRS) (Liu et al. [1974]) and two plasmon decay (TPD) (Simon et al. [1983]) are expected to be the dominant LPI at this intensity. However, both particle-in-cell (Seaton and Arber [2020]) and experimental observation of backscatter light (Rosenberg et al. [2018]) indicate that SRS pump depletes other LPI and is responsible for the majority of hot electrons

generated. Simulation of LPI has been attempted in fluid codes (Colaitis et al. [2015, 2016]) however experimental observations currently lead theory in distinguishing the dominant LPI mechanisms, meaning there is benefit to reducing the LPI model and simulating the experimentally diagnosed hot electrons which are predicted to impact the implosion.

## 6.2 Simulation to Match NIF SSS Experiment

This Chapter presents the combination of nanosecond time-scale,  $10^{15} - 10^{16} \text{W/cm}^2$  intensity regime experimental characterization of hot electrons carried out on the NIF with a fluid simulation including an integrated 3D hot electron Monte-Carlo deposition and scattering model. Furthermore, we apply the hot electron characterization to near ignition scale implosions thought to be achievable with PDD on the NIF.

The hot electron characteristics used in this Chapter are based on diagnostics from a NIF direct drive strong shock solid target (SSS) experiment (N190204-002). The experiment featured a  $1100 \mu\text{m}$  plastic target, and a 800kJ laser pulse with peak intensity in excess of  $10^{15} \text{W/cm}^2$ . The aim of the experiment was to investigate the effect of hot electrons on the formation and propagation of spherically convergent strong shocks relevant for SI. Figure 6.1 shows droop corrected, gated x-ray detector data (GXD, Kyrala et al. [2010]) indicating shock position and filter-fluorescer diagnostic system (FFLEX, McDonald et al. [2004]) hot electron characterization (McDonald et al. [2004]).

The experiment was simulated using Odin, a 2D radiation-hydrodynamics ALE code, and its 3D Monte-Carlo hot electron tracking routines. The deposition and scattering routines are based on Robinson et al. [2014] (Seltzer and Berger [1984]; Atzeni et al. [2008]). The reduced laser and LPI model were used to generate hot electrons at quarter critical surface ( $n_{crit}/4$ ). Coronal physics was reduced with the aim of reproducing experimental observables, not the full physics of LPI and thus removing the largest unknown. In addition, the laser rays are modelled as simple radial paths that do not refract or diffract but deposit energy via inverse bremsstrahlung and idealized resonant absorption (depositing all remaining energy at critical density). These reductions allow input of experimental hot electron characteristics and the simplified driver makes the observation of their effect on the target and shock clear.

Hot electron angular distribution was not measured at the NIF SSS experiment and represents the largest unknown in this work. A uniform distribution over

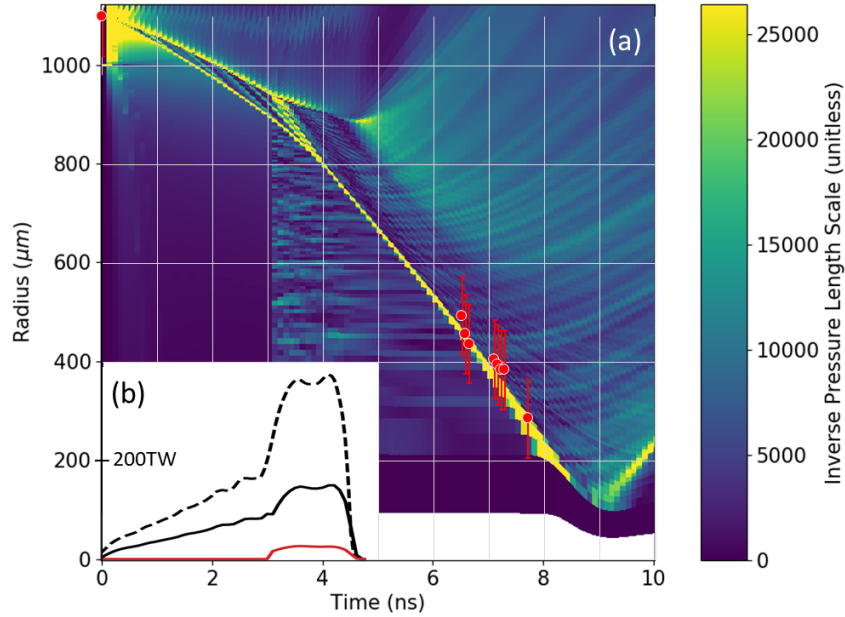


Figure 6.2: (a) Inverse pressure length scale ( $d(\ln P)/dr$ ) showing the shock propagation in the simulation and the red circles representing the shock timing extracted from Figure 6.1 with corresponding error bars. (b) Power emitted: dashed black is the experimental measure, solid black is the simulation after CBET and SRS backscatter and red solid is the hot electrons, equivalent to 35kJ.

a full cone angle of  $90^\circ$  was used. The value is in broad agreement with prior experiment and simulation seen in Yaakobi et al. [2013]; Colaitis et al. [2016]; Seaton and Arber [2020] however there is no consensus and for diffusive hot electrons an isotropic distribution was preferred in Betti et al. [2008]; Perkins et al. [2009]; Nora et al. [2015] or a  $180^\circ$  uniform distribution in Theobald et al. [2012] which did not feature scattering. The hot electron temperature was set at 55keV, and sampled with 200 energy bins per laser ray. The energy fraction taken from the laser at  $n_{crit}/4$  was 20% giving the 35kJ observed in Figure 6.1.

### 6.3 Analysis of NIF SSS simulation

Figure 6.2 shows the simulation and experimental shock timing. Close agreement was achieved with a flux limiter of 6%, a CBET backscatter multiplier of 40% loss and an SRS backscatter term of 20% at  $n_{crit}/4$  during the high intensity part of the laser profile matching the hot electron energy fraction. The free parameters are not uniquely constrained by the experiment, as an increase in shock pressure achieved by increasing the CBET multiplier can be offset by reducing the flux limiter and

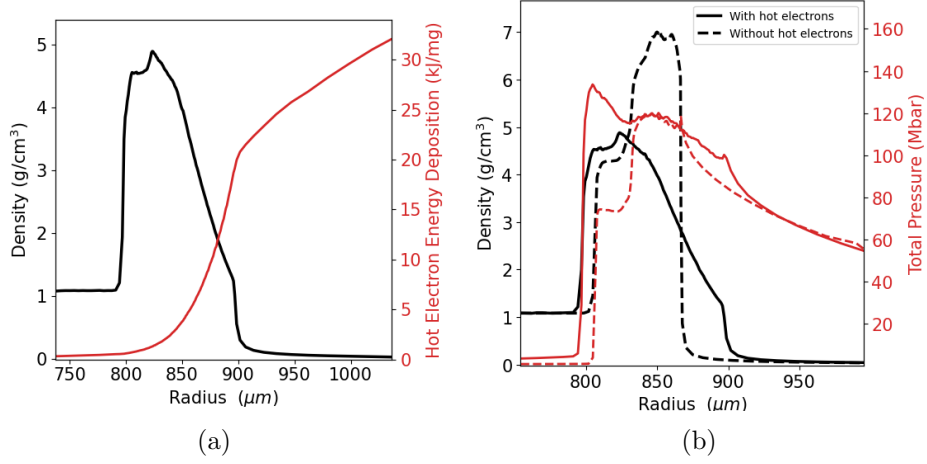


Figure 6.3: (a) Shows the density profile of the target in black and the hot electron deposition in red. The critical surface is at  $\approx 1050\mu\text{m}$ , the ablation front is at  $\approx 900\mu\text{m}$  but between  $850 - 900\mu\text{m}$  there is a hot electron pressure front. (b) Comparison of the density profile (black) and pressure profile (red) for simulations with (solid) and without (dashed) hot electrons. The change in shock timing is approximately equivalent to  $0.1\text{ns}$  at this point, but will be  $0.3\text{ns}$  by the time the two shock coalesce. After coalescence, the shock will travel at the same velocity (with the same pressure) as the simulation with hot electrons.

vice versa. The driver for the shock in this model is not accurate as the ray tracing has been simplified to a radial ray model but matching shock timing means that the radiation-hydrodynamics that occurs within the target should be representative of the experiment and so should the impact of the hot electrons. SRS is predicted to dominate over TPD when the intensity exceeds  $10^{15}\text{W}/\text{cm}^2$  (Seaton and Arber [2020]; Rosenberg et al. [2018]) and the FABS diagnostic used in the experiment reinforce the theory seen in PIC simulation Anderson and Theobald [2021].

From  $3\text{ns}$  onward in Figure 6.2, hot electron preheat is visible, and also in Figure 6.3, which are snapshots of the same simulation from  $4\text{ns}$ . Figure 6.3 (b) shows two shock fronts the second of which is created due to the increase in power at  $3\text{ns}$  but the second shock was not formed when hot electrons were simulated. Instead, hot electrons transfer their energy past the ablation front and support the existing shock pushing it ahead in time. When the two shock fronts have coalesced at  $5.7\text{ns}$  (at a radius of  $\approx 500\mu\text{m}$ ) there is a  $0.3\text{ns}$  timing difference between the shocks in the two simulations which is maintained until peak convergence (as the shocks have the same velocity and peak pressure). Due to the size of the error bars on the shock timing measurement (Figure 6.2) both simulations with and without hot electrons are compatible with the experimental diagnostics. There are two factors effecting

shock timing, hot electrons volumetrically applying pressure behind the shock front and preheating ahead. The hot electron temperature or sampling can be modified to remove preheat revealing that hot electron energy deposited behind the shock is responsible for the change in shock timing. Figure 6.3 (a) demonstrates that the majority of hot electron energy is deposited behind the shock front. Critically the simulations demonstrate that hot electrons deposit their energy over an area between the ablation front and shock front, volumetrically heating and supporting the shock, in addition they modify the density profile expanding the outer edge of the target. Hot electrons support the shock to the same total shock strength as simulations run without hot electrons (after they coalesce at 5.7ns), implying the change in shock timing is due to a modified energy transport mechanism not an increase in shock strength. If SRS backscatter is removed, the shock strength can exceed that of the simulation without hot electrons as described in Shang et al. [2017]. Shock support is more likely in a TPD dominated model (or where the hot electron beam size is narrow, and the hot electron temperature is low). The amount of support provided by hot electrons depends on the free parameter: angular distribution, which was not observed in the experiment. The narrower the emission angle the greater the shock size and the wider the angle, the less the effect of the hot electrons.

## 6.4 Shock Ignition Implosion Setup

The observations above are important for energy transport on nanosecond scales in the  $10^{15} - 10^{16} \text{W/cm}^2$  intensity regime. Specifically, the interaction of hot electrons with the shock front gives a unique insight into near ignition scale hot electron energy transport for SI (and electron shock ignition) which bears great relevance for PDD experiments on the NIF. The hot electron characterization is applied to a near ignition implosion, which is representative of what might be expected with NIF PDD.

The reduced ray and LPI model is used for the implosion as it is not intended to be predictive, however the result should make clear the importance of accurately modelling hot electrons in the  $10^{15} - 10^{16} \text{W/cm}^2$  intensity regime. The implosion target and laser profile, seen in Figure 4.2 were selected from Atzeni et al. [2019] for it's similarity to the NIF SSS experimental pulse shape. SI simulations here differ from Chapter 4.3 in the use of better resolution, radiation transport and a higher peak power of 300TW for the SI spike (not the 220TW seen in Figure 4.2). A large adiabat implosion ( $\alpha \sim 4$ ) was used as it is expected in PDD experiment to improve robustness to hydrodynamic instabilities (Tabak et al. [1990]). In addition, alpha

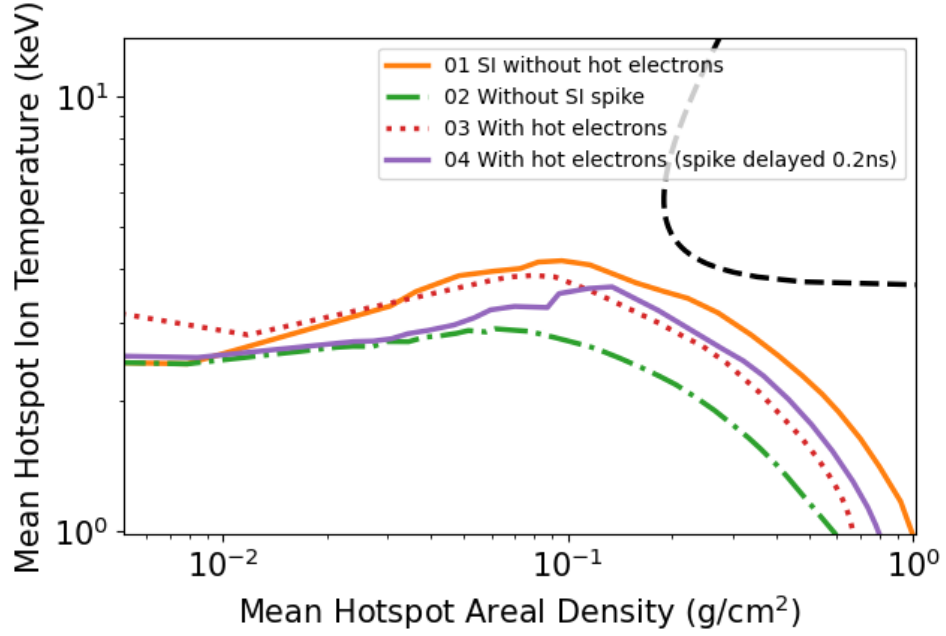


Figure 6.4: Hotspot thermodynamic path using the same hotspot definition as Ref. Colaïtis et al. [2016] (hotspot edge  $T_{edge} = T_i/10$  where  $T_i$  is the core temperature). The isobaric ignition criteria is displayed as a dashed black line. The simulation without hot electrons and without a SI spike lie at the extremum, with two simulations including hot electrons between. The difference is the timing of the shock ignition spike. We find the least degraded implosion requires a delay of 0.2ns on the shock ignition spike when compared to the optimal design without hot electrons.

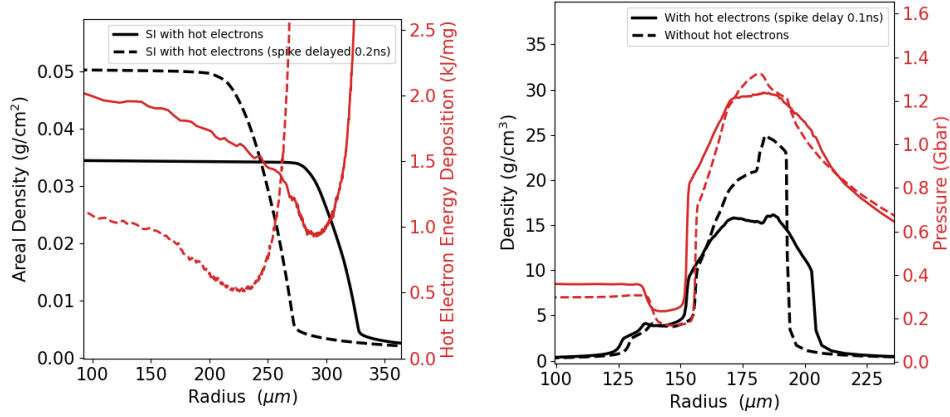


Figure 6.5: (a) The areal density (black) and cumulative hot electron energy deposition (red) of two simulations with hot electrons. The solid lines correspond to a simulation with a laser pulse shape optimized without hot electrons and the dashed line is the reduced preheat found by delaying the ignition pulse by 0.2ns. Both snapshots are taken 0.1ns into the shock pulse and are therefore 0.2ns offset. (b) Density (black) and pressure (red) achieving optimal shock timing for a simulation with (dashed) and without (solid) hot electrons. The shock timing offset is 0.1ns due to the volumetric heating of the hot electrons as seen in the NIF SSS experiment.

heating was not simulated to give a clean hotspot thermodynamic path (Figure 6.4). The hot electron characteristics were all the same as used for the NIF SSS simulation, however the shorter SI spike means that the 20% conversion efficiency at  $n_{crit}/4$  corresponds to a hot electron energy of  $\approx 15$ kJ. Due to the design aims of the NIF SSS and the similarity of the implosion pulse shape the hot electron characteristics are expected to be applicable. The most significant difference is the implosion's late stage convergence, meaning that plasma density scale length and beam overlap may lead to a difference in LPI.

## 6.5 Applying Hot Electron Characterisation to Shock Ignition

The hotspot thermodynamic paths of four simulations can be seen in Figure 6.4 at each extreme is a simulation without hot electrons (nearest ignition) and without a SI spike (furthest from ignition). Within the limits of the experimental characterization we found that hot electrons degrade SI implosions, the extent of the degradation depends on the angular distribution of the hot electron population and, critically for experimental design, the timing of the ignition spike. We found the least detrimental SI implosion with hot electron required a delay of 0.2ns for the SI

spike when compared to the optimal simulation without hot electrons.

The optimal delay for SI with hot electrons seen in Figure 6.4 is partially due to volumetric heating changing the shock timing as seen in the SSS NIF experiment. However, Figure 6.5 (a) demonstrates that a further increase in time delay is optimal to allow areal density to increase and reduce hot electron preheat. The inner shell preheat can be reduced from  $\approx 3\text{kJ/mg}$  to  $\approx 1\text{kJ/mg}$  (by the end of the shock pulse) using a delay of  $0.2\text{ns}$ . The improved laser pulse shape (with SI spike delay) corresponds to a preheat of  $\sim 0.3\text{kJ}$  or  $\sim 0.1\%$  of total laser energy which moves it within the acceptable limits as defined by Radha et al. [2016]; Rosenberg et al. [2018]. There are other ways to mitigate hot electron preheat which are not explored in this Thesis including, not ablating all of the plastic, or using a silicon layer to increase coronal temperature (Radha et al. [2016]).

Figure 6.5 (b) shows that optimal shock timing achieved can be reproduced with a SI spike delay of  $0.1\text{ns}$  when hot electrons are simulated. Volumetric heating is observed ahead of the ablation front at  $\approx 200\mu\text{m}$  (Figure 6.5 (b)) as was seen in the NIF SSS simulations. Increased target radius is observed again (as was seen for the NIF SSS in Figure 6.3 (b)), but critically for implosions it now affects in-flight aspect ratio (IFAR). Preheat is also visible beyond the capsule wall in the gaseous region at the centre as an increased pressure in Figure 6.5 (b) and an increased hotspot temperature in Figure 6.4.



## Chapter 7

# Omega Conical Target Experiment

Similar to Chapter 6, this chapter presents experimental observations aimed at characterizing shock ignition (SI) hot electron populations. The experiment described below was performed on the Omega laser (Laboratory for Laser Energetics, University of Rochester, Boehly et al. [1997], kilo-Joule class laser facility) not capable of delivering the Mega-joule energies thought necessary for ignition. Instead of replicating the target geometry (as seen in Chapter 6) a novel laser and target geometry was required to reach the plasma conditions seen in SI simulations, including a density scale length  $L_n \sim 500\mu\text{m}$  (Equation 4.11), coronal electron temperature  $T_e \sim 4\text{keV}$  and a laser intensity  $I > 10^{15}\text{W}/\text{cm}^2$ . The experiment was simulated on H2D (Larsen and Lane [1994b], by Kevin Glize and Robbie Scott Scott et al. [2021]) to verify the setup would reach the intended plasma conditions. It is the first time in published work that these plasma conditions have been achieved alongside hot electron characterization. The hot electron population was observed with  $T_h \approx 40\text{keV}$  temperature, and  $0.01 < \eta < 0.025$  of laser energy Scott et al. [2021].

Section 7.1 will outline the target and laser geometry used to achieve the plasma conditions. Section 7.2 describes the effect of the hot electron population on SI implosions, and the last section (7.3) will present a discussion of the disparity between the characterization in this chapter and that seen in Chapter 6. Original work for this Thesis is presented as the SI implosion simulations which were run to support the Omega conical shell experiment. The experimentalists and PIC theorists who contributed are listed in Scott et al. [2021].

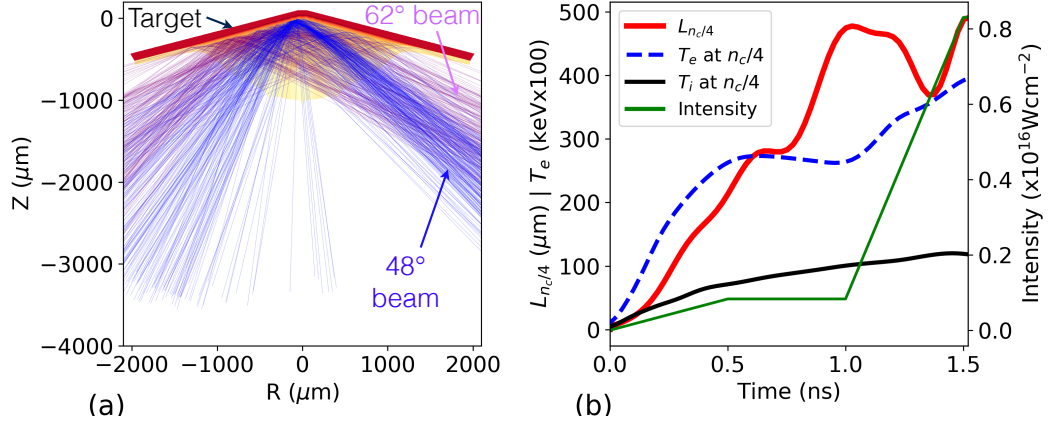


Figure 7.1: (a) Target setup with beam alignments. The target is a 3.6mm diameter cone with a full cone angle of  $152^\circ$ . The layered cone was  $40\mu\text{m}$  CH plastic on which the laser was incident, with a  $5\mu\text{m}$  copper layer and a  $30\mu\text{m}$  CH back. (b) Simulation of experiment done on H2D gives density scale length (red, solid), electron temperature (blue, dashed), ion temperature (black, solid) and intensity (green, solid, read from the right axis). This is the first published experiment to achieve SI plasma parameters seen in (b) at  $\approx 1.2\text{ns}$ . Reproduced from Scott et al. [2021].

## 7.1 Conical Target Experiment

The Omega conical target experiment is the closest published experiment to the plasma parameters and intensities expected in an ignition scale implosion. Moreover, the investigation has direct relevance to PDD SI on the 1.8MJ laser at the NIF as described by Anderson et al. [2013]. The aim was to achieve a density scale length  $L_n = \frac{dn_e}{dr}/n_e \approx 500\mu\text{m}$ , electron temperature  $\sim 4\text{keV}$  and laser intensities  $> 1 \times 10^{15} \text{ W/cm}^2$  on the kilo-joule class Omega. A spherical direct drive experiment on Omega can typically expect density scale length  $L_n \approx 125\mu\text{m}$ , electron temperature  $\sim 2\text{keV}$  and laser intensities  $< 1 \times 10^{14} \text{ W/cm}^2$ . As shown in Figure 7.1, the experiment used a novel conical target to improve laser coupling for the 20 beams available (in this geometry). 10 beams delivered 5kJ to the target creating the coronal plasma with the necessary parameters and then another 10 deliver 5kJ (focused at a point  $200\mu\text{m}$  from the initial target surface where the quarter critical surface was simulated to be) which creates the high intensities required.

Full aperture backscatter (FABS, not shown) diagnostics indicate that two plasmon decay (TPD) dominates until the high intensity beams are incident, at which point SRS is dominant. This is expected for an experiment that reaches the correct plasma parameters and intensities, as shown in Rosenberg et al. [2018]. The backscatter was also observed using a near backscatter imager (NBI) and filtering

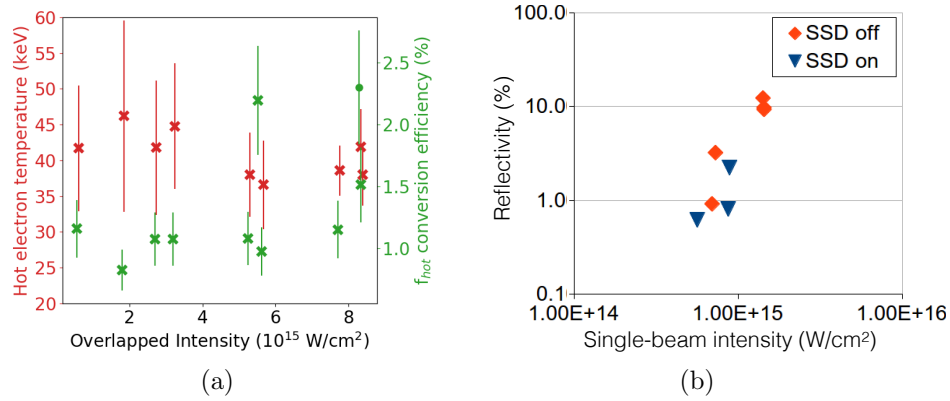


Figure 7.2: (a) Observed hot electron temperature (red, left axis) and laser to hot electron conversion efficiencies (green, right axis) for different intensity shots (bottom axis). Hot electron temperature shows little sensitivity to intensity and is consistently  $\approx 40$  keV. Hot electron fraction shows some sensitivity to intensity, however the trend is not clear and all are within 2 standard deviations of 1.5%. The use of imprint mitigating “smoothing by spectral dispersion” phase plates (SSD, Regan et al. [2000]) have no effect on hot electron characteristics. (b) The SRS reflectivity (backscatter) observed is affected by the use of SSD. The experiments done without the SSD (red, diamonds) show more backscatter,  $\sim 5\%$ , than those with the SSD,  $\sim 1\%$  (blue, dots). The mitigation of LPI with more spatially uniform lasers is one of the desired effects of SSD, so it is an expected result. The graph also shows a trend of increasing SRS backscatter with increasing intensity. Reproduced from Scott et al. [2021].

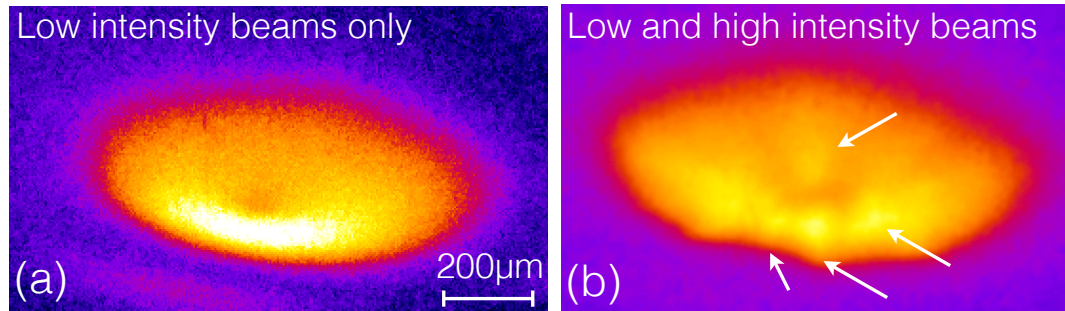


Figure 7.3: A spherically bent quartz crystal imager (SCI, Stoeckl et al. [2012]) was used to give spatially resolved images of high energy ( $\sim 8$  keV) hot electrons. (a) the low intensity beams show the most intense emission near the quarter critical surface where the beams are focused. (b) with the high intensity beams, the diagnostic shows intense patches with small structure. It is believed that hot electron emission cones from the non-uniform high intensity beams may cause the structures. Reproduced from Scott et al. [2021].

was used to distinguish SBS ( $\sim 351\text{nm}$ ) from SRS/TPD ( $400 - 700\text{nm}$ ).

The hot electron characterization was carried out by three diagnostics. Hot electrons incident on the copper layer (described in Figure 7.1) lead to line emission as a hot electron displaces a K-shell bound electron, the resulting relaxation leads to X-ray line emission ( $8.0478\text{keV}$ ) which is observed using the Zinc von Hamos spectrometer (ZVH, Jarrott et al. [2017], over the range  $8 - 9\text{keV}$ ) and a spherically bent quartz crystal imager (SCI, Stoeckl et al. [2012], over the narrow range  $8.045 - 8.054\text{keV}$ ) shown in Figure 7.3. These diagnostics were used to estimate energy fraction  $\eta$  using GEANT4 simulations (Agostinelli et al. [2003]) and a  $T_h = 40\text{keV}$  hot electron temperature. The temperature  $T_h$  was estimated from bremsstrahlung emission using a hard X-ray diagnostic (HXIP, Solodov et al. [2016b],  $10 - 200\text{keV}$ ).

Figure 7.2 shows the hot electron temperature  $\approx 40\text{keV}$ , and laser to hot electron energy conversion efficiency  $0.01 < \eta < 0.025$  generated during the experiment, it also shows the SRS backscatter  $\approx 1\%$  of incident laser light. When spatial smoothing by spectral dispersion (SSD, Regan et al. [2000]) is on. The near equivalence between SRS backscatter energy and hot electron energy is in agreement with PIC simulation (Seaton and Arber [2020]) and the approximation made in Equation 4.10. Calculation of the instantaneous fraction at the quarter critical surface requires accounting for the fact that only half the energy is in the high intensity pulse (half the energy is used to create the plasma) giving  $0.02 < \eta_{qc} < 0.05$ . This energy fraction is at the lower end predicted for SI LPI. The  $T_h = 40\text{keV}$  temperature is more central to the range given in Section 4.3.

In Figure 7.2 (a) there are fluctuations in both hot electron temperature and  $f_{hot}$  the conversion efficiency. With the amount of data and the uncertainty as given (by the error bars) the assumption is made in this Thesis that both temperature and conversion efficiency are constant across the range of intensities measured. This assumption differs from LPI theory, which predicts an increase in conversion efficiency and backscatter at  $I \approx 2 \times 10^{15}\text{W/cm}^2$  (Spencer et al. [2020]). The threshold may be visible as an upward trend of  $f_{hot}$  with higher intensities in Figure 7.2 (a) but there is not enough data to discern a definitive threshold.

Figure 7.3 shows possible direct observation of narrow beamed (non-isotropic) hot electron emission due to LPI. The small scale structures only arise when the high intensity beams are turned on and their intensity is correlated with SRS generated hot electrons observed. Their FWHM ( $\sim 75\mu\text{m}$ ) is smaller than the focus of the laser beams ( $105 \times 144\mu\text{m}$ ).

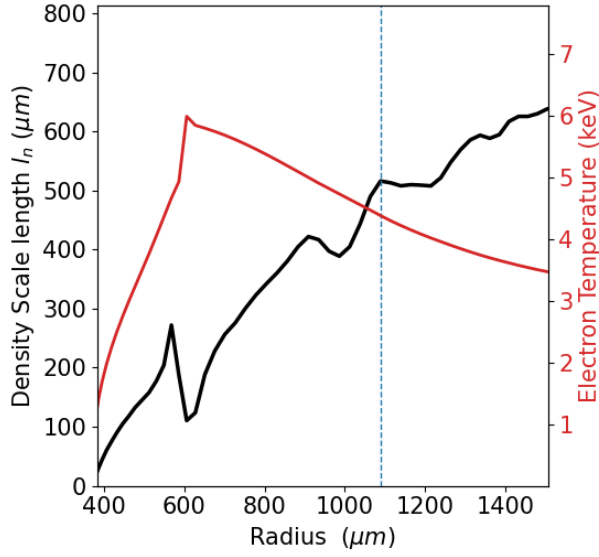
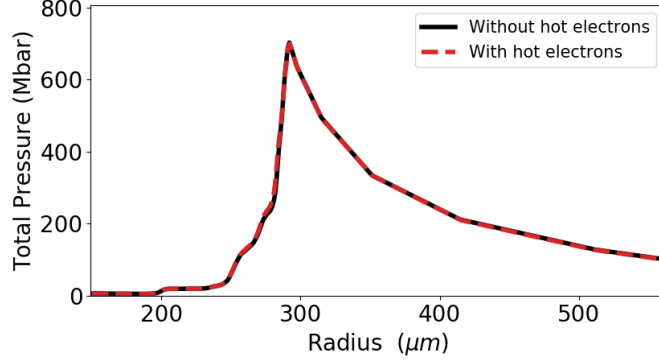


Figure 7.4: Shock ignition coronal plasma parameters. The quarter critical surface (blue, dashed) has density scale length  $\approx 500\mu\text{m}$  (black, left axis), electron temperature  $\approx 4\text{keV}$  (red, right axis) and peak laser intensity  $\approx 2 \times 10^{15}\text{W}/\text{cm}^2$  at quarter critical. This can be compared to the experimental measured parameters shown in Figure 7.1 (b).

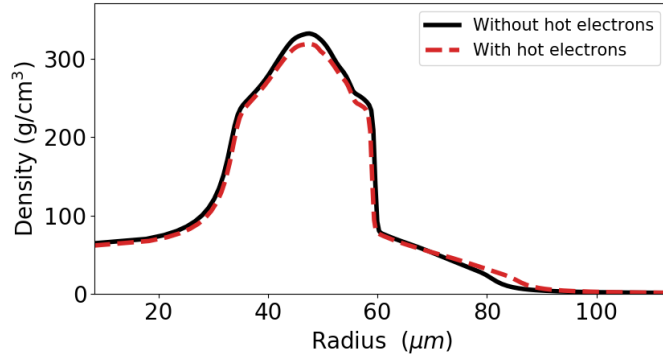
## 7.2 Shock Ignition Simulations

The hot electron characteristics observed can be applied to ignition scale simulations. The shock ignition setup is the same as described in Chapter 6 (and similar to Section 4.3 except for the use of better grid resolution, radiation transport and higher peak laser power of 300TW during the SI spike). The plasma parameters, seen in Figure 7.4, and the peak laser intensity,  $\approx 2 \times 10^{15}\text{W}/\text{cm}^2$  at quarter critical, were all a close match to those of the simulated omega conical target experiment (see Figure 7.1 (b)). The SI simulation peak intensity ( $\approx 2 \times 10^{15}\text{W}/\text{cm}^2$ ) is of closest match to  $\eta = 0.0125$  as read from Figure 7.2 ( $\eta_{qc} = 0.025$  at quarter critical).

The hot electron emission angle was not measured, but observation in Figure 7.3 indicate that the beams may have a narrow spread. The angular distribution was set as uniform over a  $90^\circ$  full angle in agreement with PIC simulation from Seaton and Arber [2020]. The observed hot electron temperature is  $\approx 40\text{keV}$  similar to the  $\approx 55\text{keV}$  used to match the diagnostics, from the NIF SSS (Chapter 6). However, in the Omega conical target experiment, the  $\approx 2 - 3\%$  ( $\eta_{qc} \approx 0.025$ ) of laser energy transferred to hot electrons at quarter critical is approximately  $\approx 8$  times less than observed in the NIF SSS ( $\eta_{qc} \approx 0.2$ ). Figure 7.5 shows that such a small energy fraction in hot electrons has almost no effect on the creation of the SI shock, and



(a)



(b)

Figure 7.5: Shock ignition implosion simulated without (black, solid) and with (red, dashed) a hot electron population being generated from the quarter critical surface during the shock ignition spike in laser power. The hot electron population is simulated with a temperature of 40keV, an energy fraction at quarter critical of 2.5%, and a full cone angle of  $90^\circ$ . Simulations are run without alpha particle heating, and the target and pulse shape are based on Atzeni et al. [2019]. (a) Pressure in the shock immediately after the laser pulse has ended, approximately at peak velocity. (b) Density at peak compression. Both (a) and (b) show that the hot electron population are having a negligible effect during the key phases of a shock ignition implosion. Reproduced from Scott et al. [2021].

hot electron preheat has only a minor effect at peak compression.

These hot electron characteristics do not pose an issue for SI and are well within tolerable levels of preheat for direct drive implosions. The novel experiment geometry presents an opportunity to explore ignition scale LPI on near future high repetition kilo-joule facilities, which will improve statistical significance of experimental observations.

### 7.3 Hot Electron Characterisation Disparity

The hot electron characterization presented in this chapter ( $\eta_{qc} = 0.025$ , and  $T_h = 45\text{keV}$ ) is in stark contrast with that presented in Chapter 6 ( $\eta_{qc} = 0.2$ , and  $T_h = 55\text{keV}$ ). The temperature fluctuations seen in Figure 7.2 give an error  $\approx \pm 10\text{keV}$  which indicates that the temperature measurements may be compatible, however the fraction of laser energy converted to hot electrons is not.

Values of  $\eta$  (see definition in Chapter 4.3) between the two experiments are closer, than  $\eta_{qc}$ , with NIF SSS  $\eta = 0.043$  and Omega conical target  $\eta = 0.0125$  for the intensities of interest for the SI setup ( $2 \times 10^{15}\text{W/cm}^2$ ). The larger difference seen in  $\eta_{qc}$  is due to target and beam geometry. The NIF SSS experimental simulation value for  $\eta_{qc}$  was modified until  $35\text{kJ}$  of hot electron energy was deposited within the target and ablated material for a laser pulse shape with the  $\times 0.6$  CBET multipliers applied. For the Omega conical target, the experimental setup was not simulated in Odin meaning that CBET multiplier could not be determined, and a direct extrapolation from experiment to implosion was necessary. CBET is expected to be less significant for conical and planar targets (Solodov et al. [2016a]). As a result, the  $\eta_{qc}$  fraction calculated for the experiment was applied directly to the SI simulation. Even when given as,  $\eta$  there is a disparity between the two experiments ( $> \times 3$  difference). There are several possible explanations detailed below.

The predictive capabilities of hydrodynamic simulations are limited, especially in the coronal region critical for these observations. It is possible that H2D simulations of the conical target are inaccurate and the conditions at the quarter critical surface differ from those shown in Figure 7.1. For the NIF SSS experiment shown in Chapter 6 the issue of predicting coronal physics is not as significant since the shock timing and electron characteristics were measured independently at the correct energy scales for SI. This means that the NIF SSS hot electron characterization can be applied directly to a NIF PDD SI implosion without the need for the same level of accuracy simulating coronal physics.

Assuming the simulated intensity, density scale length and background elec-

tron temperature of the two experiments are correct, there are factors which were not measured (including beam interaction angle, polarization and phase but also non-Maxwellian particle distributions) that affect LPI. It is possible that both experiments are relevant for SI experiments, and the Omega experimental parameters will give possible methods for hot electron suppression (such as a beam alignment). In order to understand physics on this scale, more kinetic simulations are required.

For PDD SI on the NIF the experimental setup shown in Chapter 6 (NIF SSS experiment) must be seen as the closest match to beam and target geometry. The beam and target geometry is critical to the type of LPI which occur (Ebrahim et al. [1980]). The major weakness of the Omega conical experiment is that it cannot achieve the SI geometry, intensity and plasma parameters. It is not clear whether this would lead to an over or under prediction of hot electron fraction due to the non-linear nature of the interactions. Another important distinction is that the density scale length is a radial parameter for implosions (assuming spherical symmetry) whereas the density changes, for the Omega experiment, in all three spatial dimensions. Experiments on kilo-joule facilities would be the best method for evaluating the sensitivity of these measurements to beam incident angle and the anisotropic density ramp.

The NIF SSS observation in Chapter 6 relies on the thick target approximation. The approximation assumes that most of the hot electron population is stopped by the target, emitting X-ray bremsstrahlung radiation with the same temperature as the hot electron that caused the emission (Hohenberger et al. [2013]). This means that the X-ray bremsstrahlung temperature seen in Figure 6.1 (b) can be used directly as the inferred hot electron temperature. The thick target approximation appears to be valid as the NIF SSS simulations show that that all hot electrons incident on the target (less than the 300keV cut-off) were stopped by the solid plastic sphere. Figure 5.1 shows hot electron trajectories for interaction with the NIF SSS target. The observation of the Omega conical target in this chapter, could not make the same thick target approximation (since its target was too thin) so instead GEANT4 (Agostinelli et al. [2003]) simulations were used to model hot electron stopping and diagnostic response (Stoeckl and Solodov [2019]). Both observation methods are susceptible to inaccuracies depending on the hot electron beam size, which has not been tightly constrained. If the beam is larger than the target, then hot electron refluxing becomes critical (see Section 5.1.5) which on the nanosecond timescales of the experiments is also in need of more experimental verification. The Omega conical target observation could be improved by repetition with a thicker target, as seen in Zhang et al. [2020], to verify the measurements.



The NIF SSS observation could be improved with more independent observations of X-ray emission (similar to the triple observation HXIP, ZVH, and SCI used with the Omega conical target). Hot electron beam size and refluxing are significant unknowns, which may have compounded with the difference in target geometry to cause the disparity in hot electron characterization. More experimental observation is needed of hot electron beam size and refluxing in the regime relevant to SI.

Finally, if a Mega-joule direct drive facility were constructed, it would have a different beam arrangement to those seen at the NIF. The hot electron characteristics shown in Chapter 6 may be relevant for PDD SI on the NIF but with reduced beam overlap a Mega-joule direct drive facility may observe different hot electron characteristics.

In summary, the observations and simulations described in this chapter and Chapter 6 mark a first step to understanding experimental observation of hot electron generation at SI intensities. Hot electron energy fraction and beam angle need to be constrained before predictive SI simulations can be run, however the susceptibility of the implosion to diagnosed populations has been explored. For the populations investigated, hot electrons have a deleterious effect on achieving ignition. The magnitude of mitigation depends on more experimental characterization, but neither of the populations made SI an untenable approach to ignition (mitigating strategies could be implemented to reduce preheat and/or re-time shocks).

## Chapter 8

# Conclusion

The computational aim of this project was to develop the energy transport routines used in the radiation-hydrodynamics ALE code Odin. The scientific goal of the project was to begin investigating the role of electron energy transport in shock ignition implosions. This Thesis presents the development of two core modules, in addition to simulations of a NIF experiment to characterize the hot electron population and the impact it would have on shock ignition. The Omega conical target experiment aims to achieve the same conditions, but the two observations present a significant contrast in hot electron characteristics.

The thermal conduction module was presented in Chapter 3 in addition to developing the code, it was tested and supplementary modules such as the radial ray tracing package and the cold (“quiet”) start function were written to allow Odin to run ignition scale simulations. The tests and ignition simulations all demonstrate the functioning of the module. Electron and ion thermal conduction were added as original work in this Thesis, furthermore the routines developed were also applied to radiation diffusion. Future work for this module is needed to improve accuracy in the proximity of contact discontinuities, mixed material cells, near steep temperature gradients and strong magnetic fields.

The hot electron module was presented in Chapter 5 with the sampling and deposition tested to agree with literature. The scattering of hot electrons, although functioning, has not finished testing due to the inadequate comparison. The scattering test shows some agreement, but differences may be in part explained by the simplified tracking routine. To fully diagnose the scattering of hot electrons, an ionized comparison model is required. 3D Monte-Carlo hot electron tracing with deposition and scattering in a radiation-hydrodynamics code is work not seen in the literature. The nearest comparison being Colaïtis et al. [2015] which uses beamlet

instead of particle tracking. Future work for the path tracing module include a ray tracing and alpha particle tracking. The hot electron module could be improved by the addition of the atomic corrections (including binding energies), modelling return currents and magnetic fields generated by the particles.

Chapter 6, uses hot electrons characterized by a nanosecond,  $10^{15} - 10^{16} \text{W/cm}^2$  intensity NIF experiment (SRS dominated, 55keV and 35kJ cumulative kinetic energy) to investigate the energy transport and preheat mechanisms. In this regime hot electrons preheat ahead of shocks but they also volumetrically heat and can support existing shocks. Shock timing is modified, even if shock strength and preheat are unchanged, since hot electrons deposit energy beyond the ablation front. The latter of which is not seen in the literature, as shock timing was attributed to preheat (Colaitis et al. [2016]) or support of shocks (Shang et al. [2017]). When the hot electron characteristics are applied to Megajoule scale implosions we find that they are degraded by preheat, the shock timing is modified but can be corrected with a SI spike delay. In addition, preheat appears to reach the maximum tolerable amount of 3kJ/mg seen in the literature (Rosenberg et al. [2018]), and needs to be mitigated either via further delaying the SI spike allowing areal density to increase or via other methods to maximize the potential for ignition.

The laser to hot electron conversion efficiency at quarter critical seen in Chapter 7  $\approx 2.5\%$ , contradicts that presented in Chapter 6 which was  $\approx 20\%$ . The two experiments aim to achieve the same plasma parameters and laser intensities, however they vary drastically in experimental setup. The difference in observation indicates that there needs to be more experimental observations in this regime. Neither experiment was able to quantify hot electron cone angle, however Scott et al. [2021] does present experimental observation indicating tight beams. Hot electron angular distribution is a free parameter that needs to be further constrained by experiment.

# Bibliography

- I Aavatsmark. An introduction to multipoint flux approximations for quadrilateral grids. *Computational Geosciences*, 6(3-4):405–432, 2002.
- Sea Agostinelli, John Allison, K al Amako, John Apostolakis, H Araujo, P Arce, M Asai, D Axen, S Banerjee, G 2 Barrand, et al. Geant4a simulation toolkit. *Nuclear instruments and methods in physics research section A: Accelerators, Spectrometers, Detectors and Associated Equipment*, 506(3):250–303, 2003.
- K. Anderson and W. Theobald. Nif sss experiment and analysis. (unpublished), 2021.
- KS Anderson, R Betti, PW McKenty, TJB Collins, M Hohenberger, W Theobald, RS Craxton, JA Delettrez, M Lafon, JA Marozas, et al. A polar-drive shock-ignition design for the national ignition facility. *Physics of Plasmas*, 20(5):056312, 2013.
- CD Armstrong, CM Brenner, E Zemaityte, GG Scott, DR Rusby, G Liao, H Liu, Y Li, Z Zhang, Y Zhang, et al. Bremsstrahlung emission profile from intense laser-solid interactions as a function of laser focal spot size. *Plasma Physics and Controlled Fusion*, 61(3):034001, 2019.
- S Atzeni, A Schiavi, and JR Davies. Stopping and scattering of relativistic electron beams in dense plasmas and requirements for fast ignition. *plasma physics and controlled fusion*, 51(1):015016, 2008.
- Stefano Atzeni and Jürgen Meyer-ter Vehn. *The Physics of Inertial Fusion: Beam-Plasma Interaction, Hydrodynamics, Hot Dense Matter*, volume 125. Oxford University Press on Demand, 2004.
- Stefano Atzeni, Angelo Schiavi, Luca Antonelli, and Arianna Serpi. Hydrodynamic studies of high gain shock ignition targets: effect of low-to intermediate-mode asymmetries. *The European Physical Journal D*, 73(11):1–10, 2019.

- Satish Balay, Shrirang Abhyankar, Mark F. Adams, Jed Brown, Peter Brune, Kris Buschelman, Lisandro Dalcin, Alp Dener, Victor Eijkhout, William D. Gropp, Dinesh Kaushik, Matthew G. Knepley, Dave A. May, Lois Curfman McInnes, Richard Tran Mills, Todd Munson, Karl Rupp, Patrick Sanan, Barry F. Smith, Stefano Zampini, Hong Zhang, and Hong Zhang. PETSc users manual. Technical Report ANL-95/11 - Revision 3.10, Argonne National Laboratory, 2018. URL <http://www.mcs.anl.gov/petsc>.
- MM Basko, J Maruhn, and An Tauschwitz. An efficient cell-centered diffusion scheme for quadrilateral grids. *Journal of Computational Physics*, 228(6):2175–2193, 2009.
- D Batani, S Baton, A Casner, S Depierreux, M Hohenberger, O Klimo, M Koenig, C Labaune, X Ribeyre, C Rousseaux, et al. Physics issues for shock ignition. *Nuclear Fusion*, 54(5):054009, 2014.
- AR Bell and M Tzoufras. Electron transport and shock ignition. *Plasma Physics and Controlled Fusion*, 53(4):045010, 2011.
- AR Bell, RG Evans, and DJ Nicholas. Electron energy transport in steep temperature gradients in laser-produced plasmas. *Physical Review Letters*, 46(4):243, 1981.
- AR Bell, APL Robinson, M Sherlock, RJ Kingham, and W Rozmus. Fast electron transport in laser-produced plasmas and the kalos code for solution of the vlasov–fokker–planck equation. *Plasma Physics and controlled fusion*, 48(3):R37, 2006.
- Keith Bennett, Tom Goffrey, and Tony Arber. User manual for the odin code, 2021. Accessed: 2021-06-06.
- David J Benson. Computational methods in lagrangian and eulerian hydrocodes. *Computer methods in Applied mechanics and Engineering*, 99(2-3):235–394, 1992.
- R Betti, CD Zhou, KS Anderson, LJ Perkins, W Theobald, and AA Solodov. Shock ignition of thermonuclear fuel with high areal density. *Physical review letters*, 98(15):155001, 2007.
- R Betti, W Theobald, CD Zhou, KS Anderson, PW McKenty, S Skupsky, D Shvarts, VN Goncharov, JA Delettrez, PB Radha, et al. Shock ignition of thermonuclear fuel with high areal densities. In *Journal of Physics: Conference Series*, volume 112, page 022024. IOP Publishing, 2008.

- TR Boehly, DL Brown, RS Craxton, RL Keck, JP Knauer, JH Kelly, TJ Kessler, SA Kumpan, SJ Loucks, SA Letzring, et al. Initial performance results of the omega laser system. *Optics communications*, 133(1-6):495–506, 1997.
- Th Bornath, M Schlenges, P Hilse, and D Kremp. Nonlinear collisional absorption in dense laser plasmas. *Physical Review E*, 64(2):026414, 2001.
- SI Braginskii. Transport processes in a plasma. *Reviews of plasma physics*, 1:205, 1965.
- J Breil and PH Maire. A cell-centered diffusion scheme on two-dimensional unstructured meshes. *Journal of Computational Physics*, 224(2):785–823, 2007.
- Edward J Caramana, Mikhail J Shashkov, and Paul P Whalen. Formulations of artificial viscosity for multi-dimensional shock wave computations. *Journal of Computational Physics*, 144(1):70–97, 1998a.
- EJ Caramana, DE Burton, MJ Shashkov, and PP Whalen. The construction of compatible hydrodynamics algorithms utilizing conservation of total energy. *Journal of Computational Physics*, 146(1):227–262, 1998b.
- A Colaïtis, G Duchateau, X Ribeyre, Y Maheut, G Boutoux, L Antonelli, Ph Nicolaï, D Batani, and V Tikhonchuk. Coupled hydrodynamic model for laser-plasma interaction and hot electron generation. *Physical Review E*, 92(4):041101, 2015.
- A Colaïtis, X Ribeyre, E Le Bel, G Duchateau, Ph Nicolaï, and V Tikhonchuk. Influence of laser induced hot electrons on the threshold for shock ignition of fusion reactions. *Physics of Plasmas*, 23(7):072703, 2016.
- TJB Collins, JA Marozas, KS Anderson, R Betti, RS Craxton, JA Delettrez, VN Goncharov, DR Harding, FJ Marshall, RL McCrory, et al. A polar-drive–ignition design for the national ignition facility. *Physics of Plasmas*, 19(5):056308, 2012.
- Jeff Colvin and Jon Larsen. *Extreme physics: properties and behavior of matter at extreme conditions*. Cambridge University Press, 2013.
- RS Craxton, KS Anderson, TR Boehly, VN Goncharov, DR Harding, JP Knauer, RL McCrory, PW McKenty, DD Meyerhofer, JF Myatt, et al. Direct-drive inertial confinement fusion: A review. *Physics of Plasmas*, 22(11):110501, 2015.
- JR Davies. How wrong is collisional monte carlo modeling of fast electron transport in high-intensity laser-solid interactions? *Physical Review E*, 65(2):026407, 2002.

- TR Dittrich, OA Hurricane, DA Callahan, EL Dewald, T Döppner, DE Hinkel, LF Berzak Hopkins, S Le Pape, T Ma, JL Milovich, et al. Design of a high-foot high-adiabat icf capsule for the national ignition facility. *Physical review letters*, 112(5):055002, 2014.
- R Paul Drake. *High-energy-density physics: fundamentals, inertial fusion, and experimental astrophysics*. Springer Science & Business Media, 2006.
- Dstrozzi. Nuclear fusion cross-sections, fusion rxnrate.svg. <https://commons.wikimedia.org>, 2020. Accessed: 2021-05-06.
- NA Ebrahim, HA Baldis, C Joshi, and R Benesch. Hot electron generation by the two-plasmon decay instability in the laser-plasma interaction at 10.6  $\mu\text{m}$ . *Physical Review Letters*, 45(14):1179, 1980.
- EM Epperlein and MG Haines. Plasma transport coefficients in a magnetic field by direct numerical solution of the fokker-planck equation. *The Physics of fluids*, 29(4):1029–1041, 1986.
- Robert D Falgout and Ulrike Meier Yang. hypre: A library of high performance preconditioners. In *International Conference on Computational Science*, pages 632–641. Springer, 2002.
- Enrico Fermi. The ionization loss of energy in gases and in condensed materials. *Physical Review*, 57(6):485, 1940.
- Noel Fleurot, Claude Cavailler, and JL Bourgade. The laser megajoule (lmj) project dedicated to inertial confinement fusion: Development and construction status. *Fusion Engineering and design*, 74(1-4):147–154, 2005.
- Chamberlain Fong. Analytical methods for squaring the disc, 2019.
- TE Fox, APL Robinson, and J Pasley. Strong shock generation by fast electron energy deposition. *Physics of Plasmas*, 20(12):122707, 2013.
- Thomas Edward Fox. *Strong shock wave generation by fast electron energy deposition in shock ignition relevant plasmas*. PhD thesis, University of York, 2014.
- GS Fraley, EJ Linnebur, RJ Mason, and RL Morse. Thermonuclear burn characteristics of compressed deuterium-tritium microspheres. *The Physics of Fluids*, 17(2):474–489, 1974.

- Thomas Goffrey. *A cylindrical magnetohydrodynamic arbitrary Lagrangian Eulerian code*. PhD thesis, University of Warwick, 2014.
- VN Goncharov, JP Knauer, PW McKenty, PB Radha, TC Sangster, S Skupsky, R Betti, RL McCrory, and DD Meyerhofer. Improved performance of direct-drive inertial confinement fusion target designs with adiabat shaping using an intensity picket. *Physics of Plasmas*, 10(5):1906–1918, 2003.
- ER Grilly. The vapor pressures of hydrogen, deuterium and tritium up to three atmospheres<sup>1</sup>. *Journal of the American Chemical Society*, 73(2):843–846, 1951.
- G Guderley. Powerful spherical and cylindrical compression shocks in the neighbourhood of the centre and of the cylinder axis. *Luftfahrtforschung*, 19:302–312, 1942.
- S Gus’kov, X Ribeyre, M Touati, J-L Feugeas, Ph Nicolaï, and V Tikhonchuk. Ablation pressure driven by an energetic electron beam in a dense plasma. *Physical review letters*, 109(25):255004, 2012.
- M Hohenberger, NE Palmer, G LaCaille, EL Dewald, L Divol, EJ Bond, T Döppner, JJ Lee, RL Kauffman, JD Salmonson, et al. Measuring the hot-electron population using time-resolved hard x-ray detectors on the nif. In *Target Diagnostics Physics and Engineering for Inertial Confinement Fusion II*, volume 8850, page 88500F. International Society for Optics and Photonics, 2013.
- M Hohenberger, PB Radha, JF Myatt, S LePape, JA Marozas, FJ Marshall, DT Michel, SP Regan, W Seka, A Shvydky, et al. Polar-direct-drive experiments on the national ignition facility. *Physics of Plasmas*, 22(5):056308, 2015.
- LC Jarrott, MS Wei, C McGuffey, FN Beg, PM Nilson, C Sorce, C Stoeckl, W Theobald, H Sawada, RB Stephens, et al. Calibration and characterization of a highly efficient spectrometer in von hamos geometry for 7-10 keV x-rays. *Review of Scientific Instruments*, 88(4):043110, 2017.
- David S Kershaw. Differencing of the diffusion equation in lagrangian hydrodynamic codes. *Journal of Computational Physics*, 39(2):375–395, 1981.
- RA Klausen and TF Russell. Relationships among some locally conservative discretization methods which handle discontinuous coefficients. *Computational Geosciences*, 8(4):341–377, 2004.



- O Klimo, S Weber, VT Tikhonchuk, and J Limpouch. Particle-in-cell simulations of laser-plasma interaction for the shock ignition scenario. *Plasma Physics and Controlled Fusion*, 52(5):055013, 2010.
- William Kruer. *The physics of laser plasma interactions*. CRC Press, 2019.
- W. Kutta. *Beitrag zur näherungsweise Integration totaler Differentialgleichungen*. Teubner, 1901. URL <https://books.google.co.uk/books?id=K5e6kQEACAAJ>.
- GA Kyrala, S Dixit, S Glenzer, D Kalantar, D Bradley, N Izumi, N Meezan, OL Landen, D Callahan, SV Weber, et al. Measuring symmetry of implosions in cryogenic hohlraums at the nif using gated x-ray detectors. *Review of Scientific Instruments*, 81(10):10E316, 2010.
- Jon T. Larsen and Stephen M. Lane. Hyadesa plasma hydrodynamics code for dense plasma studies. *Journal of Quantitative Spectroscopy and Radiative Transfer*, 51(1):179–186, 1994a. ISSN 0022-4073. doi: [https://doi.org/10.1016/0022-4073\(94\)90078-7](https://doi.org/10.1016/0022-4073(94)90078-7). URL <https://www.sciencedirect.com/science/article/pii/0022407394900787>. Special Issue Radiative Properties of Hot Dense Matter.
- Jon T Larsen and Stephen M Lane. Hyadesa plasma hydrodynamics code for dense plasma studies. *Journal of Quantitative Spectroscopy and Radiative Transfer*, 51(1-2):179–186, 1994b.
- JD Lindl and WC Mead. Two-dimensional simulation of fluid instability in laser-fusion pellets. *Physical Review Letters*, 34(20):1273, 1975.
- Konstantin Lipnikov, Gianmarco Manzini, and Daniil Svyatskiy. Analysis of the monotonicity conditions in the mimetic finite difference method for elliptic problems. *Journal of Computational Physics*, 230(7):2620–2642, 2011.
- CS Liu, Marshall N Rosenbluth, and Roscoe B White. Raman and brillouin scattering of electromagnetic waves in inhomogeneous plasmas. *The Physics of Fluids*, 17(6):1211–1219, 1974.
- RC Malone, RL McCrory, and RL Morse. Indications of strongly flux-limited electron thermal conduction in laser-target experiments. *Physical Review Letters*, 34(12):721, 1975.
- Wallace Manheimer, Denis Colombant, and Valeri Goncharov. The development of a krook model for nonlocal transport in laser produced plasmas. i. basic theory. *Physics of Plasmas*, 15(8):083103, 2008.

- a division of Waterloo Maple Inc.. Maplesoft. Maple, 2019. URL <https://hadoop.apache.org>.
- Jerrold E Marsden and Anthony Tromba. *Vector calculus*. Macmillan, 2003.
- JW McDonald, RL Kauffman, JR Celeste, MA Rhodes, FD Lee, LJ Suter, AP Lee, JM Foster, and G Slark. A filter-fluorescer diagnostic system (fflex) for the national ignition facility (nif). Technical report, Lawrence Livermore National Lab., 2004.
- Chad D Meyer, Dinshaw S Balsara, and Tariq D Aslam. A second-order accurate super timestepping formulation for anisotropic thermal conduction. *Monthly Notices of the Royal Astronomical Society*, 422(3):2102–2115, 2012.
- Chad D Meyer, Dinshaw S Balsara, and Tariq D Aslam. A stabilized runge–kutta–legendre method for explicit super-time-stepping of parabolic and mixed equations. *Journal of Computational Physics*, 257:594–626, 2014.
- Jürgen Meyer-ter Vehn and Christian Schalk. Selfsimilar spherical compression waves in gas dynamics. *Zeitschrift für Naturforschung A*, 37(8):954–970, 1982.
- Dimitri Mihalas and Barbara Weibel Mihalas. *Foundations of radiation hydrodynamics*. Courier Corporation, 2013.
- George H Miller, Edward I Moses, and Craig R Wuest. The national ignition facility. *Optical Engineering*, 43(12):2841–2853, 2004.
- Patrick Mora. Plasma expansion into a vacuum. *Physical Review Letters*, 90(18):185002, 2003.
- JE Morel, RM Roberts, and MJ Shashkov. A local support-operators diffusion discretization scheme for quadrilateral meshes. *Journal of Computational Physics*, 144(1):17–51, 1998.
- JF Myatt, J Zhang, RW Short, AV Maximov, W Seka, DH Froula, DH Edgell, DT Michel, IV Igumenshchev, DE Hinkel, et al. Multiple-beam laser–plasma interactions in inertial confinement fusion. *Physics of Plasmas*, 21(5):055501, 2014.
- Ph Nicolaï, J-L Feugeas, M Touati, X Ribeyre, S Gus’kov, and V Tikhonchuk. Deleterious effects of nonthermal electrons in shock ignition concept. *Physical Review E*, 89(3):033107, 2014.

- R Nora, W Theobald, R Betti, FJ Marshall, DT Michel, W Seka, B Yaakobi, M Lafon, C Stoeckl, J Delettrez, et al. Gigabar spherical shock generation on the omega laser. *Physical review letters*, 114(4):045001, 2015.
- Jan M Nordbotten, Ivar Aavatsmark, and GT Eigestad. Monotonicity of control volume methods. *Numerische Mathematik*, 106(2):255–288, 2007.
- Gordon L Olson, Lawrence H Auer, and Michael L Hall. Diffusion, p1, and other approximate forms of radiation transport. *Journal of Quantitative Spectroscopy and Radiative Transfer*, 64(6):619–634, 2000.
- Sasi Palaniyappan, JP Sauppe, BJ Tobias, CF Kawaguchi, KA Flippo, AB Zylstra, OL Landen, D Shvarts, E Malka, SH Batha, et al. Hydro-scaling of direct-drive cylindrical implosions at the omega and the national ignition facility. *Physics of Plasmas*, 27(4):042708, 2020.
- L John Perkins, R Betti, KN LaFortune, and WH Williams. Shock ignition: A new approach to high gain inertial confinement fusion on the national ignition facility. *Physical review letters*, 103(4):045004, 2009.
- GJ Pert. A class of similar solutions of the non-linear diffusion equation. *Journal of Physics A: Mathematical and General*, 10(4):583, 1977.
- GJ Pert. Physical constraints in numerical calculations of diffusion. *Journal of Computational Physics*, 42(1):20–52, 1981.
- Susanne Pfalzner. *An introduction to inertial confinement fusion*. CRC Press, 2006.
- Alexandre Poyé, Sébastien Hulin, Mathieu Bailly-Grandvaux, J-L Dubois, Jérôme Ribolzi, Didier Raffestin, Matthieu Bardon, Frédéric Lubrano-Lavaderci, Emmanuel D’Humières, J Jorge Santos, et al. Physics of giant electromagnetic pulse generation in short-pulse laser experiments. *Physical Review E*, 91(4):043106, 2015.
- PB Radha, M Hohenberger, DH Edgell, JA Marozas, FJ Marshall, DT Michel, MJ Rosenberg, W Seka, A Shvydky, TR Boehly, et al. Direct drive: Simulations and results from the national ignition facility. *Physics of Plasmas*, 23(5):056305, 2016.
- Sean P Regan, John A Marozas, John H Kelly, Thomas R Boehly, William R Donaldson, Paul A Jaanimagi, Robert L Keck, Terrance J Kessler, David D Meyerhofer, Wolf Seka, et al. Experimental investigation of smoothing by spectral dispersion. *JOSA B*, 17(9):1483–1489, 2000.

- Marc B Reynolds. Square/disc mappings. <https://marc-b-reynolds.github.io/math/2017/01/08/SquareDisc.html>, 2017. Accessed: 2021-05-11.
- X Ribeyre, G Schurtz, M Lafon, S Galera, and S Weber. Shock ignition: an alternative scheme for hiper. *Plasma Physics and Controlled Fusion*, 51(1):015013, 2008.
- APL Robinson, DJ Strozzi, JR Davies, L Gremillet, JJ Honrubia, T Johzaki, RJ Kingham, M Sherlock, and AA Solodov. Theory of fast electron transport for fast ignition. *Nuclear Fusion*, 54(5):054003, 2014.
- MD Rosen, HA Scott, DE Hinkel, EA Williams, DA Callahan, RPJ Town, L Divol, PA Michel, WL Kruer, LJ Suter, et al. The role of a detailed configuration accounting (dca) atomic physics package in explaining the energy balance in ignition-scale hohlraums. *High Energy Density Physics*, 7(3):180–190, 2011.
- MJ Rosenberg, AA Solodov, JF Myatt, W Seka, P Michel, M Hohenberger, RW Short, R Epstein, SP Regan, EM Campbell, et al. Origins and scaling of hot-electron preheat in ignition-scale direct-drive inertial confinement fusion experiments. *Physical review letters*, 120(5):055001, 2018.
- Max Roser and Esteban Ortiz-Ospina. Global extreme poverty. *Our World in Data*, 2013. <https://ourworldindata.org/extreme-poverty>.
- Yousef Saad. *Iterative methods for sparse linear systems*. SIAM, 2003.
- GP Schurtz, Ph D Nicolai, and M Busquet. A nonlocal electron conduction model for multidimensional radiation hydrodynamics codes. *Physics of plasmas*, 7(10):4238–4249, 2000.
- R.H.H. Scott, K. Glize, L. Antonelli, M. Khan, W. Theobald, M. Wei, R. Betti, C. Stoeckl, A.G. Seaton, T.D Arber, D. Barlow, T. Goffrey, K. Bennett, W. Garbett, S. Atzeni, A. Casner, D. Batani, C. Li, and N. Woolsey. Shock ignition laser-plasma interactions in ignition-scale plasmas. *Physical review letters* (unpublished), 2021.
- Alexander George Seaton. *Particle-in-cell Simulations of Laser-plasma Instabilities in Shock-ignition*. PhD thesis, University of Warwick, 2019.
- Alexander George Seaton and Tony D Arber. Laser-plasma instabilities in long scale-length plasmas relevant to shock-ignition. *Physics of Plasmas*, 27(8):082704, 2020.

- Stephen M Seltzer and Martin J Berger. Improved procedure for calculating the collision stopping power of elements and compounds for electrons and positrons. *The International Journal of Applied Radiation and Isotopes*, 35(7):665–676, 1984.
- WL Shang, R Betti, SX Hu, K Woo, L Hao, C Ren, AR Christopherson, A Bose, and W Theobald. Electron shock ignition of inertial fusion targets. *Physical review letters*, 119(19):195001, 2017.
- M Shashkov et al. Solving diffusion equations with rough coefficients in rough grids. *Journal of Computational Physics*, 129(2):383–405, 1996.
- Z Sheng and G Yuan. A nine point scheme for the approximation of diffusion operators on distorted quadrilateral meshes. *SIAM Journal on Scientific Computing*, 30(3):1341–1361, 2008.
- Zhiqiang Sheng and Guangwei Yuan. An improved monotone finite volume scheme for diffusion equation on polygonal meshes. *Journal of Computational Physics*, 231(9):3739–3754, 2012.
- Mark Sherlock, Jonathan Peter Brodrick, and Christopher Paul Ridgers. A comparison of non-local electron transport models for laser-plasmas relevant to inertial confinement fusion. *Physics of Plasmas*, 24(8):082706, 2017.
- A Simon, RW Short, EA Williams, and T Dewandre. On the inhomogeneous two-plasmon instability. *The Physics of fluids*, 26(10):3107–3118, 1983.
- N Sinenian, M JE Manuel, JA Frenje, FH Séguin, CK Li, and RD Petrasso. An empirical target discharging model relevant to hot-electron preheat in direct-drive implosions on omega. *Plasma Physics and Controlled Fusion*, 55(4):045001, 2013.
- S Skupsky, JA Marozas, RS Craxton, R Betti, TJB Collins, JA Delettrez, VN Goncharov, PW McKenty, PB Radha, TR Boehly, et al. Polar direct drive on the national ignition facility. *Physics of Plasmas*, 11(5):2763–2770, 2004.
- AA Solodov and R Betti. Stopping power and range of energetic electrons in dense plasmas of fast-ignition fusion targets. *Physics of Plasmas*, 15(4):042707, 2008.
- AA Solodov, MJ Rosenberg, JF Myatt, R Epstein, SP Regan, W Seka, J Shaw, M Hohenberger, JW Bates, JD Moody, et al. Hydrodynamic simulations of long-scale-length plasmas for two-plasmon-decay planar-target experiments on the nif. In *Journal of Physics: Conference Series*, volume 717, page 012053. IOP Publishing, 2016a.

- AA Solodov, B Yaakobi, DH Edgell, RK Follett, JF Myatt, C Sorce, and DH Froula. Measurements of hot-electron temperature in laser-irradiated plasmas. *Physics of Plasmas*, 23(10):102707, 2016b.
- SJ Spencer, Alexander George Seaton, Tom Goffrey, and Tony D Arber. Inflationary stimulated raman scattering in shock-ignition plasmas. *Physics of Plasmas*, 27(12):122705, 2020.
- Lyman Spitzer. *Physics of fully ionized gases*. Courier Corporation, 2006.
- Lyman Spitzer Jr and Richard Härm. Transport phenomena in a completely ionized gas. *Physical Review*, 89(5):977, 1953.
- RM Sternheimer, MJ Berger, and Stephen M Seltzer. Density effect for the ionization loss of charged particles in various substances. *Atomic Data and Nuclear Data Tables*, 30(2):261–271, 1984.
- C Stoeckl, G Fiksel, D Guy, C Mileham, PM Nilson, TC Sangster, MJ Shoup III, and W Theobald. A spherical crystal imager for omega ep. *Review of Scientific Instruments*, 83(3):033107, 2012.
- M Stoeckl and AA Solodov. Refining instrument response functions with 3-d monte carlo simulations of differential hard x-ray spectrometers. *Nuclear Instruments and Methods in Physics Research Section A: Accelerators, Spectrometers, Detectors and Associated Equipment*, 931:162–171, 2019.
- M Tabak, DH Munro, and JD Lindl. Hydrodynamic stability and the direct drive approach to laser fusion. *Physics of Fluids B: Plasma Physics*, 2(5):1007–1014, 1990.
- H Takabe, L Montierth, and RL Morse. Self-consistent eigenvalue analysis of rayleigh–taylor instability in an ablating plasma. *The Physics of fluids*, 26(8):2299–2307, 1983.
- W Theobald, R Betti, C Stoeckl, KS Anderson, JA Delettrez, V Yu Glebov, VN Goncharov, FJ Marshall, DN Maywar, RL McCrory, et al. Initial experiments on the shock-ignition inertial confinement fusion concept. *Physics of Plasmas*, 15(5):056306, 2008.
- W Theobald, R Nora, M Lafon, A Casner, X Ribeyre, KS Anderson, R Betti, JA Delettrez, JA Frenje, V Yu Glebov, et al. Spherical shock-ignition experiments with the 40+ 20-beam configuration on omega. *Physics of Plasmas*, 19(10):102706, 2012.

- Henk A Van der Vorst. Bi-cgstab: A fast and smoothly converging variant of bi-cg for the solution of nonsymmetric linear systems. *SIAM Journal on scientific and Statistical Computing*, 13(2):631–644, 1992.
- Jasmina L Vujic. Monte carlo sampling methods, nuclear engineering department, university of california, usa. <http://web.ist.utl.pt/~ist11038/acad/theo/simul/Vujic.pdf>, 2008. Accessed: 2021-05-06.
- A. J. Wathen. Preconditioning. *Acta Numerica*, 24:329376, 2015. doi: 10.1017/S0962492915000021.
- Christopher John Werner, Jeffrey S Bull, Clell Jeffrey Solomon, Forrest B Brown, Gregg Walter McKinney, Michael Evan Rising, David A Dixon, Roger Lee Martz, Henry G Hughes, Lawrence James Cox, et al. Mcnp version 6.2 release notes. Technical report, Los Alamos National Lab.(LANL), Los Alamos, NM (United States), 2018.
- SC Wilks, AB Langdon, TE Cowan, M Roth, M Singh, S Hatchett, MH Key, D Pennington, A MacKinnon, and RA Snively. Energetic proton generation in ultra-intense laser–solid interactions. *Physics of plasmas*, 8(2):542–549, 2001.
- EA Williams, RL Berger, RP Drake, AM Rubenchik, BS Bauer, DD Meyerhofer, AC Gaeris, and TW Johnston. The frequency and damping of ion acoustic waves in hydrocarbon (ch) and two-ion-species plasmas. *Physics of Plasmas*, 2(1):129–138, 1995.
- B Yaakobi, AA Solodov, JF Myatt, JA Delettrez, C Stoeckl, and DH Froula. Measurements of the divergence of fast electrons in laser-irradiated spherical targets. *Physics of Plasmas*, 20(9):092706, 2013.
- Lin Yin, BJ Albright, HA Rose, KJ Bowers, B Bergen, RK Kirkwood, DE Hinkel, AB Langdon, P Michel, DS Montgomery, et al. Trapping induced nonlinear behavior of backward stimulated raman scattering in multi-speckled laser beams. *Physics of Plasmas*, 19(5):056304, 2012.
- Ya B Zel'Dovich and Yu P Raizer. *Physics of shock waves and high-temperature hydrodynamic phenomena*. Courier Corporation, 2002.
- S Zhang, CM Krauland, J Peebles, J Li, FN Beg, N Alexander, W Theobald, R Betti, D Haberberger, EM Campbell, et al. Experimental study of hot electron generation in shock ignition relevant high-intensity regime with large scale hot plasmas. *Physics of Plasmas*, 27(2):023111, 2020.

CD Zhou and R Betti. A measurable lawson criterion and hydro-equivalent curves for inertial confinement fusion. *Physics of Plasmas*, 15(10):102707, 2008.